NUMERICAL ANALYSIS OF DESTRESSING TO MITIGATE THE SUDDEN COLLAPSE RISK OF STIFF LAYERS IN SOLUTION MINING

A THESIS SUBMITTED TO
THE GRADUATE SCHOOL OF NATURAL AND APPLIED SCIENCES
OF
MIDDLE EAST TECHNICAL UNIVERSITY

BY

CEM NOYAN KONUK

IN PARTIAL FULFILLMENT OF THE REQUIREMENTS
FOR
THE DEGREE OF MASTER OF SCIENCE
IN
MINING ENGINEERING

JUNE 2023

Approval of the thesis:

NUMERICAL ANALYSIS OF DESTRESSING TO MITIGATE THE SUDDEN COLLAPSE RISK OF STIFF LAYERS IN SOLUTION MINING

submitted by **CEM NOYAN KONUK** in partial fulfillment of the requirements for the degree of **Master of Science** i**n Mining Engineering, Middle East Technical University** by,

Prof. Dr. Halil Kalıpçılar
Dean, Graduate School of **Natural and Applied Sciences** _____

Prof. Dr. Naci Emre Altun
Head of the Department, **Mining Engineering** _____

Assist. Prof. Dr. Ahmet Güneş Yardımcı
Supervisor, **Mining Engineering, METU** _____

Examining Committee Members:

Prof. Dr. Bahtiyar Ünver
Mining Engineering, Hacettepe University _____

Assist. Prof. Dr. Ahmet Güneş Yardımcı
Mining Engineering, METU _____

Assoc. Prof. Dr. Mustafa Erkayaoğlu
Mining Engineering, METU _____

Date: 12.06.2023

I hereby declare that all information in this document has been obtained and presented in accordance with academic rules and ethical conduct. I also declare that, as required by these rules and conduct, I have fully cited and referenced all material and results that are not original to this work.

Name Last name : Cem Noyan Konuk

Signature :

ABSTRACT

NUMERICAL ANALYSIS OF DESTRESSING TO MITIGATE THE SUDDEN COLLAPSE RISK OF STIFF LAYERS IN SOLUTION MINING

Konuk, Cem Noyan
Master of Science, Mining Engineering
Supervisor : Assist. Prof. Dr. Ahmet Güneş Yardımcı

June 2023, 147 pages

Solution mining in thick deposits is a challenging practise of strata geomechanics. The stiff layers overlaying the production caverns can bear excessive loads and the strain energy may be relesead by a sudden collapse. The violent failure of the strata has serious consequences in terms of operational sustainability and safety. To mitigate the risk, destressing methods can be used to induce fracture networks on the stiff layers. This study employs a discontinuum based numerical code to investigate the alternative destressing schemes. Considering the operational practises and economy, the ribbon and borehole patterns were simulated for different configurations. Discrete Fracture Networks was used for implementation of the fractured region. While the ribbons were examined for various spacings between the fractured zones, the boreholes were studied with different patterns. A sample production on a single cavern was simulated on a staged manner and the strata mechanics were monitored with history points. Comparing the model results, the most viable destressing scheme was determined for solution mining.

Keywords: Solution Mining, Strata Control, Destressing

ÖZ

ÇÖZELTİ MADENCİLİĞİNDE SERT TABAKALARIN ANİ ÇÖKME RİSKİNİ AZALTMAK İÇİN GERİLME RAHATLATMANIN NÜMERİK ANALİZİ

Konuk, Cem Noyan
Yüksek Lisans, Maden Mühendisliği
Tez Yöneticisi: Dr. Öğr. Üyesi Ahmet Güneş Yardımcı

Haziran 2023, 147 sayfa

Kalın damar içerisinde çözelti madenciliği jeomekanik açıdan zorlu bir uygulamadır. Üretim açıklıklarının üzerindeki katı tabakaların yüksek miktarda yük ve stres taşıyabilmesi nedeniyle gerilme enerjinin aniden salınması durumunda ani göçük riski oluşabilmektedir. Bu durum, operasyonel devamlılığı ve güvenliği tehdit eder. Ani göçme riskini ortadan kaldırmak için, sert tabakalarda çatlak ağları oluşturma ve tabaka gerilme rahatlatma yöntemleri kullanılır. Bu çalışmada, olası alternatif gerilme rahatlatma teknikleri, süreksizlik temelli sayısal modeller yardımıyla değerlendirilmiştir. Operasyonel kolaylık ve ekonomi gibi faktörler göz önünde bulundurularak şerit ve delgi düzenleri değerlendirilmiştir. Kırık ve çatlak ağlarını simüle etmek için ayrık çatlak ağları yöntemi kullanılmıştır. Şerit düzeni farklı aralık mesafelerinde değerlendirilirken, delgi düzeni farklı örüntülerde değerlendirilmiştir. Tek bir kavernada aşamalı üretim simülasyonu yapılırken tabakalardaki mekanik davranışlar izlenmiştir. Model çıktıları değerlendirilerek en uygun gerilme rahatlatma düzeni belirlenmiştir.

Anahtar Kelimeler: Çözelti Madenciliği, Tabaka Kontrolü, Gerilme Rahatlatma

To my mother, thank you for your belief in my abilities and your constant encouragement.

To my sister, your passion for learning and intellectual curiosity have ignited my own thirst for knowledge.

ACKNOWLEDGMENTS

I would like to express my deepest gratitude and appreciation to everyone who has contributed to the completion of this thesis. First and foremost, I am indebted to my thesis supervisor, Ahmet Güneş Yardımcı, for his invaluable mentorship, expertise, and commitment throughout the entire thesis journey. His insightful feedback, constructive criticism, and constant encouragement have been instrumental in refining my ideas and methodologies. I am also grateful to my former workplace, Eti Soda, for granting me the opportunity to pursue higher education while working. I would like to extend my heartfelt appreciation to all my colleagues at Eti Soda for their support and cooperation during my course times.

TABLE OF CONTENTS

ABSTRACT v

ÖZ vi

ACKNOWLEDGMENTS viii

TABLE OF CONTENTS ix

LIST OF TABLES xii

LIST OF FIGURES xiii

LIST OF ABBREVIATIONS xix

LIST OF SYMBOLS xxi

CHAPTERS

1 INTRODUCTION 1

1.1 Research Motivation and Problem Statement 2

1.2 Objective and Scope of the Study 3

1.3 Research Methodology 4

1.4 Novelty of the Thesis 4

1.5 Structure of the Thesis 5

2 LITERATURE REVIEW 7

2.1 Extraction of Deep Tabular Deposits 7

2.1.1 Room and Pillar Mining 11

2.1.2 Longwall Mining 13

2.1.3 Solution Mining 15

2.2 Geomechanical Classification of Rock Mass 20

2.2.1 Premises 20

2.2.2 Commonly Used Rock Mass Classification Systems (RMR, Q-Index & GSI) … 23
2.2.3 The Recent Developments 28
2.3 Determination of the Geomechanical Properties of Rocks 31
2.3.1 Rock Mechanics Laboratory Tests 33
2.3.2 In-Situ Rock Test 35
2.4 Numerical Analysis in Geomechanics 38
2.4.1 Finite Element Method 40
2.4.2 Discrete Element Method 42
2.4.3 Hybrid Methods 50
2.4.4 Meshless Methods 51
2.5 Common Strata Control Problem in Sedimentary Deposits 52
2.5.1 Roof Instability 52
2.5.2 Surface Subsidence 55
2.6 Destressing 56
3 DATA COLLECTION FOR THE NUMERICAL STUDY 59
3.1 The Field Studies 59
3.1.1 Identification of the Structural Domains 60
3.1.2 Rock Mass Quality Classification 62
3.2 Laboratory Testing 63
3.3 Determination of the Rock Mass Parameters 64
4 NUMERICAL ANALYSIS OF SOLUTION MINING IN A THICK DEPOSIT 67
4.1 The Model Geometry 68

4.2 Stress Distribution within the Strata due to Production in a Single Cavern 73
4.3 Validation and Verification of DFN as a Destress Modeling Technique 83
4.4 Determination of the Suitable Destressing Pattern..... 88
4.4.1 The Ribbon Type Destressing Pattern 89
4.4.2 The Borehole Type Destressing Pattern..... 91
5 RESULTS AND DISCUSSION 95
5.1 Destressing with the Ribbon Pattern 95
5.2 Destressing with the Borehole Pattern 104
5.3 Selection of the Best Pattern in the Upper Stiff Layer (T3)..... 109
5.4 Assessment of Destressing in the Upper (T3) and the Lower (T4) Stiff Strata. 110
6 CONCLUSION 115
REFERENCES 117
A. Appendix 1 141

LIST OF TABLES

TABLES

Table 2.1 Deposits classified by depth (Adler & Thompson, 2011) 9
Table 2.2 Tabular deposits classified by inclinations and rock strength (Adler & Thompson, 2011) 9
Table 2.3 Tabular deposits classified by thickness (after Adler & Thompson, 2011). 10
Table 2.4 Summary of the rock mass classification systems (after Cosar, 2004; Ünal & Özkan, 1996; Yardimci, 2013) 21
Table 2.5 Interpretation of the 'Rock Quality Designation' (RQD) (after Deere et al., 1967) 24
Table 2.6 Interpretation of the 'Rock Mass Rating (RMR_{89})' system (after Bieniawski, 1989) 24
Table 2.7 The rock tests (ISRM, 2007) 31
Table 2.8 Rock Mechanics Laboratory Tests and Parameters 33
Table 2.9 The advantages and disadvantages of different DFN approaches (after Lei et al., 2017) 49
Table 3.1 Rock material properties for a representative trona field 64
Table 3.2 Rock mass geomechanical parameters 65
Table 3.3 Joint properties of discontinuities and DFN 65

LIST OF FIGURES

FIGURES

Figure 2.1 (a) Massive ore body (b) lenticular ore body (c) disseminated ore body (d) vein type ore body (e) tabular ore body 8
Figure 2.2 Room and pillar mining (a) in a regular pillar layout in hard rock (after Martens & Assoc., 1972) (b) in a random pillar layout in hard rock (c) in a coal mine (Paulick, 1963) 13
Figure 2.3 A typical LTCC method with AFC (Bessinger, 2011) 15
Figure 2.4 Longwall mining with (a) advance and (b) retreating systems 15
Figure 2.5 (a) single vertical well (b) dual vertical well (c) piste (d) horizontal well with single vertical and (e) dual vertical well (f) multiple horizontal well solution mining setup 17
Figure 2.6 Representation of multi-cavern production of solution mining with horizontal and vertical well combination 19
Figure 2.7 Interpretation of the Q-Tunneling Index and estimated support categories (after Grimstad & Barton, 1993, taken from Hoek, 2007) 25
Figure 2.8 GSI interpretation table (Hoek et al., 1998) 27
Figure 2.9 Modified Q chart 29
Figure 2.10 Q-slope stability chart 29
Figure 2.11 Interpretation table of RMQR (Aydan et al., 2014) 30
Figure 2.12 Ranges for various index tests to determine UCS (ISRM, 2014) 34
Figure 2.13 Plate test equipment (ISRM, 2007) 35
Figure 2.14 A typical set-up for an in-situ direct shear test 36
Figure 2.15 (a) A typical flatjack test equipment (b) a sample layout for the test .. 37
Figure 2.16 The steps of a typical overcoring operation (taken from Guo et al., 2013) 38
Figure 2.17 Four different approaches to rock mechanics modeling and design (after Hudson, 2001) 39

Figure 2.18 The parallel bond model in PFC (a) normal and shear stiffness (b) constitutive behavior in shear and tension (Lisjak & Grasselli, 2014).....44
Figure 2.19 UDEC fracture propagation (a) normal and shear stiffness (b) constitutive behavior in shear and tension (Lisjak & Grasselli, 2014).....45
Figure 2.20 Calculation cycles in DEM (Jing, 2003).....46
Figure 2.21 Representation of DFN in (a) & (b) 3-D discs (Long et al., 1985) (c) 2-D lines (Lei et al., 2017) (d) 3-D polygons (Itasca Consulting Group Inc., 2016)..48
Figure 2.22 Measures of fracture density (taken from Chou et al., 2016) 50
Figure 2.23 Tributary area representation 53
Figure 2.24 The caved, fractured, and continuous deformation zones above an underground opening (modified after Peng & Chiang, 1984).....54
Figure 2.25 Section view of a tabular deposit and surface subsidence (Peng, 1978) 55
Figure 2.26 Examples of caving and collapse in (a) Sarralbe – Loraine (France) with a weak overburden (b) Twenthe – East Netherlands with an intermediate overburden (c) Nancy – Lorraine (France) with a stiff overburden (taken from Daupley et al., 2005) 57
Figure 3.1 Stratigraphy of Beypazarı Trona Field.....61
Figure 3.2 (a) RQD (b) RMR_{89} (c) Q-index distribution of the samples.....63
Figure 4.1 The isometric view of the model body and the strata dimensions 69
Figure 4.2 (a) The side view, (b) the front view and (c) the isometric view of the model 71
Figure 4.3 History points within the (a) overburden and (b) the cavern wall, interburden, and 20 m inside of the cavern wall 72
Figure 4.4 The unbalanced force history in elastic and plastic stages.....73
Figure 4.5 The maximum principal stresses (a) after removing the first trona layer at the bottom (b) after completing the lower trona seam (c) after completing production both in the upper and lower seams.....75
Figure 4.6 The major principal stress history during the production stages 76
Figure 4.7 The minor principal stress history during the production stages 76

Figure 4.8 The vertical displacements of the strata 77
Figure 4.9 The history points along the cavern wall from the top view 78
Figure 4.10 σ_1 history of the lower trona seam on the cavern wall 79
Figure 4.11 σ_1 history of the lower trona seam 20 m inside the cavern wall..... 79
Figure 4.12 σ_1 history of the upper trona seam on the cavern wall 80
Figure 4.13 σ_1 history of the upper trona seam 20 m inside the cavern wall..... 80
Figure 4.14 The maximum principal stresses at (a) the virgin state, (b) after the first stage of production, (c) after the second stage, (d) after the third stage, (e) after the complete lower trona seam production, (f) after the fifth stage of production, (g) after the sixth and (h) seventh stage of production, and (i) complete upper and lower production 82
Figure 4.15 Validation of DFN with relaxation of T3 layer 84
Figure 4.16 Comparison of the maximum principal stress in T3 layer with and without destressing..... 84
Figure 4.17 Comparison of the major principal stress distributions after the first stage of production (a) without destressing (b) with destressing, after the completion of the lower trona seam (c) without destressing (d) with destressing, and completing the production both in the upper and lower seams (e) without destressing and (f) with destressing 85
Figure 4.18 Yielded elements after first lower layer removal (a) without destressing (b) destressing, complete lower layer removal stage (c) without destressing (d) destressing, and both complete upper and lower layer removal (e) without destressing (f) destressing 87
Figure 4.19 Determination of the best destressing pattern 89
Figure 4.20 The model body, dimensions, and distances of RN_30 pattern in (a) isometric view and (b) side view, RN_60 (c) isometric view and (d) side view, RN_90 (e) isometric view and (f) side view 90
Figure 4.21 The borehole pattern dimensions, distance, and the model body of the BH_STG (a) top view and (b) side view, BH_STR (c) top view and (d) side view92

Figure 4.22 The destressing patterns in T4 (a) the ribbon pattern with 30 m spacing and (b) the staggered borehole patterns 93
Figure 5.1 Spacing between destressed ribbons (a) 30 m (RN_30) (b) 60 m (RN_60) and (c) 90 m (RN_90) 96
Figure 5.2 σ_1 history in the upper stiff layer (T3) when the same layer is destressed with various ribbon spacings 98
Figure 5.3 σ_1 history in the lower stiff layer (T4) for destressing the upper stiff layer (T3) with various ribbon spacings 98
Figure 5.4 The major principal stresses after the first production stage in a) woDESS b) RN_30 c) RN_60 d) RN_90 99
Figure 5.5 Stress distributions after fourth production stage in a) woDESS b) RN_30 c) RN_60 d) RN_90 100
Figure 5.6 Stress distributions after the eighth production stage in a) woDESS b) RN_30 c) RN_60 d) RN_90 101
Figure 5.7 The yielded elements after removal of the first layer in the lower seam (a) woDESS, (b) RN_30, (c) RN_60, and (d) RN_90 102
Figure 5.8 The yielded elements after completing the lower trona layer (a) woDESS, (b) RN_30, (c) RN_60, and (d) RN_90 103
Figure 5.9 The yielded elements after completing both the lower and upper trona seams (a) woDESS, (b) RN_30, (c) RN_60, and (d) RN_90 104
Figure 5.10 The top view of the (a) staggered (BH_STG) and (b) straight (BH_STR) patterns of the borehole destressing 105
Figure 5.11 Comparison of σ_1 history in the upper stiff layer (T3) for no destressing and destressing in T3 layer with borehole patterns 106
Figure 5.12 Comparison of σ_1 history in the lower stiff layer (T4) for no destressing and destressing in T3 layer with borehole patterns 106
Figure 5.13 Stress distributions when BH_STR applied and after (a) the first production stage, (c) completing production in the lower seam, (e) producing both the upper and lower seams; when BH_STG applied and after (b) the first

production stage, (d) completing production in the lower seam, (f) producing both the upper and lower seams 107
Figure 5.14 The yielded elements when BH_STG applied and after (a) the first production stage, (c) completing production in the lower seam, (e) producing both the upper and lower seams; when BH_STR applied and after (b) the first production stage , (d) completing production in the lower seam, (f) producing both the upper and lower seams 108
Figure 5.15 Comparison of σ_1 history in T3 layer when no destressing is induced and T3 layer is fractured using RN_60 and BH_STG patterns 109
Figure 5.16 σ_1 histories in T4 layer for RN_60, BH_STG, and woDESS models 110
Figure 5.17 The major principal stresses in T3 and T4 layers for destressing with T3_RN_60 (left) and T4_RN_60 patterns (right) 112
Figure 5.18 Percentage of major principal stress changes in the upper stiff layer (T3) and lower stiff layer (T4) regarding the destressing pattern and the strata... 113
Figure 5.19 σ_1 values for T3 and T4 layer for T3_BH_STG (left) and T4_BH_STG (right) 114
Figure A.1 GSI value distribution graph of layers 141
Figure A.2 After complete trona layer removal maximum principal stresses in (a) T1 layer (b) T2 layer (c) T3 layer (d) T4 layer (e)T5 layer (f) T6 layer 142
Figure A.3 σ_{dev} (in T3 layer) graph of woDESS model 143
Figure A.4 σ_{dev} (in T3 layer) graph of DESS model 143
Figure A.5 σ_1 history of the 1st stage level history points on the cavern wall (upper) and 20 m inside the cavern wall (lower) 144
Figure A.6 σ_1 history of the 2nd stage level history points on the cavern wall (upper) and 20 m inside the cavern wall (lower) 144
Figure A.7 σ_1 history of the 3rd stage level history points on the cavern wall (upper) and 20 m inside the cavern wall (lower) 145
Figure A.8 σ_1 history of the 4th stage level history points on the cavern wall (upper) and 20 m inside the cavern wall (lower) 145

Figure A.9 σ_1 history of the 5th stage level history points on the cavern wall (upper) and 20 m inside the cavern wall (lower) 146
Figure A.10 σ_1 history of the 6th stage level history points on the cavern wall (upper) and 20 m inside the cavern wall (lower) 146
Figure A.11 σ_1 history of the 7th stage level history points on the cavern wall (upper) and 20 m inside the cavern wall (lower) 147
Figure A.12 σ_1 history of the 8th stage level history points on the cavern wall (upper) and 20 m inside the cavern wall (lower) 147

LIST OF ABBREVIATIONS

ABBREVIATIONS

AFC : Armored Face Conveyor

ASTM : American Society for Testing and Materials

BEM : Boundary Element Method

DD : Degradation Degree

DDA : Discontinuous Deformation Analysis

DEM : Distinct Element Method

DFN : Discrete Fracture Network

DIN : German Institute for Standardization

DS : Discontinuity Spacing

DSN : Discontinuity Set Number

FDEM : Hybrid Finite-Discrete Element Approach

FDM : Finite Difference Method

FEM : Finite Element Method

GSI : Geological Strength Index

GWAC : Groundwater Absorption Condition

GWSC : Groundwater Seepage Condition

ISRM : International Society for Rock Mechanics and Rock Engineering

LTCC : Longwall Top Coal Caving

MSL : Multi-slice Longwall

PFC : Particle Flow Code

RMQR : Rock Mass Quality Rating

RMR : Rock Mass Rating

RQD : Rock Quality Designation

SPH : Smoothed Particle Hydrodynamics

SPL : Single Pass Longwall

SRF : Stress Reduction Factor

TS : Tensile Strength

UCS : Uniaxial Compressive Strength

UDEC : Universal Distinct Element Code

LIST OF SYMBOLS

SYMBOLS

c : Cohesion

E :Young's modulus

G : Shear Modulus

H : Depth

J_a : Joint Alteration

J_n : Joint Set Number

J_r : Joint Roughness

J_w : Water Reduction Factor

K : Bulk Modulus

K_n : Normal Stiffness

K_s : Shear Stiffness

m : meters

N : Newton

Pa : Pascal

P_r : Required Support Pressures

V_p : Seismic Velocity

W_o : Opening Width

W_p : Pillar Width

σ_1 : Major Principal Stress

σ_3 :Minor Principal Stress

σ_c : Uniaxial Compressive Strength

σ_{pa} : Average Pillar Stress

υ : Poisson's ratio

ϕ : Internal Friction Angle

CHAPTER 1

INTRODUCTION

Bedded mineral deposits are commonly produced in bulk amounts leaving a large opening space with no means of permanent support. Regarding the huge excavation volume, filling is not a viable option to slow down the strata movements. Indeed, strata deformations may provide a natural support by bending into the opening and contacting with the floor to establish a force balance within the disturbed stress region. The movements affect not only the close vicinity of the opening but also cause significant deformations on the topographical surface. Due to the risks to the operational sustainability and safety posed by extensive yield and unexpected failure of overlaying geological units, strata control has been a major concern in underground mining. Especially, sudden collapse is a serious instability risk in the mining of sedimentary-type deposits like fossil fuels (i.e. coal) and industrial minerals. Trona has recently been a popular industrial mineral, which naturally occurs within horizontal or shallowly dipping beds. Due to its geochemical composition that majorly involves sodium carbonates, trona is a raw material in glass, chemicals, metals, and food industries. Following the regularly growing trend, the demand for trona mineral has reached up to 17 million tonnes as of 2021 with a 20% increase (USGS, 2022). Turkey owns the second largest reserve in the world after the USA, which has a current production capacity of approximately 5 million tonnes. For the deposits in Beypazarı and Kazan districts close to Ankara, solution mining technique has been adopted due to the economical and operational advantages (Aydın & Şenkal, 2001). Briefly, solution mining is an in-situ leaching technique operated via horizontal and vertical wells to reach and access the trona seams. Hot solvent injection dissolves the trona around the horizontal well and creates a solution that is later pumped out from the vertical wells in the form of a ‘brine’. Production results in a large underground opening called a ‘cavern’.

Eventually, the overlaying geological units yield and collapse into the production openings. Regarding the sedimentary rocks form within long periods of time by accumulation of different minerals, a variation can be expected not only in the mineralogical and physical characteristics but also in the geomechanical properties. While weak rocks can easily fail, the stiff layers tend to bear more stress that is induced by the production. As a result, the opening's roof may fail with a sudden collapse mechanism. Strata control measures need to be taken for the mitigation of sudden collapse risk since the consequences are likely to be devastating both in the production zone and on the topographical surface. Developments in the rock mechanics science and computational mechanics provide useful tools and background knowledge to analyze the strata problems for different production scenarios.

This research investigates the alternative destressing methods and develops a useful scheme for production in thick trona deposits. Taking advantage of discrete numerical simulations, a destressing plan was developed and proposed for the potential strata problems in solution mining.

1.1 Research Motivation and Problem Statement

Trona is an economic mineral that is widely used in various industries. Conventional room and pillar mining and longwall mining techniques are embraced for trona mining around the world (USGS, 2022). However, Turkish trona reserves have been operated by solution mining due to the hydrogeological and geotechnical challenges. Although this state of art mining method comes with its advantages in terms of operational simplicity, safety, and low production cost, it needs to overcome many difficulties posed by the geology, mineralogical composition of the ore, and structural discontinuities and bedding planes that could affect the dissolving mechanism. In addition, large deformations are inevitable in the overburden strata due to the large production openings within the thick trona layers. Induced stress accumulation on the overlaying strata results in an asynchronous settlement between

different geological units due to geomechanical variations. Especially, the stiff layers tend to collapse suddenly and violently with potential consequences of losing the production caverns and control of production due to the propagation of the fracture network. Another drawback can be stated to be the adverse effects on the ground surface. Considering all, a suitable de-stressing method is required to mitigate the sudden collapse risk. The motivation of this study is to examine alternative destressing methods for use in solution mining and come up with a practical and economic solution. The classical destressing methods involve operational challenges for large volumes of rock mass. For flat, tabular, and extensive deposits, the conventional destressing methods need to be revisited to develop a more effective way of inducing a fracture network.

1.2 Objective and Scope of the Study

The objective of this study is to determine a destressing scheme that conforms with the solution mining method and effectively relieves the accumulated stress on stiff geological layers to mitigate the risk of sudden collapse. The best method is projected to be found using numerical simulations of alternative stress relieve techniques and patterns based on distinct element method. The scope of this work involves identification of the rock mass quality within the research field and the determination of geomechanical properties by laboratory rock mechanics tests. The outcomes of the rock mass characterization are used to represent real trona and overlaying strata materials in the numerical models of production in a single cavern to assess different destressing methods. Induced stresses around the cavern under different production stages were investigated by stress and deformation analyses. Although single cavern production is the major concern of this study, abutment pressure analyses are carried out to comment on the potential effects of production on the neighboring caverns. Finally, the most effective and practical stress relieving method is determined by comparing numerical simulation results.

1.3 Research Methodology

The rock mass quality was determined using the common rock quality classification systems. The core samples were subjected to laboratory scale rock mechanics tests to determine the rock mass geomechanical properties based on an empirical approach. Alternative numerical methods were investigated to determine the best approach for simulation of sedimentary deposits. Since continuum-based numerical methods are not capable of simulating the exact mechanical behavior of rock mass due to the multi-layer stratification and unique mechanical features of strata and contact surfaces, discontinuum-based methods were preferred. 'Distinct Element Method (DEM)' was used for numerical modeling. The geomechanical inputs were used for the back analysis of surface subsidence due to previous productions and the method verification was accomplished. Later, a field scale production using solution mining in thick trona seams was simulated. The distinct production stages were imitated and the development of mechanical stress and deformations were modeled. The fracture network implemented by any suitable destressing technique (hydraulic fracturing, destress blasting, conditioning) was simulated using 'Discrete Fracture Networks (DFN)'.

1.4 Novelty of the Thesis

Numerical simulation of strata movements in solution mining, especially in thick deposits, will contribute to the prediction of strata behavior and elimination of possible aforementioned operational problems. This study will help to test and determine the usefulness of numerical methods in rock mechanics problems in solution mining. Parametrical studies to reveal the relationship between different patterns and various crack densities with stress accumulation and relaxation should also be useful in determining the best destressing practice.

1.5 Structure of the Thesis

This study is composed of five chapters. In the first chapter, the significance of trona mineral and solution mining is presented with an overview of production problems like stress concentration on stiff layers and mitigation techniques. The nature of the problem and objective of the study is given along with the methodology of the study. The second chapter covers a literature review of mining methods that are used in sedimentary deposits, geomechanical classification of the rock mass, and determination of the geomechanical properties of the rocks. Numerical analysis methods in geomechanics, strata control, and destressing methods were also reviewed briefly. The third chapter includes data collection for the numerical study with details of the field study, laboratory testing, and determination of rock mass parameters. Chapter four presents the numerical analysis of solution mining in thick deposits and includes the model body, stress distribution within the strata, validation, and verification of DFN as a destress modeling technique, and investigation of the best destressing pattern. Chapter five covers the comparison of the advantages and disadvantages of DFN, presents the results, and discussion of the case. Finally, chapter six shows the remarkable study outcomes.

CHAPTER 2

LITERATURE REVIEW

This chapter presents an overview of the studies from literature covering sedimentary ore deposits, rock mass characterization, numerical simulation techniques, and destressing. The section starts with the mining methods used for extraction of deep tabular deposits and continues with the geomechanical classification of rock mass. Subsequently, geomechanical simulation techniques are presented. Following a brief review of strata control, this chapter is concluded by destressing methods.

2.1 Extraction of Deep Tabular Deposits

Ore genesis is the formation of minerals over the course of an extended period of geological timescale. Although there are various classifications for the ore formation process (Einaudi, 2000; Evans, 1993), commonly the deposit composition, form, geological setting, and interpreted genesis are taken basis (Gandhi & Sarkar, 2016). The common practice in geology is to divide the rock into three main categories namely igneous, sedimentary, and methamorphic (Robb, 2005). As an economical term of minerals deposits, ore deposits are characterized by their physical properties. Dimensions and orientational relationships (i.e., shape, width, extent, and dip angle) are frequently used to define the orebody type. For instance a ‘massive orebody’ (Figure 2.1.a) refers to a bulk volume of ore with a regular shape and extensive dimensions; on the other hand, a ‘lenticular orebody’ (Figure 2.1.b) refers to a flat-elliptical shape with a gradational change in thickness from thin to moderate around the middle of the ore body. A ‘disseminated orebody’ (Figure 2.1.c) is a deposit type where fine mineral particles are distributed throughout the rock. Although there are debates on the definition of ‘vein type orebody’ (Haynes, 1993), the term in general defines a deposit of ore filling a fissure within the rock mass (Figure 2.1.d). A

‘tabular orebody’ (Figure 2.1.e), which is subject to this study, describes a flat and regularly shaped volume laying horizontal or near horizontal to the ground and extending on the lateral axis.

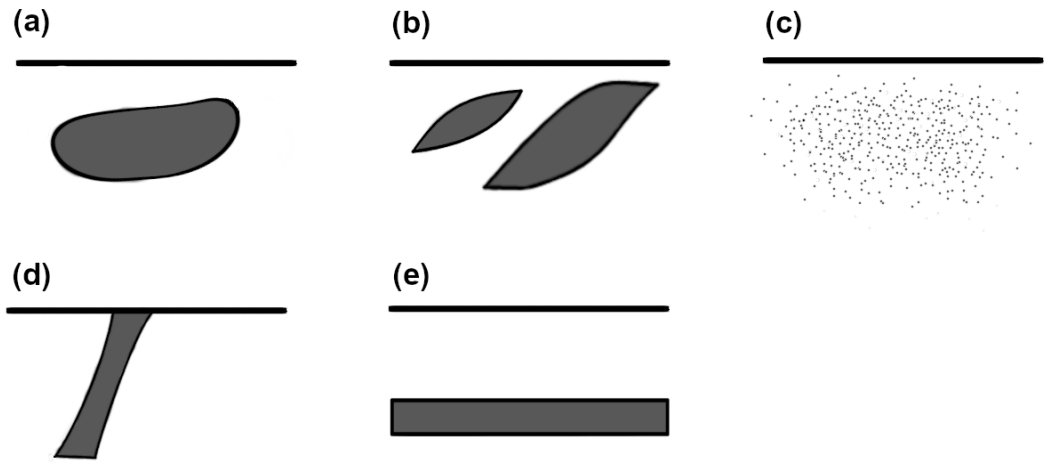

Figure 2.1 (a) Massive ore body (b) lenticular ore body (c) disseminated ore body (d) vein type ore body (e) tabular ore body

In exploitation of tabular deposits (coal, shale, potash, and trona etc.) inclination, deposit thickness, and depth of the deposit play a vital role in the production plan (Popov, 1971). Although there are various methods for the classification of orebodies (Table 2.1), the depth is majorly used to identify the deposit type. Deep deposits are prone to have pillar and roof instability problems as well as bumps and bursts.

Table 2.1 Deposits classified by depth (Adler & Thompson, 2011)

	Deposit Depth		
	Underground		*Surface*
Depth	*Coal*	*Ore*	
Shallow	≤61m	≤305m	≤61m
Moderate	122 – 244m	305 – 457m	61 – 305m
Deep	≥915m	≥1,830m	≥305 – 915m

Flat tabular deposits are generally associated with weak rock strength (Table 2.2) and this results in support requirements and ground control problems (Hamrin, 1982).

Table 2.2 Tabular deposits classified by inclinations and rock strength (Adler & Thompson, 2011)

Inclination	*Dip*	*Rock Strength*
Flat	$\leq 20^0$	Weak rock
Inclined	$20\text{-}45^0$	Average Rock
Steep	$\geq 45^0$	Strong Rock

In addition, the thick seams (Table 2.2) can create rib and pillar problems.

Table 2.3 Tabular deposits classified by thickness (after Adler & Thompson, 2011).

Thickness	*Deposit Thickness*	
	Coal	*Ore*
Thin	0.9 – 1.2m	0.9 – 1.8m
Medium	1.2 – 2.4m	1.8 – 4.6m
Thick	2.4 – 4.6m	4.6 – 15.3m

Mining method selection is a complex process that includes environmental, economical, social, and political considerations in addition to technical challenges (Nelson, 2011). However, aforementioned geomechanical restrictions asserted by the physical and weak rock characteristics of sedimentary rocks force the mining method to prioritize the safety and economy. Considering that the minable near surface resources were expected to deplete by 2006, 27% of mining operations were conducted by underground mining operations in Turkey (Eros & Candelario-Quintana, 2006). This rate has increased up to 31% by 2014 (Mining Intelligence, 2014). Furthermore, in the USA, between 2011 and 2015 surface ore production decreased by 15% while underground ore production increased by 14% (Osborne, 2020). This shows that the trend will continue.

Geological and mechanical complexities make every operation unique and tailored solutions are required to meet the specific needs. Exploitation of deep and weak rock deposits are commonly performed by longwall mining, room-and-pillar mining, and stope-and-pillar mining methods. Alternatively, solution mining proposes various advantages for soluble minerals. Selection of a suitable mining method conforming the orebody characteristics and providing the best economy with operational safety is the most critical stage of mine planning to ensure the long-term success. Following sections briefly describe the viable underground mining methods for extraction of deep tabular deposits.

2.1.1 Room and Pillar Mining

Room-and-pillar mining is a widely used open-stoping method in horizontal or nearly horizontal deposits of metal, coal, trona, potash, salt, limestone, and sandstone. It operates by creating a series of stopes or rooms within the orebody. The in-situ rock left in-between the stopes acts as a pillar for supporting the vertical loads (Bullock, 1998). History of the room-and-pillar mining method dates back to 1500-1600 BCs in Hittites. It is believed that rock salt, a precious commodity of those times, in Çankırı, Turkey was exploited by this method (Timur et al., 2014). Room-and-pillar mining is still popular for metallic and non-metallic ores (Figure 2.2). In USA 60% of salt, 100% of potash, 80% of soda ash, 90% of lead, and 60% of zinc mines are exploited by room-and-pillar mining (Zipf, 2001). Also, 85% of coal production in China, 50% in Australia and 43% in South Africa is conducted by room-and-pillar mining (Tien, 2011). The method is viable for horizontal orebodies but 20-30^0 dip angles are also operated by inclined mining and/or step mining. For the former, stoping is done in accordance with the dip of the orebody while for the latter horizontal stoping with steps is adapted. The difference between the inclined mining and step mining is the suitability of mobile equipments in step mining while it is not possible in inclined mining due to the gradient of the orebody (Hamrin, 1982). The pillar layout and and dimensions are adjusted considering the orebody charactheristics and geomechanical properties. For instance, the pillar width may be smaller than the room in the hard-rocks while it should be larger in weak-rocks. In addition to that, weak-rock mines can usually be planned to the last detail and most of the room-and-pillar metal mines try to mine with a regular pattern as possible by considering the deviation. In the room-and-pillar method, before mining operation starts, entries and rooms are developed from the entry to the far end of the section. Often, production can simultaneously start with development since it is performed within the orebody. For development and production, room-and-pillar mining employs either conventional or continuous mining equipment, which produces nearly identical outcomes with subtle differences (Stefanko, 1983). Production

methods vary based on practical and financial considerations. When the entire vertical extent of a specific seam's ore is extracted from the advancement of one face, no mineral of economic significance is left behind. Conversely, where it is not practicable to carry the entire vertical height of the face, multiple slicing, also known as multiple-pass mining, could be used. Portions of the face known as the breasts. It occasionally becomes necessary in orebodies with uneven shapes (Bullock, 1998). Different pillar types, like yield pillars may be utilized which may be preffered to provide a temporary support by adjusting the pillar dimensions as to offer operational safety only during the work or barrier pillars which extend on a larger span for contributing to the global stability of the mine by setting an off-set between the workings and the discontinuites, protecting the main roads, suppressing the deformations in adjacent production regions, and isolating the water-bearing old mine openings. Moreover, as a secondary extraction method, pillar recovery is performed. This operation is unique for every orebody and ore type but in general it can be done by partially extracting the high grade zone on the pillar, removing high grade pillar completely while low grade pillars are left, or removing high grade pillar after back-filling. The boundary between the unmined pillars and the gob must always be maintained as a straight line. This is a crucial aspect of pillar recovery. The unmined pillar could violently collapse if it protrudes into the gob because it will receive significantly more pressure from the roof (Peng, 1978). Being versatile and relatively simple, the room-and-pillar technique is a popular mining method for hard-rock mines (Begg & Pohrivcak, 1998; Carmack et al., 1998; Korzeniowski & Stankiewicz, 1998; Lane et al., 1998; Marco et al., 1998; Nelson, 1998) as well as low strength rock mass where opening stability and surface subsidence needs to be cared extensively (Fortney, 1998; Herne & McGuire, 1998; Livingstone et al., 1998; Roberts, 1998). Apart from the advantages, in conventional cyclic mining practice, which is a flow of tasks following each other, may cause fail in any of the steps and the whole operation may be affected. However, modern continuous miners are capable of overcoming this problem. In any case, maintenance of the roof, limited stand-up time in swelling ground, decreasing extraction ratio by increasing pillar size

due to increasing depth (Bullock, 1998), and capital expenditures of the machinery are still major disadvantages.

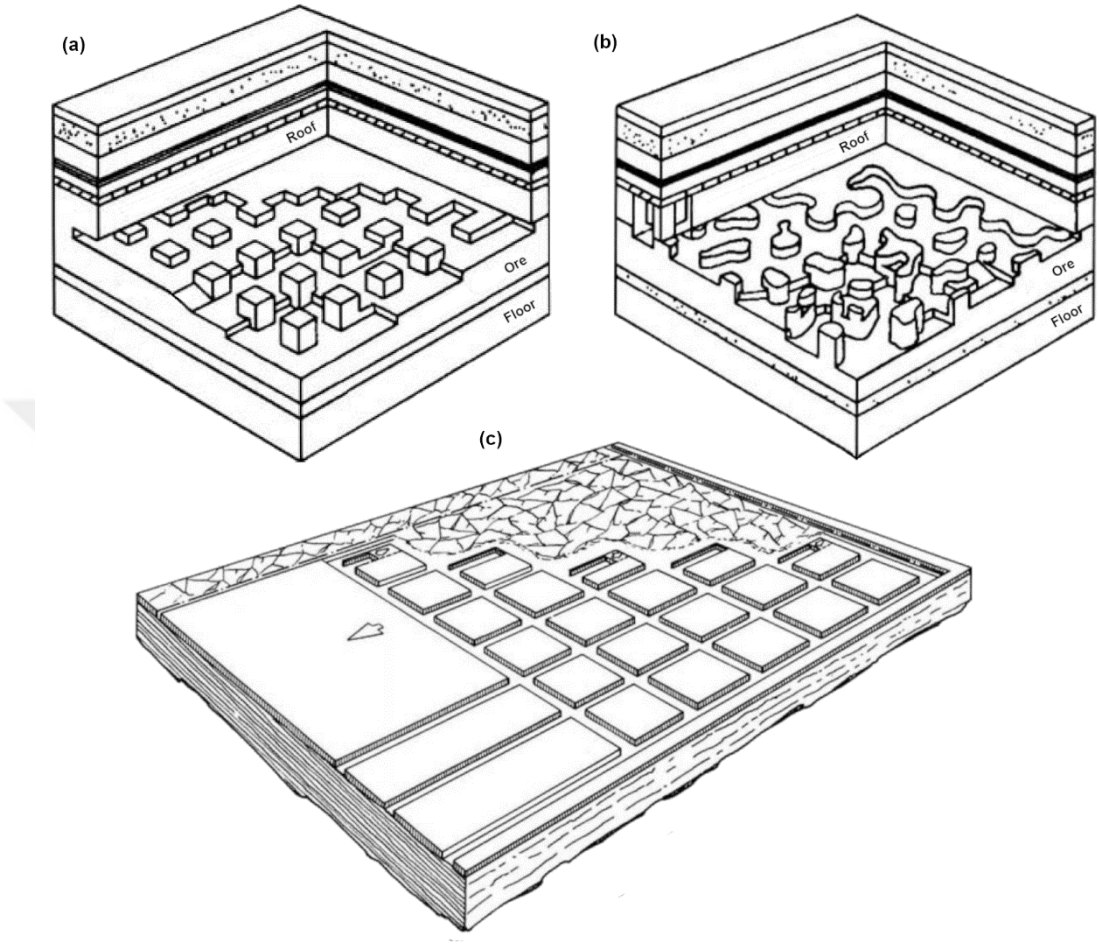

Figure 2.2 Room and pillar mining (a) in a regular pillar layout in hard rock (after Martens & Assoc., 1972) (b) in a random pillar layout in hard rock (c) in a coal mine (Paulick, 1963)

2.1.2 Longwall Mining

The longwall mining method is widely used for the extraction of sedimentary seams with large horizontal extent (ie., coal, trona, and potash as well as reef-type gold deposits like in South African gold mines) (Hamrin, 2001). It is a suitable method for both hard-rock and weak-rock ores by employing high mechanization. In longwall mining, simply, ore is extracted along a straight front in slices within a

narrow and supported stope close to the face. The longwall mining system simply utilizes a support system (four or two leg shields for the face), a shearer, and a haulage system (conveyors). For coal, trona, and potash with various seam thicknesses, the operation can be fully mechanized (Corkum & Board, 2016; Peng & Chiang, 1984) by using plows or drum shearers instead of conventional drill and blast sequence. Longwall is also used for hard-rock ores with different characteristics (Carter, 2001; Jameson & Ackerman, 2001; MacDonald & Singh, 2001). In general favorable ore and host rock characteristics for a potential longwall mine is low ore rock, weak to moderate host rock strength, and also tabular, flat, uniformly distributed thin, large orebody (Nieto, 2011). Although preferable ore thickness is thin (Hamrin, 1998), in some instances of thick orebodies, longwall mining can be used. For example in Turkey, where the majority of the lignite reserves are thick coal seams, single pass longwall (SPL), multi-slice longwall (MSL), and longwall top coal caving (LTCC) are used (Özfırat et al., 2005). Two major methods of LTCC are practiced in coal mines where both of them use armored face conveyors (AFC) (Figure 2.3) with differences in placement and usage (Bessinger, 2011). Longwall mines may operate either with advance or retreat systems (Stefanko, 1983) (Figure 2.4). Basically, in the advancing system, the longwall face propagates away from the main entry while gate roads are being developed simultaneously. In the retreat system, entries of the previous panel's main gate become a tailgate for the next panel.

Besides low flexibility and selectivity, relatively high recovery percentage, low cost, and low dilution percentage (Lishchuk et al., 2018) make longwall mining superior to room-and-pillar mining. In addition to that, in some coal mines with LTCC recovery rates are above 90% with an average of around 75% in the world (Çelik & Özçelik, 2021). On the contrary, by increasing depth, the floor and rock burst problems are encountered in coal (Peng, 2006), and especially in brittle salt deposits like trona and potash (Minkley & Lüdeling, 2015).

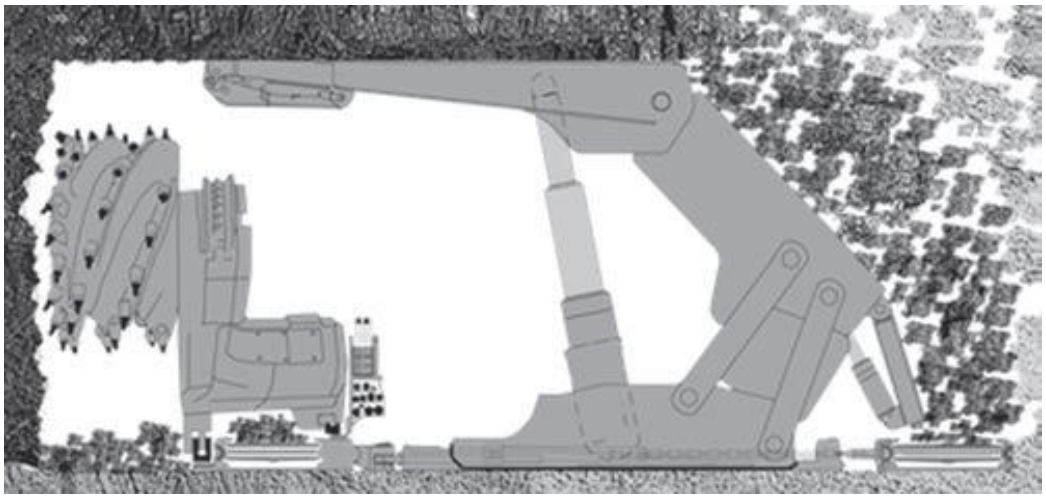

Figure 2.3 A typical LTCC method with AFC (Bessinger, 2011)

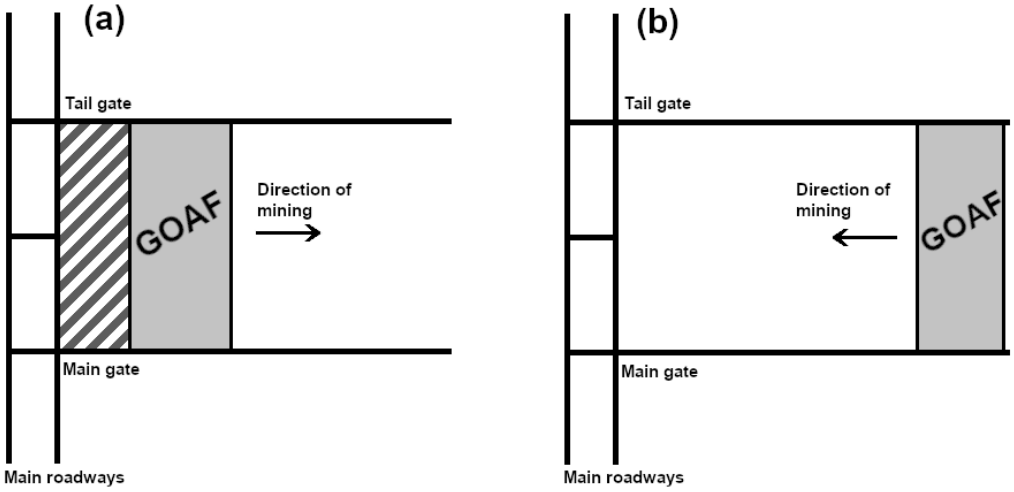

Figure 2.4 Longwall mining with (a) advance and (b) retreating systems

2.1.3 Solution Mining

Solution mining refers to the exploitation of ore via chemical methods instead of conventional mechanical excavation. In-situ solution mining, not to confuse with surface variations (Schlitt, 2011), is dissolving the orebody in-place and recovering the solution with the help of boreholes from the surface. Although the method is not widely used and categorized in underground mining operations (Boshkov & Wright, 1973; Hartman, 1987; Morrison, 1976), its history dates back to the early 1940s for

the mining of trona ore (Pike, 1943). This method could be employed to produce potash, nahcolite, and trona as well as precious metals, copper, manganese, and uranium (Chamberlin, 2009). The economic advantages arising from the low development and exploitation cost of bedded deposits, make in-situ leaching a favorable method. In addition, low capital expenditure and operating costs, and low development time are other advantages of solution mining. Also, the cost-effectiveness of the method gives the ability to exploit the low-grade ores (i.e. an average of 30% trona recovery rate in contrast to countertypes with an average of 45% (Kyle et al., 2011). Various techniques are available for extraction with solution mining. The differences are caused by the variations in the geological settings, the mechanical properties of the ore, the required production rates, and other constraints like the presence of an aquifer. For the salt and potash ores generally single or dual well setup is applied as can be seen in Figure 2.5. In single-well solution mining, a vertical well is drilled into the orebody by installing a casing and inner tubing. The injection is done from the inner tube where the collection of the solution is conducted from the casings **(**Figure 2.5.a). In multiple-well or dual-well applications the vertical wells are used for either injection or recovery **(**Figure 2.5.b). Another version of the multiple vertical wells is called "piste", which is used by the Solvay Company (Daupley et al., 2005). This method embraces a series of vertical boreholes drilled into the floor of the deposit. When all the boreholes are joined to each other, fresh water is injected into the boreholes located in the front while the brine is extracted from the backward **(**Figure 2.5.c). Alternatively, the horizontal and vertical well combinations could be used. This setup comprises one horizontal well drilled to the bottom-most of the orebody and acts as an injection well. After then, a single (Figure 2.5.d), dual (Figure 2.5.e), or multiple vertical wells are connected to the horizontal well to act as a brine recovery well/s. As mentioned earlier, according to the specific conditions and needs, different well setups could be designed. Apart from the vertical well setups, some applications only consist of horizontal wells that are connected (Figure 2.5.f).

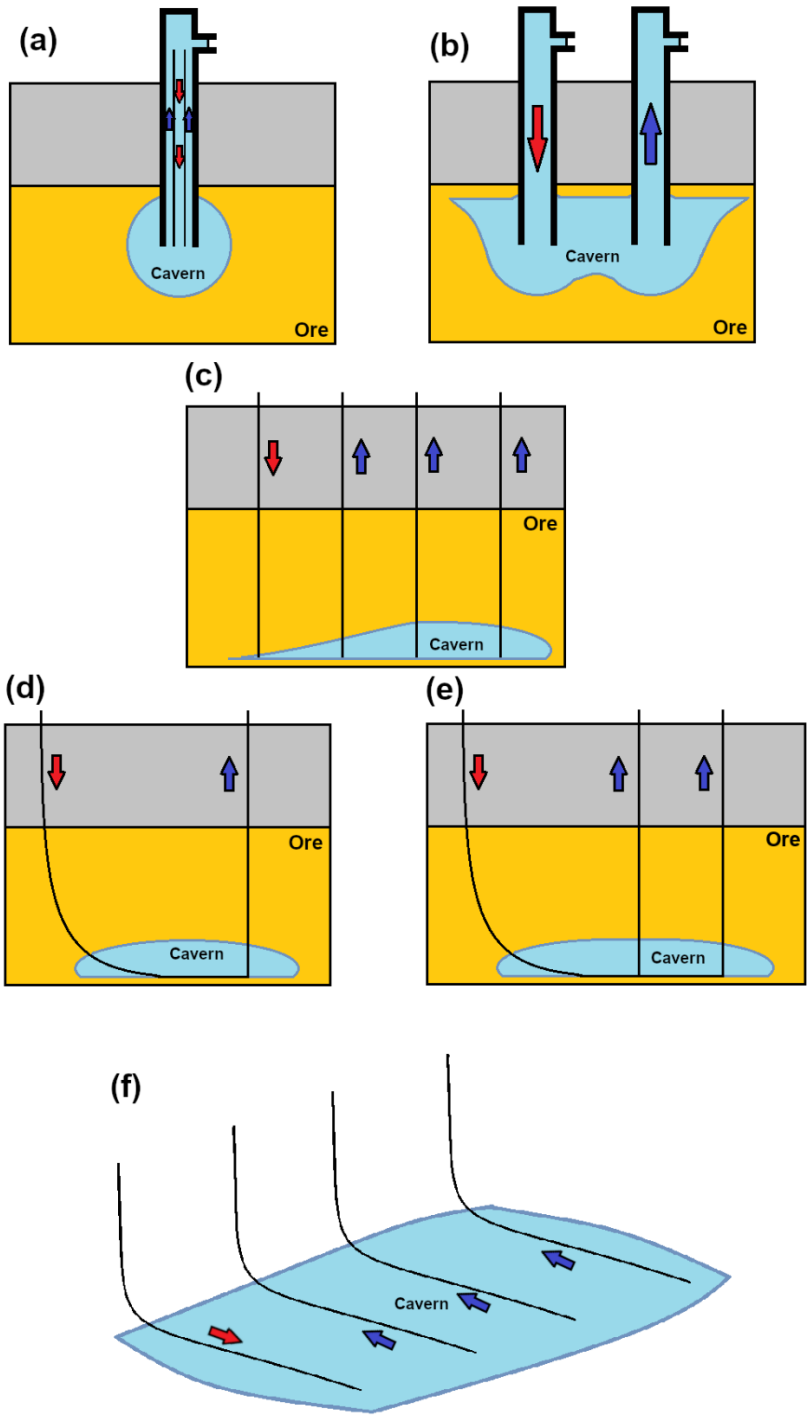

Figure 2.5 (a) single vertical well (b) dual vertical well (c) piste (d) horizontal well with single vertical and (e) dual vertical well (f) multiple horizontal well solution mining setup

The in-situ solution mining technique also provides a cost-effective waste management scheme since bulk volumes of waste rocks are left in place with low environmental impacts compared to conventional mining. With the proven effectiveness of the method, in-situ solution mining as mentioned before implemented and used to produce other types of mineral deposits such as rock salt and nahcolite (Hardy et al., 2003; Nielsen et al., 2004) as well as uranium like in Kazakhstan and Uzbekistan (Hore-Lacy, 2004). As an industrial mineral that can be exploited by in-situ solution mining methods, trona, nahcolite, and wegscheiderite are the natural resources of soda ash where Turkey has the second biggest trona reserves in the world in the Beypazarı and the Kazan districts of Ankara. The end product of the trona is soda ash and sodium bicarbonate. Soda ash, in other words, sodium carbonate, is a rapidly growing industry with $1.8 billion in total domestic value and a 20% demand increase in the USA (USGS, 2022). In the Beypazarı and Kazan districts, both trona deposits are exploited by solution mining operations since 2009 and 2011 (Eti Soda, 2020). This makes trona solution mining an important topic for Türkiye. Despite its economic and operational advantages, the method has its own challenges. The first problem is due to the complex chemical nature of the ore itself where sodium bicarbonate blinding, a phenomenon that dramatically decreases the recovery ratio. It occurs when bicarbonate ions produced during the dissolution process deposit again on the ore's exposed surface, resulting in the buildup of carbonate deposits and a corresponding decrease in the efficiency of mineral dissolution and recovery. Blinding can result in significant mineral reserves being left unextracted from the mine. To overcome this, various studies and innovations were made (Phillip & Vandendoren, 2006). Also, impurities between the beds where thin trona bed intercalations present are another problem in terms of the exploitation of the ore. Besides, geomechanical problems exist for all types of solution mining. One of the major geomechanical problems is the early collapse of the cavern roof well-before the production is completed. Regardless of the differences in the geology of the overlaying strata and the applied method of in-situ solution mining, there are several occasions that serious cavern roof collapses are reported in the USA, France,

Italy, and China (Zhang et al., 2018). In this manner, the stability of the caverns is studied by numerous researchers (Liu et al., 2020; Xiao et al., 2016; Zhang et al., 2023). The cavern stability is an important topic since any anomalies in the stress could fail the pillars between caverns. Especially fields that employ multiple cavern production (Figure 2.6) where aquifers must be protected or surface subsidence is restricted. Surface subsidence attracts most of the researchers' interest. From conventional on-surface methods to sophisticated satellites are employed to monitor and predict subsidence (Morgan et al., 2018). In addition to operational threats, there are several works done for the abandonment of the field. Post-mining conditions of several solution mining fields in the Netherlands (Kroon et al., 2003) and also in France by employing micro-seismic monitoring (Contrucci et al., 2011) are studied. Post-mining condition studies will continue to increase since the post-mining usage of the developed caverns is a trending exercise. Post-mining usage as storage for natural gas (Li et al., 2022; Liang et al., 2022), CO_2 (Shi & Durucan, 2005), and H_2 (Abreu et al., 2023) were studied by various researchers.

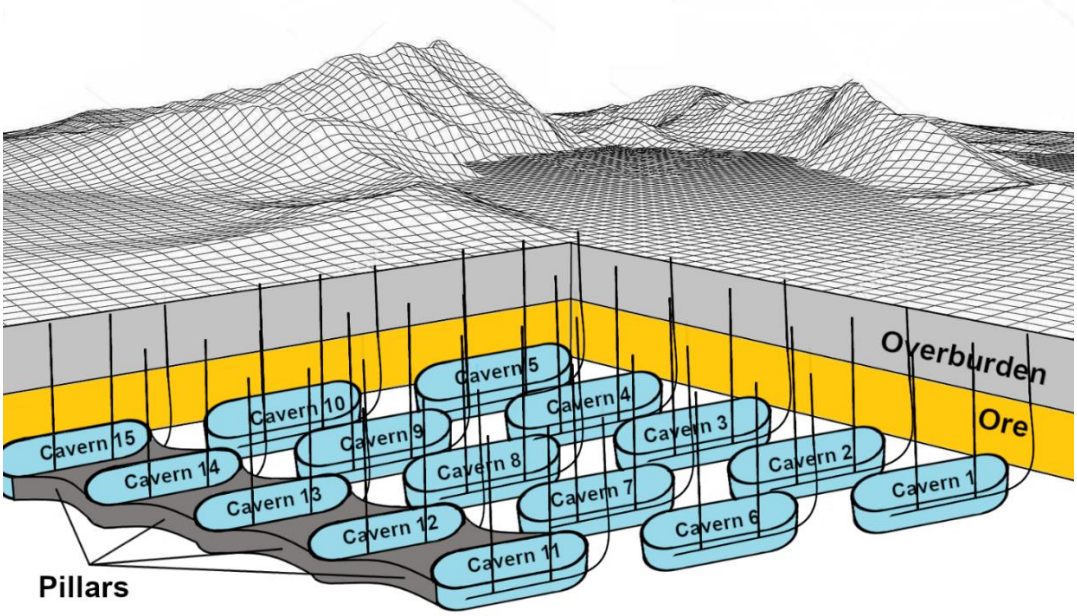

Figure 2.6 Representation of multi-cavern production of solution mining with horizontal and vertical well combination

2.2 Geomechanical Classification of Rock Mass

Since the early ages of civilization, comprehension of the mechanical behavior of the earth takes the interest of humans (Aristotle, 350 B.C.). Rock mass geomechanical characteristics are important indicators of the efficiency and economy of any rock engineering project. They are also effective in the mining method selection, mine layout design, production sequencing, and many other aspects related to production. Classification of rock mass quality is an empirical approach that relies on historical data to make predictions about the field scale behavior of rocks. This section presents a brief overview of the history and the recent development in rock mass quality characterization.

2.2.1 Premises

Humankind started to deal with geomechanical problems once they interacted with and modified the earth material for their own benefit. However, the systematic interpretation of geological material with force based on mechanical laws dates back to the early stages of the industrial revolution. In 1773, Coulomb tested some Bordeaux rock samples to identify their mechanical characteristics (Coulomb, 1776). Nearly a century later, after the starting of the construction of the Panama Canal by France in 1884, the US Army Corps of Engineers took over the task and recorded 60 slides between 1910 and 1964 (Lutton et al., 1978). These are addressed later in 'The First Soil Mechanics and Foundation Engineering Conference' by Terzaghi (Terzaghi, 1936). In a retrospective, it can be said that the first systematic approach to the mechanics of geological materials, later developed as geotechnic, is performed by Josef Stini at Vienna Technical University (Hoek, 2007). Since then, rock mass classification schemes have been developed for various purposes ranging from the first empirical approaches (Ritter, 1879) to the modern day the rock quality designation (RQD), rock mass rating (RMR), Q-system, and geological strength index (GSI) systems. Early classification systems are given in Table 2.4.

Table 2.4 Summary of the rock mass classification systems (after Cosar, 2004; Ünal & Özkan, 1996; Yardimci, 2013)

Name	*Researcher(s)*	*Country*	*Applications*
Rock Load	Terzaghi, 1946	USA	Tunnels with Steel Support
Stand-up Time	Lauffer, 1958	Australia	Tunneling
New Austrian Tunneling Method (NATM)	Pacher et al., 1964	Austria	Tunneling
Rock Quality Designation (RQD)	Deere et al., 1967	USA	Core Logging, Tunneling
Rock Structure Rating (RSR)	Wickham et al., 1972	USA	Tunneling
Rock Mass Rating (RMR)	Bieniawski, 1973 (last modification 1989-USA)	South Africa	Tunneling, Mining
RMR Extensions	Weaver, 1975	South Africa	Rippability
	Laubscher, 1977	South Africa	Mining
	Olivier, 1979	South Africa	Weatherability
	Ghose and Raju, 1981	India	Coal Mining
	Moreno Tallon, 1982	Spain	Tunneling
	Kendorski et al., 1983	USA	Hard Rock Mining
	Nakao et al., 1983	Japan	Tunneling
	Serafim and Pereira, 1983	Portugal	Foundations

Table 2.4 continued

	Gonzalez de Vallejo, 1983	Spain	Tunneling
	Ünal, 1983	USA	Roof Bolting in Coal Mines
	Romana, 1985	Spain	Slope Stability
	Newman, 1985	USA	Coal Mining
	Sandbak, 1985	USA	Boreability
	Smith, 1986	USA	Dredgeability
	Venkateswarlu, 1986	India	Coal Mining
	Robertson	Canada	Slope Stability
Modified Rock Mass Rating (M-RMR)	Ünal and Özkan, 1990	Turkey	Mining
Rock Mass Quality (Q)	Barton et al., 1974 (last modification 2002)	Norway	Tunneling, Mining
Q Extensions	Kirsten, 1982	South Africa	Excavability
	Kirsten, 1982	South Africa	Tunneling
Strength-Block Size	Franklin, 1975	Canada	Tunneling
Basic Geotechnical Classification	ISRM, 1981	International	General
Rock Mass Strength (RMS)	Stille et al., 1982	Sweden	Metal Mining
Unified Rock-Mass Classification System (URCS)	Williamson, 1984	USA	General

Table 2.4 continued

Communication Weakening Coefficient System (WCS)	Singh, 1986	India	Coal Mining
Rock Mass Index (RMi)	Palmström, 1996	Sweden	Tunneling
Geological Strength Index (GSI)	Hoek and Brown, 1997	Canada	All Underground Excavations

2.2.2 Commonly Used Rock Mass Classification Systems (RMR, Q-Index & GSI)

In the preliminary stages of earth-construction projects, rock mass characterization systems are useful as the knowledge of the stress state, hydrological conditions, structural discontinuities, and geological characteristics are very limited. It also facilitates communication between various engineering branches and simplifies the comprehension of the geomechanical condition. Despite all the advantages, it is important to consider that rock mass categorization systems alone will not be sufficient to replace more sophisticated analysis techniques (Hoek, 2007). Today, commonly accepted rock mass classification systems are RMR (Bieniawski, 1973), the Q-system (Barton et al., 1974), and GSI (Hoek, 1994). However, RQD constitutes a basis for the majority of these recent methods (Deere et al., 1967).

RQD is the percentage of intact core pieces that are longer than 100 mm in the total length of the drill core. In-situ rock mass quality can be quantitatively estimated by using RQD based on the fracture density. Determination of RQD needs extra attention since mechanical cracks that occurred during the handling and recovering

of the cores could alter the results as well as borehole orientation. Rock mass quality according to the RQD is given in Table 2.5.

Table 2.5 Interpretation of the 'Rock Quality Designation' (RQD) (after Deere et al., 1967)

RQD Value	*Rock Mass Quality*
<25	Very Poor Rock
25 – 50	Poor Rock
50 – 75	Fair Rock
75 – 90	Good Rock
90 – 100	Excellent Rock

The RMR system is an output of Bieniawski's experiences in tunneling for many years. Since the first publication, there have been many improvements by its original author and other researchers (Bieniawski, 1989). The system divides rock mass into structural domains by considering discontinuity characteristics, geological properties, and mechanical performance. While UCS of intact rock, RQD, and discontinuity spacings are taken into account, in-situ stress conditions are not included. Still, RMR is a popular system that finds a wide range of use in earth-construction projects. Ratings and classification of rock mass according to the RMR_{89} system are given in Table 2.6.

Table 2.6 Interpretation of the 'Rock Mass Rating (RMR_{89})' system (after Bieniawski, 1989)

Rating	100 – 81	80 – 61	60 – 41	40 – 21	<21
Class Number	I	II	III	IV	V
Description	Very Good Rock	Good Rock	Fair Rock	Poor Rock	Very Poor Rock

Q-system was developed by the Norwegian Geotechnical Institute (NGI) (1974) to assist in tunnel excavations and to determine the support requirements. The Q-system, or tunneling quality index (Q), is based on the study of old Scandinavian tunneling cases and considers three ratios that reflect the characteristics of the rock mass by block size, inter-block frictional strength, and active stress (Figure 2.7). With the latter component, it differs from the RMR system.

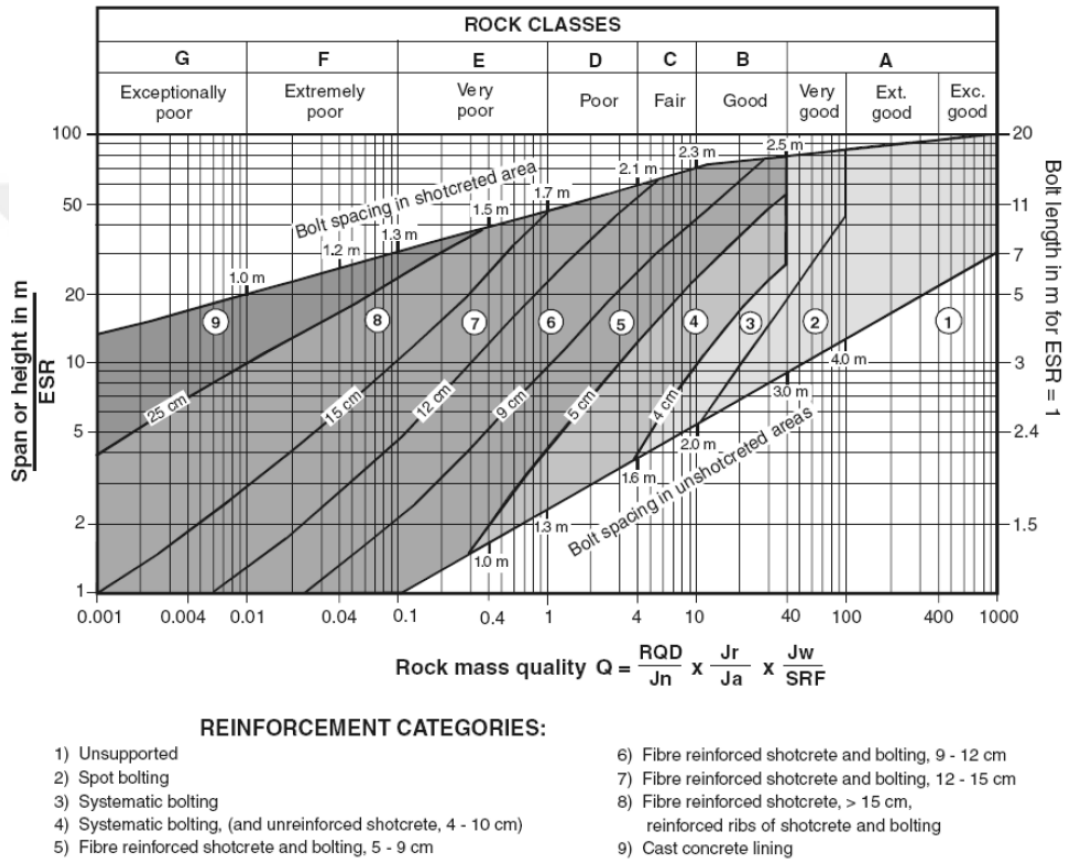

Figure 2.7 Interpretation of the Q-Tunneling Index and estimated support categories (after Grimstad & Barton, 1993, taken from Hoek, 2007)

Calculation of the RQD is done by equation 1:

$$RQD = \frac{\sum core\ pieces > 100mm}{Total\ length\ of\ core} \times 100 \quad (1)$$

Q index is calculated as given in equation 2 where J_n is the joint set number (varies from 0.5 to 20), J_r is the joint roughness (varies from 0.5 to 5), J_a is the alteration

(varies from 0.75 to 20), J_w is the water reduction factor (varies from 0.5 to 1.0), and SRF is the stress reduction factor (varies from 0.5 to 20).

$$Q = \left(\frac{RQD}{J_n}\right) \times \left(\frac{J_r}{J_a}\right) \times \left(\frac{J_w}{SRF}\right) \quad (2)$$

To combine two classification systems, Bieniawski (1976) developed a correlation which is given in equation 3:

$$RMR = 9 \log Q + A \quad (3)$$

where A with an average value of 44 with respect to case histories in tunneling and changes between 26 and 62.

For rock masses that have a GSI value above 25 and RMR is greater than 23, the value of GSI could be determined from equation 4:

$$GSI = RMR_{89} - 5 \quad (4)$$

If the GSI value is smaller than 25 that means poor rock conditions and the correlation between RMR and GSI is no longer trustable. So, for poor rock masses, RMR value should not be used to estimate GSI value. However, for poor rocks, by using equation 5, GSI can be calculated from Q values:

$$GSI = 9 \ln Q \quad + 44 \quad (5)$$

Both RMR and Q classification systems were developed to solve problems swiftly and turn decision-making into a more quantitative process. Furthermore, it is important to consider that RMR considers only the strength while Q also includes the in-situ stresses. For the determination of rock mass properties based on classification systems many statistical models have been proposed (Aydan et al., 2014).

The GSI system was developed to determine the rock mass properties for use in the analytical and numerical assessment of rock constructions. It uses four main parameters and discontinuity conditions to estimate the Hoek & Brown strength criterion for rock masses, deformability of the rocks, and strength of the rock by using modified relationships from other classification systems (Figure 2.8). It is

recommended to use a range of GSI values instead of a single value since the rock mass properties may vary.

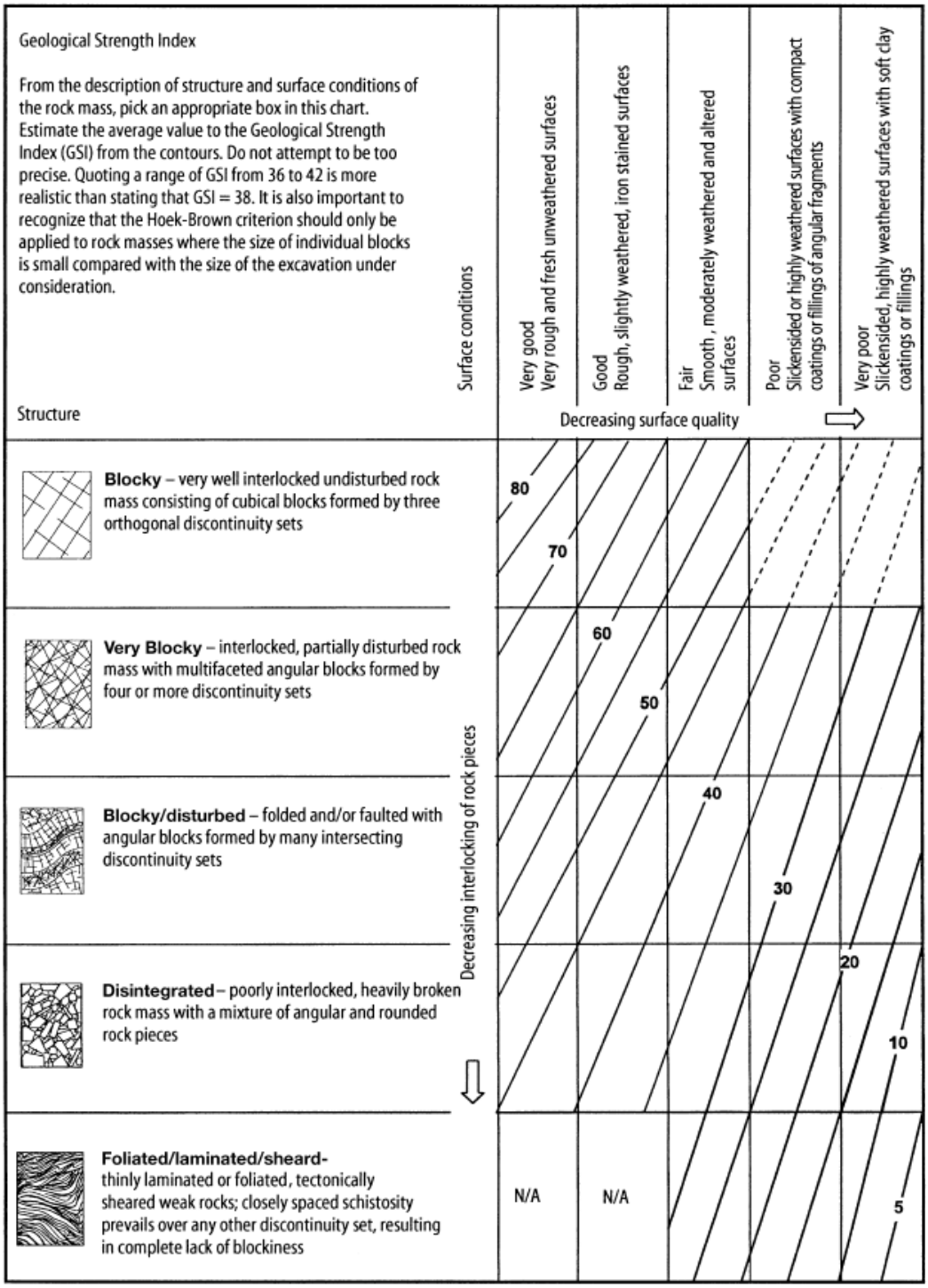

Figure 2.8 GSI interpretation table (Hoek et al., 1998)

2.2.3 The Recent Developments

The Q-System has undergone numerous revisions as a result of the incorporation of new data and advancements in excavation support techniques and technologies. These modifications have resulted in new relationships and support modifications (Barton, 2002). A normalizing factor was introduced to the original Q-value for hard rocks, resulting in a new value Q_c as shown in equation 6, after it was realized that the engineering properties are influenced by the uniaxial compressive strength (σ_c) of the intact rock between discontinuities.

$$Q_c = \left[\frac{RQD}{J_n}\frac{J_r}{J_a}\frac{J_w}{SRF}\right]\frac{\sigma_c}{100} \tag{6}$$

Also, with the advancements the correlation between the modified Q value, the Seismic Velocity V_p, Depth (H), Rock Mass Modulus, Required Support Pressures (P_r), Porosity, and Uniaxial Compressive Strength ($\sigma_{c)}$ has been determined and is shown in the form of a chart (Barton, 2002) (Figure 2.9). Also, usage area of the Q-system is extended to slope stability calculations by equation 7 (Barton & Bar, 2015). The term J_w is replaced by J_{wice} to take more environmental considerations into account. From the chart (Figure 2.10) it can be decided that whether slope is stable or not with the calculated slope angle.

$$Q_{slope} = \left(\frac{RQD}{J_n}\right)\left(\frac{J_r}{J_a}\right)_0\frac{J_{wice}}{SRF_{slope}} \tag{7}$$

In addition to that, correlation of the different rock mass properties is generally unsuccessful (Aydan & Ulusay, 2013). Because of that, the rock mass quality rating (RMQR) (Aydan et al., 2014) was developed to consider all rock mass classification systems with relevant parameters. The rating system considers the discontinuity set number (DSN), discontinuity spacing (DS), and discontinuity condition along with the degradation degree (DD) of intact rock, groundwater seepage condition (GWSC), and groundwater absorption condition (GWAC). RMQR value is the sum of these six parameters (Figure 2.11).

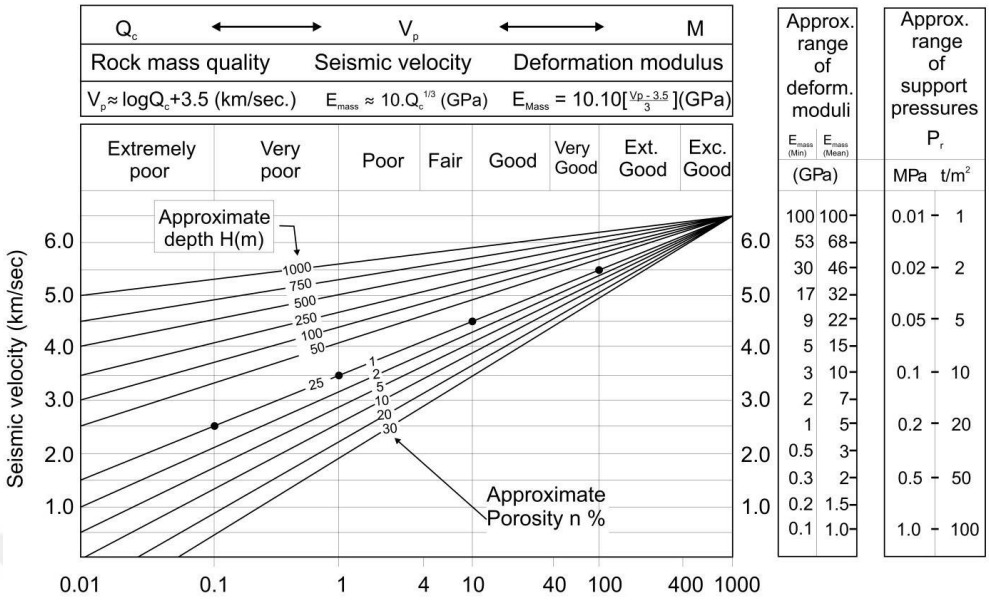

Figure 2.9 Modified Q chart

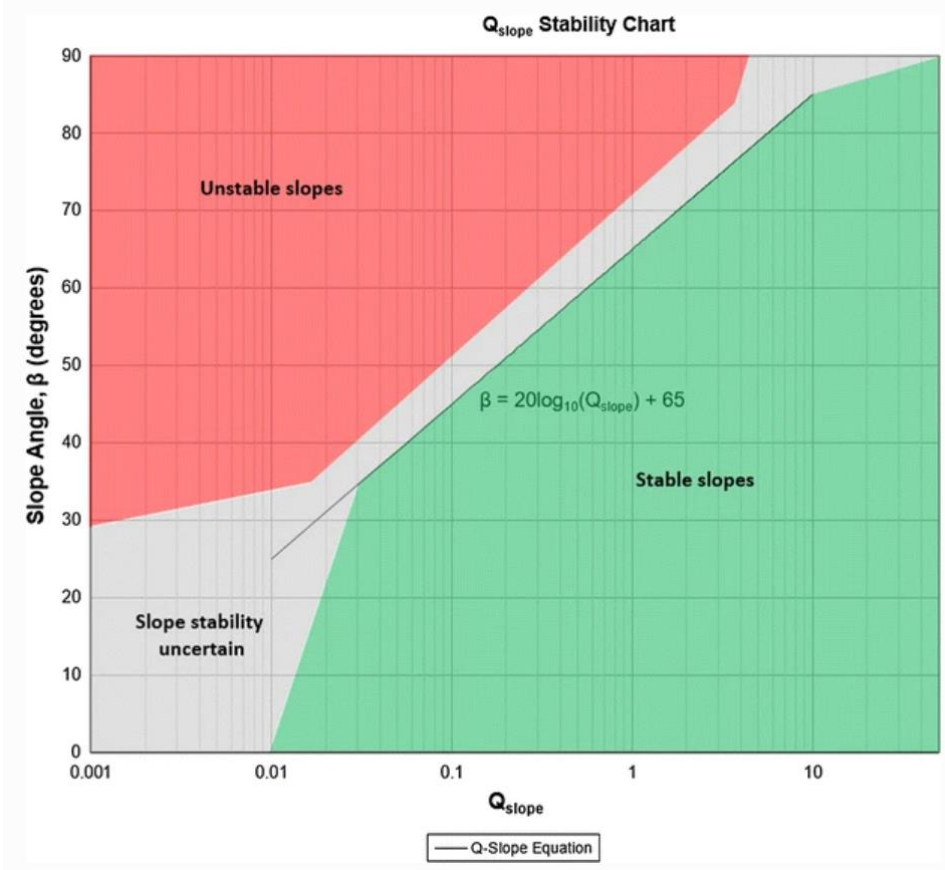

Figure 2.10 Q-slope stability chart

Degradation degree (DD)	Fresh		Stained		Slight degradation		Moderate degradation		Heavy degradation				Decomposed
Rating (R_{DD})	15		12		9		6		3				1-0
Discontinuity set number (DSN)	None (solid or massive)		One set plus random		Two sets plus random		Three sets plus random		Four sets plus random				Crushed or shattered
Rating (R_{DSN})	20		16		12		8		4				1-0
Discontinuity spacing (DS)	None or DS ≥ 24 m		24 >DS ≥ 6 m		6 m>DS ≥ 1.2 m		1.2 m > DS ≥ 0.3 m		0.3 m>DS≥0.07 m				0.07 m > DS
or RQD	100						100 > RQD ≥ 75		75 > RQD ≥ 35				35 > RQD
Rating (R_{DS})	20		16		12		8		4				1-0
Discontinuity condition (DC)	None		Healed or intermittent		Rough		Relatively smooth and tight		Slickensided with thin infill or separation (t < 5 mm)				Thick fill or separation (t > 10 mm)
Rating (R_{DC})	30		26		22		15		7				1
or , alternatively, excluding "None" and "Healed or intermittent" classes													
Discontinuity condition (DC) $R_{DC}=R_{DCA}+R_{DCI}+R_{DCR}$	Aperture or separation				None or very tight, <0.1 mm		0.1–0.25 mm		0.25–0.5 mm		0.5–2.5 mm		2.5–10 mm	>10 mm
	Rating (R_{DCA})				6		5		4		3		2	1
	Infilling				None		Surface staining only		Thin coating <1 mm		Thin filling 1 < t < 10 mm		Thick filling 6 > t >10 mm	Very thick filling or shear zone t > 60 mm
	Rating (R_{DCI})				6		5		4		3		2	1-0
	Roughness		Descriptive		Very rough		Rough		Smooth undulating		Smooth planar		Slicken-sided	Shear band/zone
			Profile No. in Fig. 9		10	9	8	7	6	5	4	3	2	1-0
	Rating (R_{DCR})				10	9	8	7	6	5	4	3	2	1-0
Groundwater seepage condition (GWSC)	Dry		Damp		Wet		Dripping		Flowing				Gushing	
Rating (R_{GWSC})	9		7		5		3		1				0	
Groundwater absorption condition (GWAC)	Non-absorptive		Capillarity or electrically absorptive		Slightly absorptive		Moderately absorptive		Highly absorptive				Extremely absorptive	
Rating (R_{GWAC})	6		5		4		3		2				1-0	

Figure 2.11 Interpretation table of RMQR (Aydan et al., 2014)

2.3 Determination of the Geomechanical Properties of Rocks

Rock testing is necessary to understand the rock behavior and performance under load. The slope and excavation designs rely on the geomechanical parameters obtained from laboratory scale or in-situ rock tests. Numerical simulations require a representative rock material model involving the isotropic or anisotropic nature of the geological material. Also, the knowledge about the in-situ stresses and rock mass properties contributes to the representativeness of the models. To this extent, The International Society of Rock Mechanics and Rock Engineering (ISRM) has published a guidebook "The Suggested Methods" (SM) for regulation of the rock testing procedures. As with other institutes like American Society for Testing and Materials (ASTM) and German Institute for Standardization (DIN), the ISRM specifies requirements and the SM is more of a guide rather than a must-follow book. Briefly, for laboratory and in-situ testing, the suggested categories are presented in Table 2.7.

Table 2.7 The rock tests (ISRM, 2007)

Category I: Classification & Characterization	
Rock Material (Laboratory Tests)	
1	Density, water content, porosity, absorption
2	Strength and deformability in uniaxial compression; point load strength
3	Anisotropy indices
4	Hardness, abrasiveness
5	Permeability
6	Swelling and slake-durability
7	Sound velocity
8	Micro-petrographic descriptions

Table 2.7 continued

Rock Mass (Field Observations)	
9	Joint systems; orientation, spacing, openness, roughness, geometry, filling, and alteration
10	Core recovery, RQD, and fracture spacing
11	Seismic test for mapping and as a rock quality index
12	Geophysical logging of boreholes
Category II: Engineering Design Tests	
Laboratory	
1	Determination of strength envelope (triaxial and uniaxial compression and tensile tests)
2	Direct shear tests
3	Time-dependent and plastic properties
In Situ	
4	Deformability tests
5	Direct shear tests
6	Field permeability, ground-water pressure, and flow monitoring; water sampling
7	Rock stress determination
8	Monitoring of rock movements, support pressures, anchor loads, rock noise and vibrations
9	Uniaxial, biaxial, and triaxial compressive strength
10	Rock anchor testing

Determination of the rock mass mechanical parameters can be performed both by the interpretation of laboratory tests with field studies and in-situ tests. This section briefly presents some significant testing methods.

2.3.1 Rock Mechanics Laboratory Tests

Laboratory testing makes it viable to determine the rock mechanics parameters using small-scale rock samples. Numerical simulations require elastic and plastic mechanical parameters like Young's modulus (E), Poisson's ratio (υ), internal friction angle (ϕ), and cohesion (c) as well as uniaxial compressive strength (UCS), tensile strength (TS), normal stiffness (K_n), and shear stiffness (K_s). Some of the laboratory tests and the associated parameters are given in Table 2.8.

Table 2.8 Rock Mechanics Laboratory Tests and Parameters

Test	*Parameters*
Deformability (ISRM, 2007)	UCS, E and υ
Ultrasonic Pulse Velocity (ISRM, 2014)	V_p, E, υ, and UCS
Uniaxial Compressive (ISRM, 2007)	UCS, Φ and c
Direct and Indirect Tensile (ISRM, 2007)	TS
Triaxial Compressive (ISRM, 2007)	Φ and c
Point Load (ISRM, 2007)	UCS
Direct Shear (ISRM, 2014)	Φ, c, K_n, and K_s

UCS is the ultimate uniaxial stress that rock could withstand without failure. The approximation of ϕ and c of the rock can be determined (ISRM, 2007).

There are two testing methods for TS, which are the direct tensile strength test and the indirect tensile strength test. The cylindrical specimen is subjected to direct uniaxial tensile load in the former. However, the uniaxial compressive force applied along the diameter fails the rock with a tensile crack in the latter testing scheme of the indirect tensile strength test (ISRM, 2007).

In the triaxial compressive strength test, the strength of the rock is determined as a function of confining pressure. The results of the test provide the values necessary to determine the strength envelope, which are ϕ and c (ISRM, 2007).

The deformability test intends to determine the stress-strain path of the rock to calculate E and υ. Under uniaxial compression, axial and circumferential strains are recorded with electrical gauges (ISRM, 2007).

Ultrasonic pulse velocity test relies on the generation, transmission, and reception of small amplitude ultrasonic pulse frequencies. By using the measurements, UCS, υ, and E can be calculated (ISRM, 2014).

The point load strength test is an index test for the determination of UCS. On average, UCS is 20-25 times the point load strength, where the ratio can vary between 15 and 50, especially for anisotropic rocks. Ranges for various index tests to determine UCS are given in Figure 2.12.

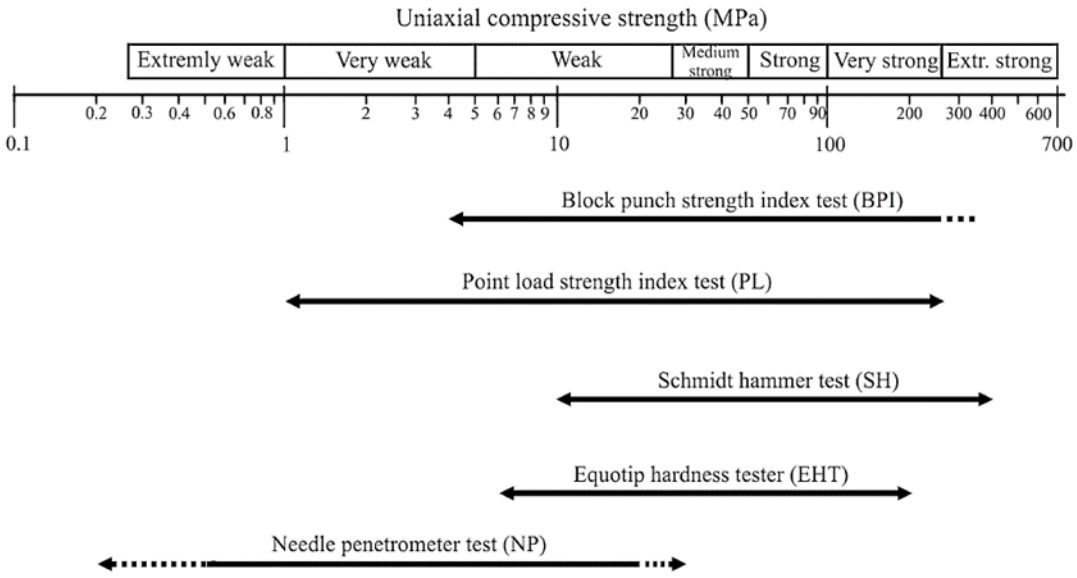

Figure 2.12 Ranges for various index tests to determine UCS (ISRM, 2014)

As a function of the stress normal to the sheared plane, the direct shear test quantifies the peak and residual direct shear strength. The test's result provides the values required for determining the discontinuity's cohesion and internal friction angle. Moreover, it is possible to determine the normal and shear stiffness (ISRM, 2014). The shear strength is crucial in the design of rock structures since the slide will most likely take place on the discontinuity plane. The cohesion and internal friction angle

are the parameters controlling this action. During direct shear testing, a constant normal load is exerted on the discontinuity plane. There is a class of engineering problems where the normal stress may not remain constant when sliding occurs, despite the fact that this boundary condition is appropriate for problems involving the sliding of rock blocks close to the ground surface in those situations. In other words, if the dilatation of a discontinuity is restrained, the stress on the sliding surface may alter (for example, around an underground excavation).

2.3.2 In-Situ Rock Test

In-situ rock testing allows for the determination of field-scale rock properties using direct methods. The plate test, also known as the uniaxial jacking test, measures the deformation characteristics of rock mass and is carried out in short tunnels or test adits. Elastic deformation and unloading moduli can be calculated using the data from incremental and cyclic loading. Also, the effects of anisotropy can be determined by orienting the thrust of the jack in any direction (ISRM, 2007). In Figure 2.13, a typical plate test equipment is given.

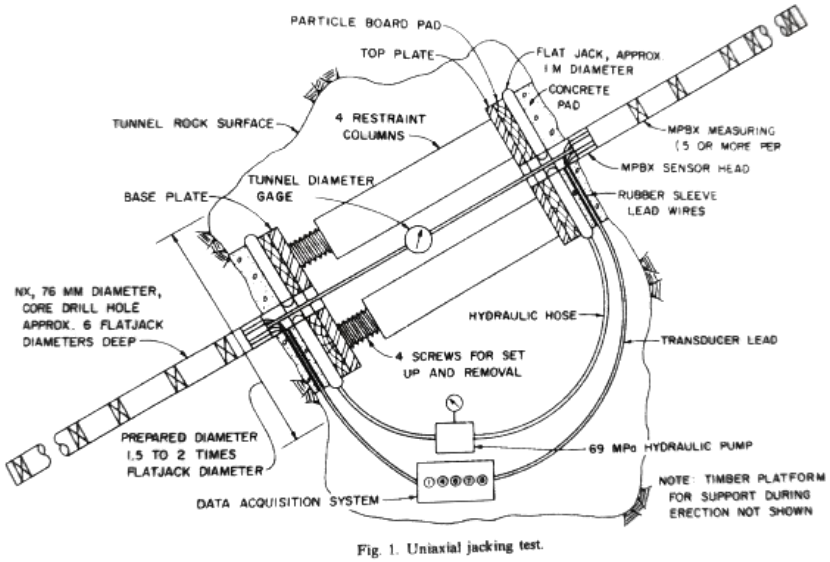

Figure 2.13 Plate test equipment (ISRM, 2007)

The direct shear test determines the maximum and remaining direct shear strength as a function of stress normal to the sheared plane. The results are used in limiting equilibrium analysis for foundations or slope stability analyses (ISRM, 2007). The purpose of shearing is to find out the peak and residual shear strength. The shear force is applied either in increments or continuously in such a way as to control the rate of shear displacement (Figure 2.14). A consolidation curve is plotted during the consolidation stage of testing.

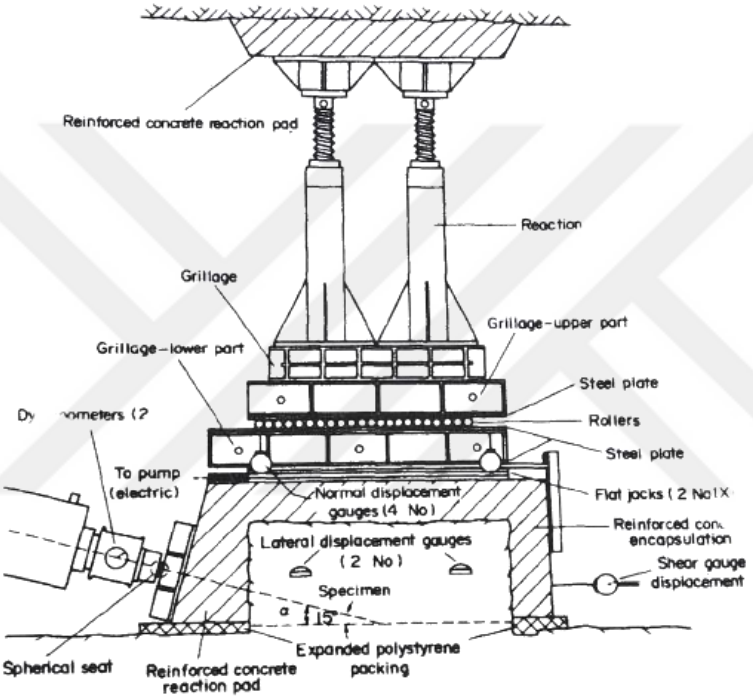

Figure 2.14 A typical set-up for an in-situ direct shear test

A flatjack consisting of two flat sheets of steel plates are used where a hydraulic pump loads the rock (Figure 2.15). With this method, the stress is measured parallel to the jack and near the exposed rock surface. Since each measurement only calculates stress in one direction, the stress tensor must be calculated from at least six measurements taken in separate directions. The average cancellation pressure will be calculated by plotting the closure and opening of each pair of pins against the applied pressure.

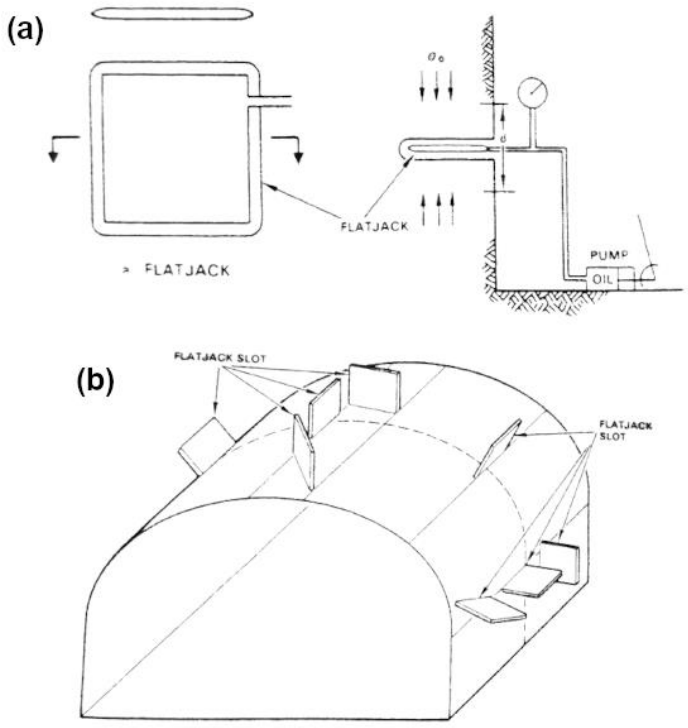

Figure 2.15 (a) A typical flatjack test equipment (b) a sample layout for the test

The overcoring technique relies on the principle that when a borehole is drilled the rock surrounding the borehole undergoes a stress relief, which leads to deformations around the hole. Using an appropriate instrumentation, the strains can be measured. Later, this data can be used to calculate the in-situ stress. Three types of commonly used instrumentations in overcoring technique is listed below:

- USBM Deformation Gage: Measures the change in borehole diameter. As the rock surrounding the borehole is relieved of stress, it undergoes elastic deformation. The USBM deformation gage monitors the change in diameter of the borehole, allowing for the calculation of stress relief.
- CSIRO Triaxial Strain Cell: Measures the strain around the borehole wall. It consists of gauge type sensors to detect the deformation of the rock in different directions. When stress is relieved through overcoring (Figure

2.16), the strain on the borehole wall changes, and the triaxial strain cell measures these alterations.

- Doorstopper: This method involves measuring the changes in strain on the flat end of the borehole. A doorstopper, which is a strain gauge, is placed against the flat end of the borehole. As stress is relieved, the strain on the flat end of the borehole changes, and this can be quantified using the doorstopper.

By knowing the elastic properties of the rock, such as Young's modulus and Poisson's ratio, the changes in borehole diameter or strains can be converted into estimates of the in-situ stress within the rock. This conversion is achieved through stress-strain relationships and the application of relevant equations or models.

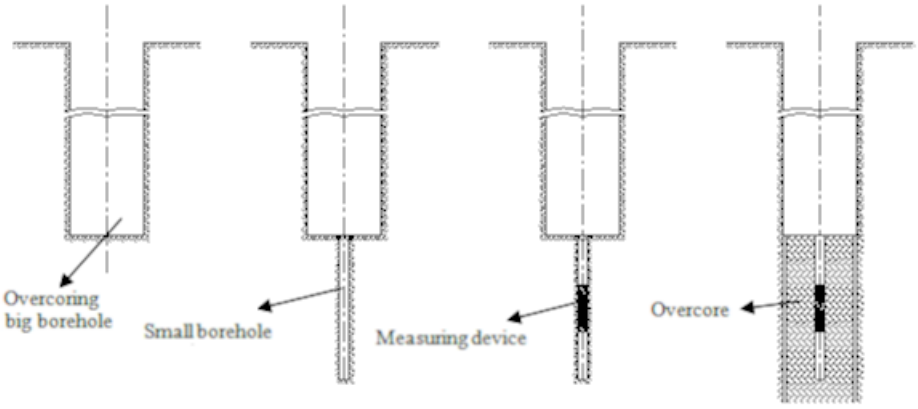

Figure 2.16 The steps of a typical overcoring operation (taken from Guo et al., 2013)

2.4 Numerical Analysis in Geomechanics

Rock engineering employs the rock mass, as a majorly discontinuous, anisotropic, inhomogeneous, and nonlinearly-elastic material (Harrison & Hudson, 2000) to create surface and underground structures. Rock mechanics takes advantage of mechanical principles to deal with the challenges of excavation on large-scale, within pre-stressed, and naturally occurring material. Various modeling approaches have been developed to analyze the mechanical effects of excavation on geomaterials as shown in Figure 2.17 (Hudson, 2001).

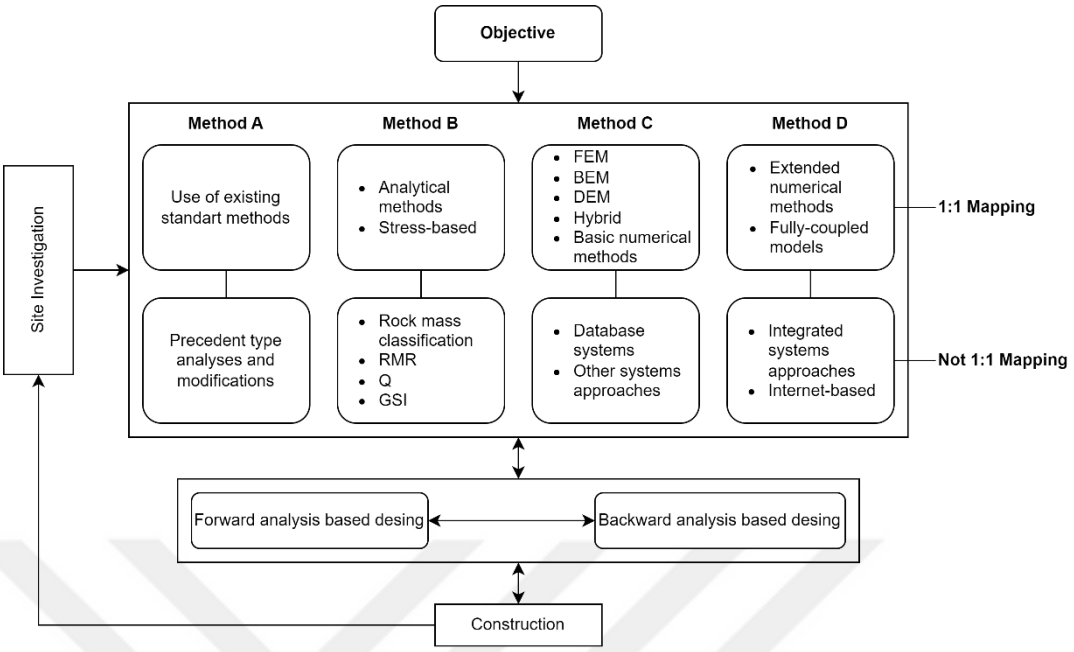

Figure 2.17 Four different approaches to rock mechanics modeling and design (after Hudson, 2001)

This section presents the numerical methods employed in rock mechanics. Computational models provide the mechanical indicators of force interactions as a result of parametrical analysis of rock excavations. In common, two different methods have been adopted for modeling rock failure, which are the continuum and the discontinuum approaches. The algorithms involve specific adjustments regarding the structural characteristics. Continuum methods consider the modeled area as a solid mass that is free of cracks and fractures. Although micro or macro-scale structural disconformities are inevitable for most of the rocks, the continuum assumption is favorable as it offers computational advantages regarding the difficulty of simulating numerous distinct elements together with their contact relationships. In continuum modeling, all elements are combined and it is not possible to separate them in any instance of the solution. The finite element method (FEM), finite difference method (FDM), and the boundary element method (BEM) are among the most commonly used numerical methods for modeling continuum (Lisjak & Grasselli, 2014).

Despite continuum being a valid assumption for most of the geomechanical problems, rock mass may involve major structural disconformities like faults and major joint sets. The discrete Element Method (DEM) was developed for the simulation of discrete bodies considering the contact relationships. DEM divides the rock mass into discrete deformable or rigid blocks and block-block interactions can be defined using slip models. For each load step, the block positions are updated using equations of motion. This way, their separation and the new contact surfaces can be determined (Cundall & Hart, 1992). The basic flowsheet of DEM involves the representation of a fractured medium as an assembly of blocks and solving the equations of motion for each block by continuously identifying and handling the contact surfaces. Deformable blocks make use of FDM or FEM for the calculation of deformations. However, rigid blocks may also be used solely to observe large deformations. Both continuum and discontinuum models have been used in underground mining, slope stability analysis, tunneling, and strata control in sedimentary rocks and especially underground coal mining to obtain more accurate simulations (D. Chen et al., 2021). Another use is for evaluation of the underground cavern stability, which are frequently used for storage purposes, especially in salt beds where there is no linear relationship between pressure and displacement (Weishen et al., 2011; Zhang et al., 2017). Since the strategic storage of energy materials such as natural gas and oil in salt deposits is of great importance, the stability of these caverns (Farahmand et al., 2015; Habibi et al., 2021), the deformation mechanism (Müller et al., 2018) and subsidence prediction (Wei et al., 2016) were studied by various researchers using numerical modeling. Recent subsidence studies have been focusing on the estimation of the deformation growth based on caving sequence (Fuenkajorn & Archeeploha, 2011).

2.4.1 Finite Element Method

FEM has been widely used and adapted as a numerical method in engineering due to its homogenous and anisotropic material handling ability. FEM consists of three

main stages. The first stage is called preprocessing, where the model is meshed, the material is defined, and boundary conditions are set. In the second stage, the solver calculates the displacement of the nodes, distortions, stresses, and nodal forces. In the final stage of postprocessing, the results of the solver step are displayed graphically. In FEM, basically three steps are needed to perform the analysis: domain discretization, local approximation, and assemblage as well as solution of the global matrix equation (Jing & Hudson, 2002). Domain discretization is the first part of the solution, which divides the body with a finite number of elements using regular shapes. These shapes could be three nodded triangles and eight nodded bricks. The nodal values of the system unknowns can be used as a trial function to approximate the unknown function, over each element by satisfying probabilistic density functions. The order of shape functions along a common edge shared by two elements must match in order to impose the displacement compatibility requirement, ensuring that there is no displacement discontinuity both along and across the edge. So, fracture analysis is a hard task to accomplish with continuum method. In FEM, imitation of strain localization results in unphysical mesh sensitivity. Since localization takes place in a region with zero thickness, this is an inevitable result (Jing, 2003). As a solution, 'joint element' is introduced where presuming that the contact stresses and relative displacements along and across the rock fractures of a theoretical zero thickness follow a linear relation with constant normal and shear stiffness, K_n and K_s (Goodman et al., 1968). Also, mesh detachment, sliding, and detachment of elements are not represented and because of the zero-thickness numerical representation is unfit. The displacement compatibility requirement can be maintained along and across the joint elements because the displacements of a joint element are of the same order of magnitude as those of its surrounding continuum elements. Then after, with the addition of two nodes in the middle, a six-node fracture element that can be curved with a small thickness is proposed (Zienkiewicz et al., 1970). However, since the element thickness is small, with large aspect ratio problems it could create discordancy. To overcome this, FEM joint element is proposed based on plasticity theory. The method minimizes unknowns

with finite thickness elements by implementing relative displacements between the two opposite surfaces of fractures (Ghaboussi et al., 1973). An elasto-plastic relation between stress and strain components is defined as a ratio of displacement over the fracture thickness. In addition to these, interface element models are developed based on the Coulomb friction law (Katona, 1983). Using the FEM approach without K_n and K_s, this model matches pairs of nodes and defines three states, which are sticking, slipping, and opening. Similarly, by using plasticity, comparable interface model approaches were developed (Gens et al., 1995; Wang & Yuan, 1997). Research on the examination of orthotropic friction for contact interface elements in the FEM is based on the theory of plasticity using the same ideas (Buczkowski & Kleiber, 1997). Further studies are performed on the combined continuum-interface method (Hammah et al., 2007; Riahi et al., 2010). Despite these initiatives, the treatment of fractures and fracture progression continues to be the most significant limiting factor in the use of the FEM for problems involving rock mechanics, particularly when a high number of fractures must be explicitly represented.

2.4.2 Discrete Element Method

The origins of DEM date back to the early 1970s (Cundall, 1971) and still have been developing as one of the most popular methods of discontinuum modeling. DEM aims to improve the simulation of pre-fractured solids, where FEM suffers to imitate the separation of discontinuities. DEM is a modelling technique that allows finite displacement and rotations of distinct elements, where complete detachment is possible. Also, identifies new contacts as simulation progress (Cundall & Hart, 1992). In other words, DEM treats the model body as a collection of deformable or rigid blocks and contacts. Stress, deformation, and location are updated regularly at each iteration during the whole computation process using the constitutive models and equations of motion. Basically, five steps are needed to perform. Sub-division and identification of model topology, the definition of block type as deformable or rigid, determination of contact relations (Lagrange multiplier, or augmented

Lagrange multiplier), selection of a constitutive model for blocks and discontinuities and assessment of blocks with equations of motion (Jing, 2003). Identification of block topology involves the assignment of in situ fracture network. Commonly, this is a stochastic process since the in-situ state cannot be fully observed because fractures develop within the rock mass and the only viable option is borehole sampling or surface mapping from the exposures. Therefore, the reliability of the fracture models relies on the quality of logging and mapping, which are highly uncertain (Sharma et al., 1999). The following step is the assignment of block types. According to block representation, for rigid blocks an explicit time-dependent scheme is used to solve the equation of motions which is based on a dynamic or static relaxation (Jing & Stephansson, 1994). Based on the adopted solution algorithm, in general, two methods are presented as being explicit and implicit methods (Jing & Stephansson, 2007). An explicit solution discretizes the interiors of the blocks at finite volumes without requiring the solution of significant matrix equations. Meanwhile, the implicit solution discretizes the block interiors using finite elements, which provides a matrix equation similar to FEM and represents the deformability of the block systems. One of the most commonly used explicit DEM codes are Universal Distinct Element Code (UDEC), 3DEC, and Particle Flow Code (PFC) (ITASCA Consulting Group Inc., 1992, 1994, 1995). Also, for implicit DEM, Discontinuous Deformation Analysis (DDA) (Shi & Goodman, 1985) is used. Although in early times DDA was used as a back analysis algorithm for deformed rock, later extended to perform complete deformation analysis by simulating dynamics, kinematics, and elastic deformability of a system of rock blocks (Shi, 1988). The explicit DEM model PFC is developed to solve non-cohesive media problems. Since soil and sands are naturally granular, rigid, and non-cohesive material this method has been widely used to simulate micromechanical interactions by using circular rigid particles of various diameters. Contacts between these particles are represented by normal and shear stiffness, and friction coefficient (Cho et al., 2007). Whereas UDEC and 3DEC as another explicit DEM scheme discretize the subject area into blocks regarding the intersection of discontinuities. To calculate

stress, strain, and displacement, each block is internally divided using a finite difference, or finite volume procedure. In 2D code (UDEC), blocks are represented by a finite number of straight-edged polygons. In 3D code (3DEC), blocks are convex polyhedral volumes with a finite number of rectilinear edges (Jing, 2003). Fractured blocks can be characterized either individually or randomly according to their field data. Individual characterization could be useful for large-scale fractures such as major faults etc.; however, in random method dip angles, dip directions, spacing, and apertures of the discontinuity sets need to be obtained from field data by using random distributions. Contact detection in the DEM is carried out by algorithms that identify the types of contacts, the largest possible gaps, and the unit normal vectors that define the tangential plane where sliding may take place. The contact bond and the parallel bond are the two main types of bonds utilized in PFC to connect blocks. Contact faces of particles are represented by a fictitious elastic spring (Kazerani & Zhao, 2010). In the parallel bond model, the force due to particle rotation is resisted by a set of elastic springs equally spaced across a region of a finite size on the contact plane and centered at the contact point (Figure 2.18).

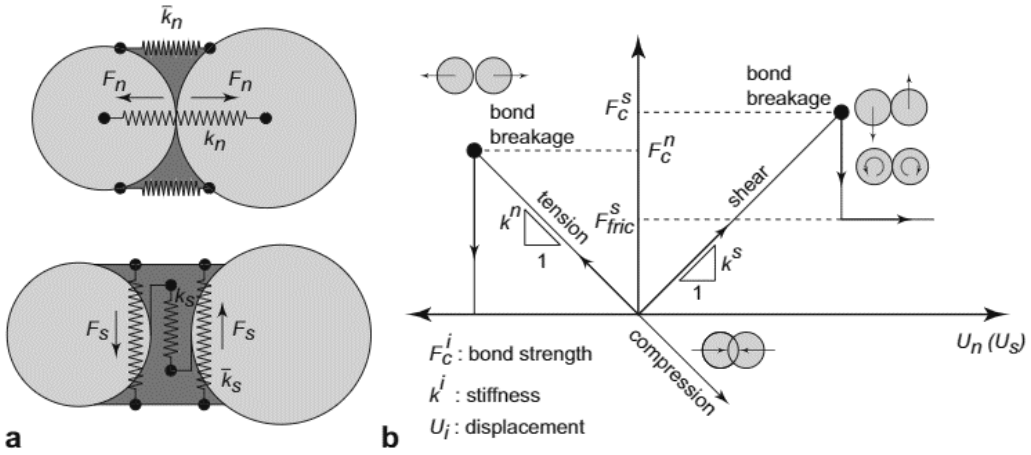

Figure 2.18 The parallel bond model in PFC (a) normal and shear stiffness (b) constitutive behavior in shear and tension (Lisjak & Grasselli, 2014)

The behavior of complex-shaped and tightly interconnected particles (typical of hard rocks) cannot be accurately modeled by simply adopting circular particles. Similar to PFC, UDEC and 3DEC use damping to solve static problems using a dynamic

relaxation technique in order to arrive at steady-state solutions. In addition to stiffness and friction angle in tangential directions with regard to the fracture surface, mechanical characteristics also include stiffness in the normal direction. The mechanical interaction between blocks is characterized by compliant contacts that use a finite stiffness and tensile strength criterion in the normal direction and a tangential stiffness and shear strength criterion (i.e., Coulomb-type friction) in the tangential direction to the discontinuity surface (Figure 2.19).

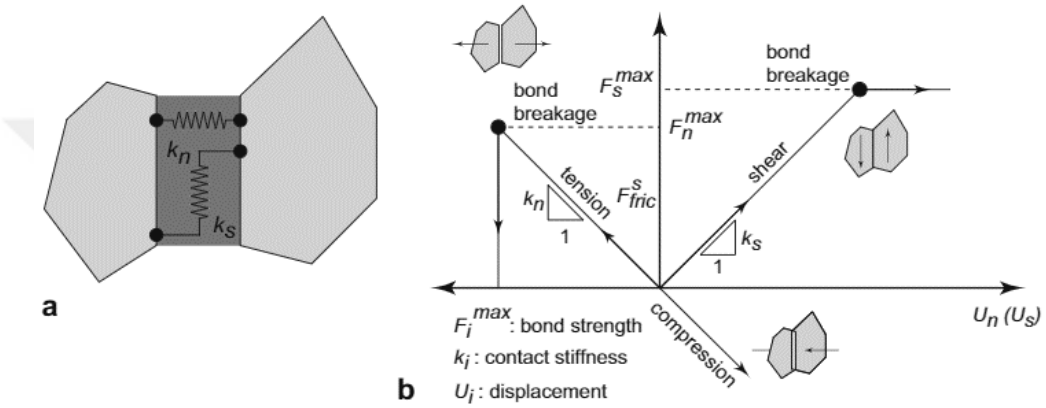

Figure 2.19 UDEC fracture propagation (a) normal and shear stiffness (b) constitutive behavior in shear and tension (Lisjak & Grasselli, 2014)

The explicit DEM does not require the setting and solution of a matrix for the equations of motion. An explicit central difference approach is used by presenting known variables directly from the element and its boundary or its closest neighbors. Two fundamental processes take place: the calculation of kinematic quantities and the calculation of the forces and stresses that make up a system. Velocities, displacements, accelerations, contact forces, and internal stresses are estimated at every time step (Hart, 1993) (Figure 2.20).

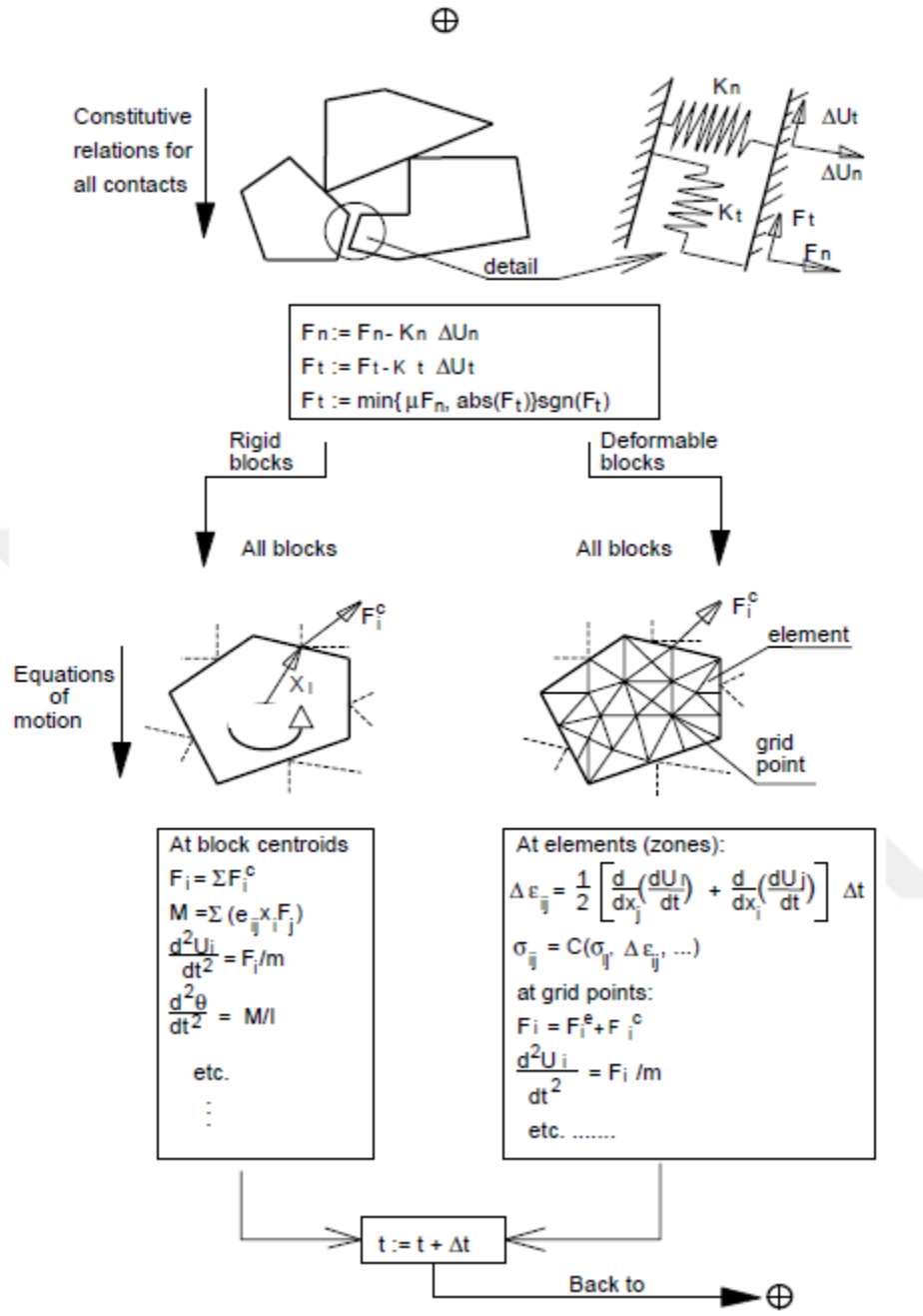

Figure 2.20 Calculation cycles in DEM (Jing, 2003)

Despite DEM's advantages, its widespread applications are constrained due to a lack of knowledge about the geometry of the rock discontinuities. In general, the shape of the fracture networks in rock masses is unknown and may only be inferred. How well the DEM results replicate real-life conditions depends on the representation of

the in-situ fracture network. The determination of discontinuity becomes a significant input parameter due to the DEM's demand for precise fracture geometry representation. Therefore, it is crucial to enhance the accuracy of fracture networks by utilizing advanced and practical technologies.

Visual inspections and geophysical methods are handy in mapping the discontinuity network in the rock mass. However, none of these techniques are capable of providing a complete sense of structural mapping. The 'Discrete Fracture Network (DFN)' is an alternative statistical method that provides a model of a fracture network and can be implemented in numerical codes (Long et al., 1982). It is possible to define a DFN model with stochastic and deterministic methods based on geometric and orientational parameters such as the direction, size, shape, and spacing of discontinuities (Lei et al., 2017). The deterministic method includes geological mapping of discontinuities by relying on observations. Discontinuities, simply fractures, can be mapped directly from rock outcrops as well as excavation faces (Einstein & Baccher, 1983; Griffith et al., 2009). As an alternative, with the developing technology, remote sensing techniques like LiDAR and photogrammetry could be used to capture fractures with more accuracy (Jacquemyn et al., 2012; Sturzenegger & Stead, 2009). LiDAR survey with certain statistical fracture shape/persistence may provide near surface mapping but again it is not competent for fractures that are located deep in the rock. The same problem continues for borehole imaging techniques which may provide shallow 3D fracture maps from a well. In addition to these, seismic reflection and refraction techniques could be useful. Although seismic data can be used to create 3D maps of large-scale geological formations, the resolution is typically too low to distinguish fine details, such as the segmentation of faults, and to locate microscopic cracks widely dispersed in subterranean rocks (Kattenhorn & Pollard, 2001). Due to the aforementioned complications and limitations of the representation of the 3D fracture systems, stochastic methods are developed. In the stochastic approach, fractures are treated as lines (in 2D) or discs/polygons (in 3D) (Figure 2.21).

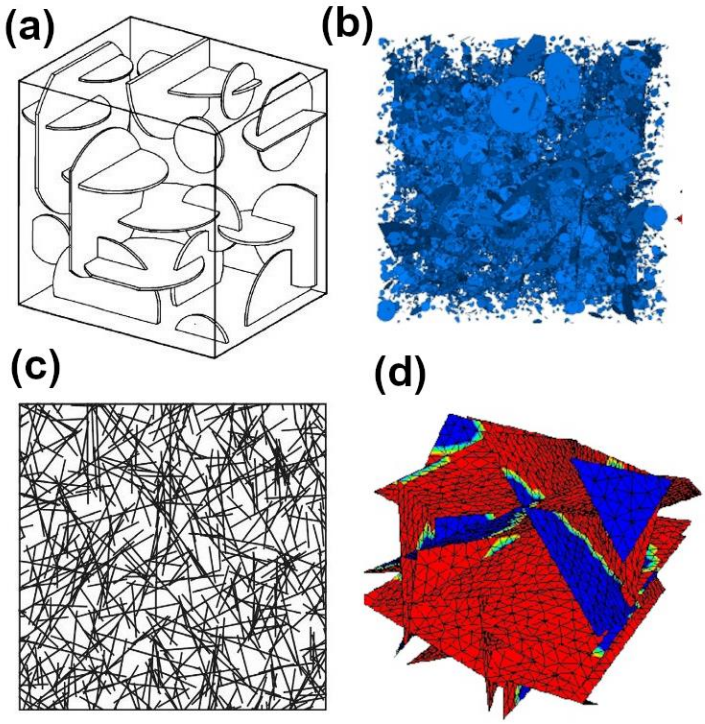

Figure 2.21 Representation of DFN in (a) & (b) 3-D discs (Long et al., 1985) (c) 2-D lines (Lei et al., 2017) (d) 3-D polygons (Itasca Consulting Group Inc., 2016)

Properties of fractures such as position, frequency, size, orientation, and aperture are independent random variables with probabilistic distributions. Orientation distributions can be uniform, normal or Fisher. The size of the fractures may be distributed by negative exponential, lognormal, gamma or power law. The frequency of the fractures are denoted by using P_{ij} system (Figure 2.22). 'i' is the dimension of the sample where 'j' is the dimension of the measurement. P_{ij} system could be described by fracture density where the number of fractures per unit volume (P_{30}), area (P_{20}), or length (P_{10}), or fracture intensity where the total fracture persistence per unit volume (P_{32}), area (P_{21}), or length (P_{10}) (Dershowitz & Herda, 1992). Depending on how much the network has been fractured, the distribution of fracture spacing may be negative exponential, lognormal, or normal. A power law with a linear or sublinear scaling relationship may be used to relate fracture apertures to fracture sizes. Fracture apertures often reflect a lognormal or power law distribution.

In general, both deterministic and stochastic approaches have their own advantages and disadvantages (Table 2.9).

Table 2.9 The advantages and disadvantages of different DFN approaches (after Lei et al., 2017)

Approach	*Inputs*	*Advantages*	*Limitations*
Deterministic	Analog mapping, LiDAR scanning, borehole imaging, aerial photographs, seismic surveys.	Geological realism, deterministic description of a fracture system.	Feasibility for deep rock, difficulty in 3D mapping, measurement scale, and resolution constraints.
Stochastic	Statistical data.	Simplicity, efficiency, 2D & 3D application, range of scale.	Oversimplification, uncertainties in parameters, multiple run need, physical process omission.

Hydrofracking applications in reservoirs consisting of sandstone and shales were numerically implemented using DFN models in order to increase the recovery and efficiency in shale gas production (Sipahi & Develi, 2021; Zhou et al., 2016). In tunneling and underground mining, the stability of the upper formations is of great importance. In this context, the DFN models were used to study the stability of excavations (Farahmand et al., 2015; Wang & Cai, 2020). Comparing the deterministic and stochastic methods on reservoir rocks revealed the advantages and disadvantages of the methods (Tavakkoli et al., 2009). Studies are conducted by using DFN and various interdisciplinary methods in reservoir rocks to increase the recovery from a reservoir (Turkmen & Gozel, 2014).

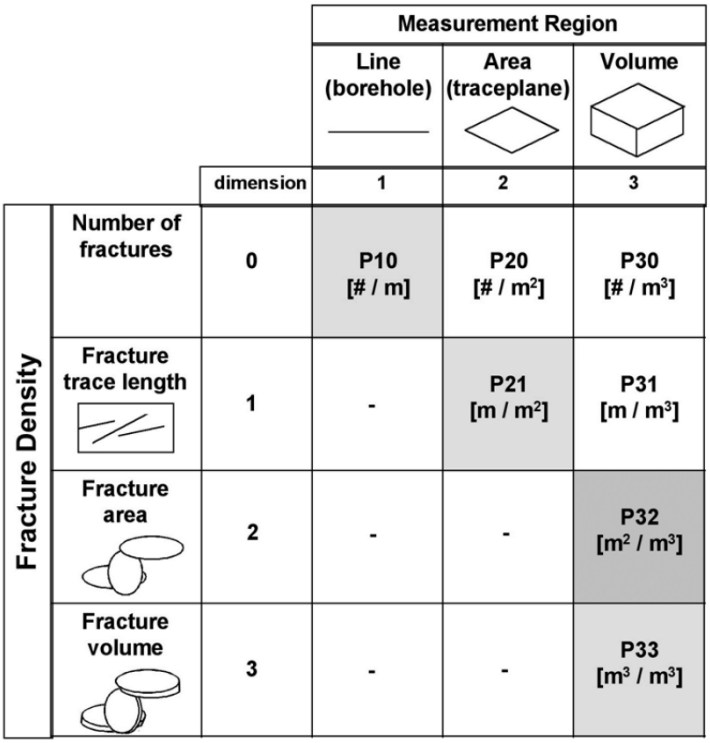

Figure 2.22 Measures of fracture density (taken from Chou et al., 2016)

2.4.3 Hybrid Methods

As an alternative to using a single technique like FEM or DEM, hybrid methods benefit from the advantages of continuum and discontinuum approaches by employing both techniques. For the most part, hybrid approaches are employed to address fractured rock mass stress/deformation and fluid flow. Commonly used hybrid methods in geomechanics are hybrid FEM/BEM, DEM/BEM, and FDEM models (Jing & Hudson, 2002). The hybrid FEM/BEM technique uses the BEM region as a super element with an artificial symmetric stiffness matrix as a method for general stress analysis (Zienkiewicz & Kelly, 1977). Similar to FEM, the hybrid FEM/BEM approach is effective in terms of processing power. Additionally, the advantages of FEM can be used to deal with the rock mass' nonlinear behavior. In the discontinuum-based hybrid approach side, the hybrid DEM/BEM model, which is based on UDEC and 3DEC (Lemos, 1987; Lorig & Brady, 1982), has contact with

the interfaces of smaller blocks of the DEM region and is surrounded by BEM region that is treated as a superblock. Besides FEM/BEM and DEM/BEM, the hybrid finite-discrete element approach (FDEM) combines discrete element solutions for transient dynamics, contact detection, and interaction with finite element analysis of stress/deformation evolution (Pan & Reed, 1991). The FEM algorithm calculates the internal stress field of each discrete matrix block in such a discontinuum modeling scheme, and the DEM algorithms trace the translation, rotation, and interaction of multiple rock blocks (Munjiza, 2004). Briefly, the FDEM approach blends FEM techniques with DEM by including fracture mechanics concepts into the formulation, the FDEM technique also offers a natural route to modeling the transitional behavior of brittle/quasi-brittle materials from continuum to discontinuum.

2.4.4 Meshless Methods

Since mesh production relies totally on judgment and experience rather than theoretical direction, it takes significantly longer than the actual calculations. It frequently takes several trial-and-error steps to resolve the problems correctly. The meshless methods greatly simplify the operation of creating a mesh in FEM taking advantage of no need for permanent elements and elimination of the element locking effect. However, it requires higher computational sources to generate numerically the trial functions over the node clusters (Belytschko et al., 1996). It has not yet outperformed FEM approaches in terms of sheer computational performance (Jing, 2003). Briefly, three fundamental operations are carried out; interpolation using trial (shape) functions, integration to produce governing algebraic equations, and solution of the final system equations. Some of the early meshless applications (Belytschko et al., 1994; Chen et al., 2017; Duarte & Tinsley Odent, 1996; Liu et al., 1995; Melenk & Babuska, 1996; Nayroles et al., 1992) could not be accepted as a true meshless method due to necessity of background mesh integration. However, the methods Local Petrov-Galerkin and Local Boundary Integral Equations are not using background meshes for interpolation or integration (Atluri et al., 1999; Atluri & Zhu,

1998). In FEM, the fundamental boundary functions are efficiently satisfied thanks to the Kronecker delta function feature of the shape functions. The produced interpolation functions in many meshless approaches do not have the Kronecker delta property at nodes. Due to this, the problem with many meshless methods is the difficulty of enforcing crucial boundary conditions like Smoothed Particle Hydrodynamics (SPH). In the method SPH (Gingold & Monaghan, 1977) setting boundary conditions is a very challenging task.

2.5 Common Strata Control Problem in Sedimentary Deposits

Strata control (ground control) is the study of the mechanical state and transition of the geological layers (Peng, 1978). The instability risk within the critical strata can be reduced by reinforcing or supporting the rock mass (Hadjigeorgiou & Potvin, 2011). The reinforcement stands for the application of the measures into the rock mass like grouted or non-grouted rock bolts, mechanical or resin anchored bolts, split sets, and swellex etc. (Bawden, 2011); however, supports are applied externally (i.e., shotcrete and steel mesh). General considerations and procedures are similar for both hard-rock and weak-rock mining operations. However, in weak-rock, time dependency is an extra concern that influences the support requirements (Stace, 2011). Common ground control problems are pillar failure, roadway instability, roof instability, and surface subsidence. Determining the stress and geological conditions is important since most of the failures occur due to incorrect pillar design or lack of geological knowledge (Van Besien, 1973). The following sections present the commonly seen strata control problems in detail.

2.5.1 Roof Instability

Underground mine excavations disturb the force and moment equilibrium of the rock mass in its virgin state. The unsupported roof tends to yield through the opening and results in roof failure when the tensile strength is surpassed by the driving stresses.

A pillar, which is a natural support to reduce the roof deformations by leaving an unexcavated portion of the rock mass, may be used to ensure the roof stability. In addition, opening dimensions can be adjusted to contribute more to the opening stability. Roof stability is a vital aspect of underground mining in terms of the safety, economy, and sustainability of the operation. Most of the research focuses on roof stability in coal mining operated by room-and-pillar and longwall methods (Hardy & Agapito, 1977; Mark, 1999; Salamon & Munro, 1967). However, the literature has gaps for hard rocks and other weak rocks such as trona and salts (Bullock, 2011). For pillar design, various studies have been presented covering the strength and load calculations (Bieniawski, 1987; Bieniawski, 1992; Coates, 1981; Farmer, 1992; Peng, 1978; Koehler & Tadolini, 1995). The tributary area is one of the examples of these works (Figure 2.23). In the tributary area method, average pillar stress for a square pillar is calculated by following equation 8 where W_p is pillar width and W_o is opening width.

$$\sigma_{pa} = \sigma_z \left(\frac{W_p + W_o}{W_p} \right)^2 \tag{8}$$

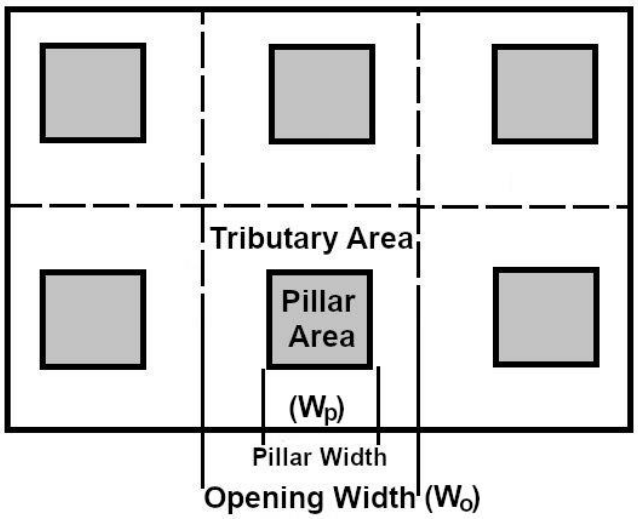

Figure 2.23 Tributary area representation

Large underground openings such as the panels in longwall mining induce three distinct zones of deformation as a result of mining (Figure 2.24). If the upper strata are stiff and thick, the vertical or near-vertical fractures will require greater loads to form and the displacements will be slow (Peng & Chiang, 1984). This can be expected to lead to sudden and severe collapse due to overstressing. Considering various stratigraphy may be present in sedimentary deposits, the seam thickness and stiffness should be regarded to control the overburden movements. Besides, the weak bonding strength between the seams may not prevent the overburden rock to bend down into the opening and this may lead to the accumulation of tensile stresses within the overlaying strata (Stefanko, 1983).

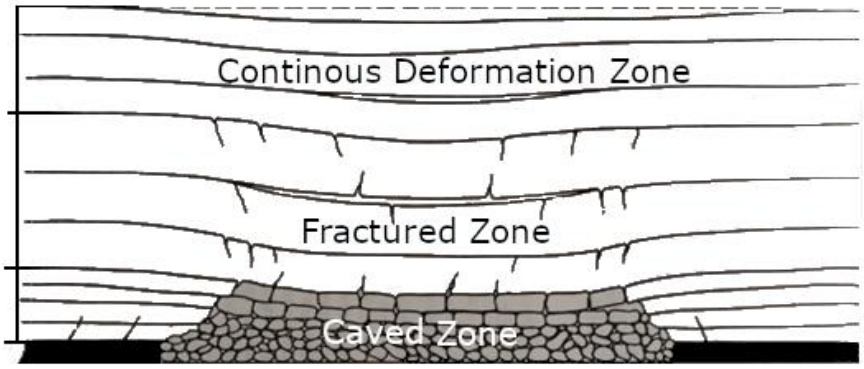

Figure 2.24 The caved, fractured, and continuous deformation zones above an underground opening (modified after Peng & Chiang, 1984)

Because of these drawbacks, roof control has been subject to various studies (Ünal, 1983) as well as pillar design (Zipf, 2001). Characterization and understanding the roof stability and pillar behavior is still an ongoing research interest to improve the operational safety. To achieve that, longwall operations with physical modeling (Ghabraie et al., 2015; Moradi et al., 2015) also numerical modeling (Chen et al., 2021; Singh & Singh, 2010) are studied. The effect of water and humidity on caving behavior (Liu & Liu, 2021), pillar design (Pechmann et al., 1995; Zipf & Swanson, 1999), and salt mine cavern integrity (Weishen et al., 2011) are also studied.

2.5.2 Surface Subsidence

Surface subsidence is an unavoidable result of underground mining (Figure 2.25). Surface subsidence covers both vertical and horizontal displacements. Commonly, it is observed in continuous or discontinuous forms affecting a limited area with cracks or cavities for the latter one and extensive areas for the former one (Harrison, 2011). There are various factors affecting subsidence but the most significant ones are the extraction thickness and the mining depth, the production method, the extraction rate, the in-situ stress, the discontinuities, and the hydrogeology (Peng, 1978). Some methods to predict surface subsidence are the graphical method, profile function method, influence function method (Whittaker & Reddish, 1989), and numerical methods by FEM (Choi & Dahl, 1981) and DEM (Zangerl et al., 2008). Generally, the subsidence individually has no significant effect on the surface structures (Peng & Chiang, 1984); however, the unexpected subsidence development may be destructive. To understand that, in coal mining subsidence relationship with the dip angle of the orebody (Sun et al., 2021), multi-seam mining method (Qin et al., 2021) along with physical models (Ghabraie et al., 2017) are studied. Also, brittle and weak-rocks are studied in terms of the effect of cavern geometry with stress concentration (Cyran et al., 2019) and the effect of multiple beds (Wei et al., 2016).

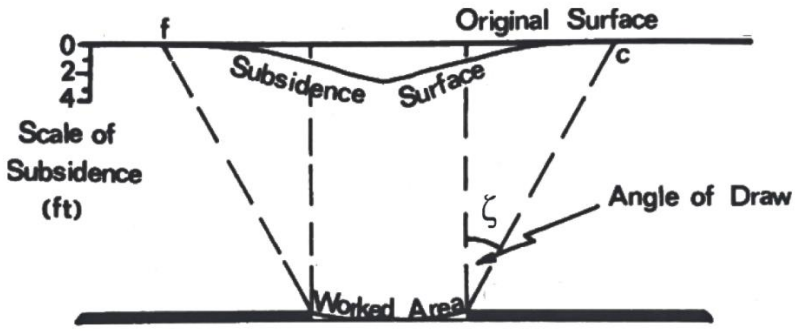

Figure 2.25 Section view of a tabular deposit and surface subsidence (Peng, 1978)

2.6 Destressing

Strata control has been a major concern for the mines, especially operating at deep deposits and/or hard-rock mass that is prone to accumulate stress after excavation. The stress concentration may result in rock burst from free surfaces, where the rock mass fails violently. Also, high-stress bearing characteristic of stiff roof strata that does not cave concordantly with excavation could result in sudden collapse that threats workers, equipment, and the sustainability of a mining operation. Destressing methods have been developed as a measure for rock burst and strata control. Some of them include destress blasting, water infusion, hydrofracking, and drilling destress holes (Gu et al., 2019)

Destress blasting arises from the idea of inducing fractures on the stiff strata to reduce the high-stress bearing capacity (Roux et al., 1957). It is widely accepted and implemented in deep hard-rock metal mines in South Africa (Konicek et al., 2011) and longwall mining of hard coals (Konicek & Schreiber, 2018). In hard-rock longwall mines, the competent roof strata above the orebody cause stress accumulation on the coal face which leads to the coal burst in the face. To eliminate that destress blasting is performed (Wojtecki et al., 2020). Apart from the rock burst risks, sudden collapse of the stiff roof strata by releasing high energy is a catastrophic event. Some studies claim that destress blasting only activates and propagates pre-existing fracture networks instead of creating new ones (Toper et al., 1997), to provide caving of the overlaying strata concordantly with excavation. In order to avoid unwanted consequences, several studies are performed using numerical methods (Miao et al., 2022; Momoh et al., 1996). Also, by implementing DFN to the numerical models (Ram Saharan, 2010) and proposing new methodologies (He et al., 2017) researchers tried to simulate and facilitate stiff strata caving. In addition to longwall mining, in many hard-rock mining operations destress blasting has been employed as a preconditioning technique (Tang & Mitri, 2001) in large scales (Vennes et al., 2020). Apart from the hard-coal and hard-rock, in brittle salt deposits, the sudden collapse of the overlaying strata poses vital threats. Examples of these

kinds of failures in the United States, Netherlands (Figure 2.26.b) Germany, France (Figure 2.26.a, Figure 2.26.c), and other countries show us that in both room-and-pillar and in-situ solution mines, there is a clear association between the sudden collapse and strong overburden strata (Whyatt & Varley, 2008).

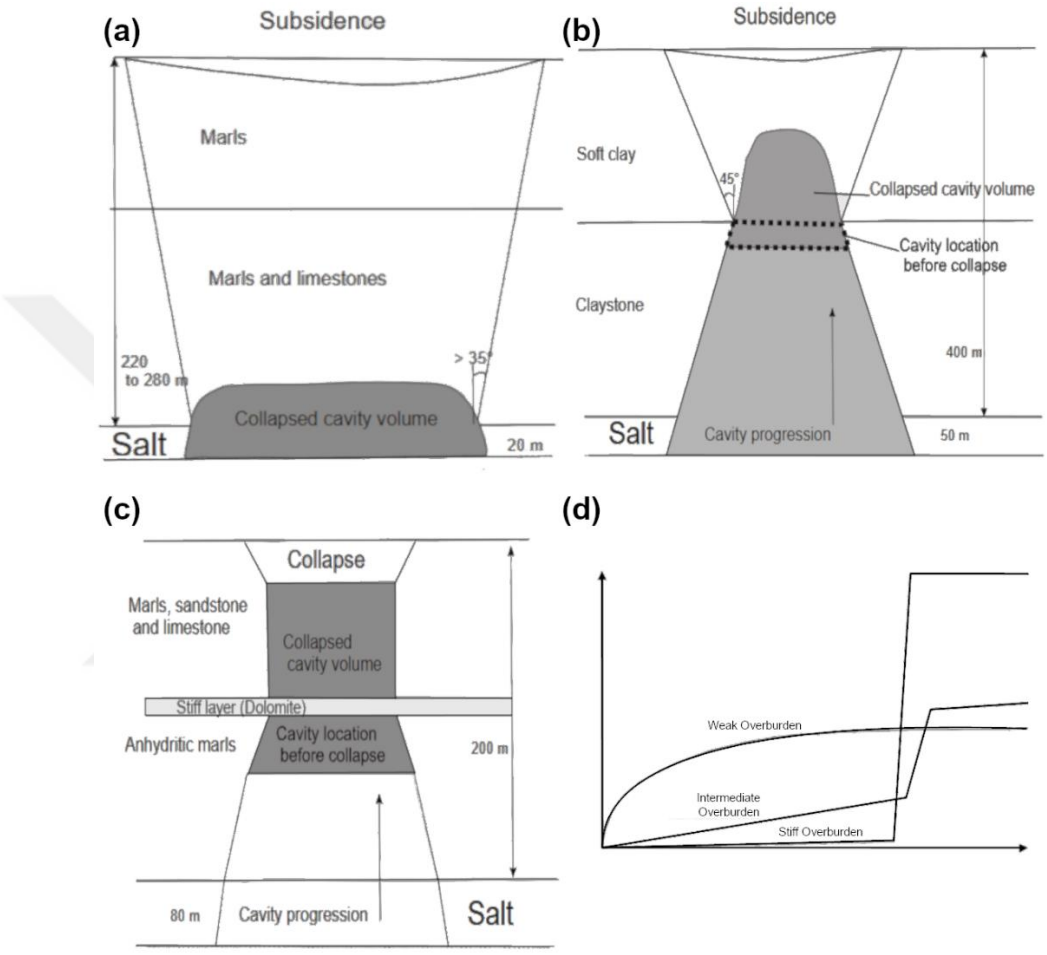

Figure 2.26 Examples of caving and collapse in (a) Sarralbe – Loraine (France) with a weak overburden (b) Twenthe – East Netherlands with an intermediate overburden (c) Nancy – Lorraine (France) with a stiff overburden (taken from Daupley et al., 2005)

Effective parameters on the sudden collapse and rock burst in crystalline rock caverns (Dowding & Andersson, 1986) and the relationship with stiff layers and salt pillars (Ma et al., 2022) also support this relation. Although the stiff layers aid to create large caverns in a solution mine, it also delays the caving and causes sudden collapse that affects production and neighboring units (Daupley et al., 2005).

CHAPTER 3

DATA COLLECTION FOR THE NUMERICAL STUDY

Geomechanical properties determine the response of rock mass to various loading conditions induced by excavation or other reasons. While the in-situ testing may characterize the mechanical condition more accurately, the operational and economic disadvantages make them unfavorable. Alternatively, empirical methods based on field studies and laboratory testing can be used. It is a well-known fact that geomechanical simulations rely majorly on mechanical input parameters. This study makes use of the field and laboratory data from a real trona deposit but examines the solution mining on a hypothetical case where the trona seams are thick. In this section, the determination of rock mass parameters for the real trona deposit and the overlaying strata are presented.

3.1 The Field Studies

Rock mass characterization studies were performed on drill core samples obtained from four different wells in the Beypazarı trona field. Nickel-plated core barrels were used to minimize the mechanical impacts on core samples. In trona layers, soda ash was mixed with drilling mud to prevent trona dissolution. The sample diameters were 83 mm and 63 mm, which were obtained with PQ and HQ size drill bits, respectively. After the cores were extracted, they were kept in a storage after wrapping with a protective film to enclose the moisture content of the samples. The samples were later used for the characterization studies. Although the rock mass parameters were obtained from the Beypazarı field, the simulated case in the research represents a hypothetical case, which is different from Beypazari in terms of operation practice and geological settings. The thickness of the strata (the interburden, trona, and

intercalations), and the depth of the layers were designed to study the effects of destressing on the thick and stiff layers.

3.1.1 Identification of the Structural Domains

In the Beypazarı Trona field, four geological formations were addressed with alternating thicknesses above the trona deposit (Figure 3.1). Regarding the various structural and mechanical characteristics, the rock mass was separated into eight domains and each of them were designated with a prefix ‘T’ starting from surface T1 to the deepest part T8. The specimens were collected from each of the structural domains for laboratory testing.

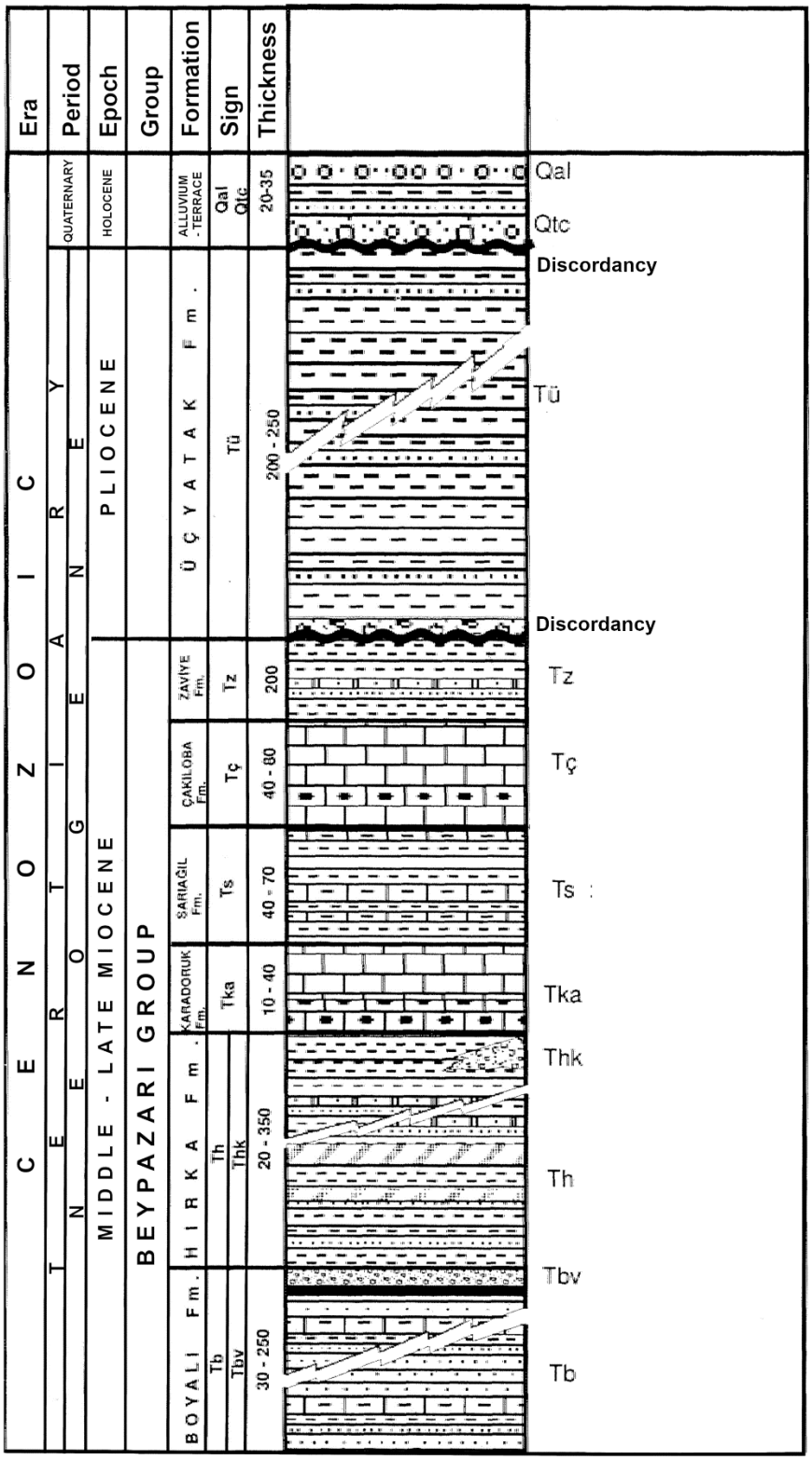

Figure 3.1 Stratigraphy of Beypazarı Trona Field

3.1.2 Rock Mass Quality Classification

The geotechnical logging was performed shortly after the samples were extracted from the drill hole. The assessments were performed according to Q (Barton et al., 1974) and RMR_{89} (Bieniawski, 1989) systems. As explained in Chapter-2.2 in detail, RMR_{89} classifies rock mass into five classes as very good rock, good rock, moderately good rock, weak rock, and very weak rock depending on RQD (Deere et al., 1967), discontinuity condition, discontinuity spacing and direction, and groundwater conditions. Similarly, the Q-system classifies the rock mass as extremely weak rock, very weak rock, weak rock, moderate rock, and good rock using discontinuity number, spacing, roughness, alteration, and groundwater conditions as parameters. According to RQD, 72% of the samples were classified as very weak where 23% are weak, 4% are moderate, and 2% are classified as good rock (Figure 3.2.a). In addition to these, in RMR_{89} geomechanical classification system 73% of the samples collected are classified as weak rock while the remaining 27% of them are moderately good rock (Figure 3.2.b). By Q-system, 26% of the samples were classified as extremely weak rock, 65% as very weak rock, and 9% as weak rock (Figure 3.2.c).

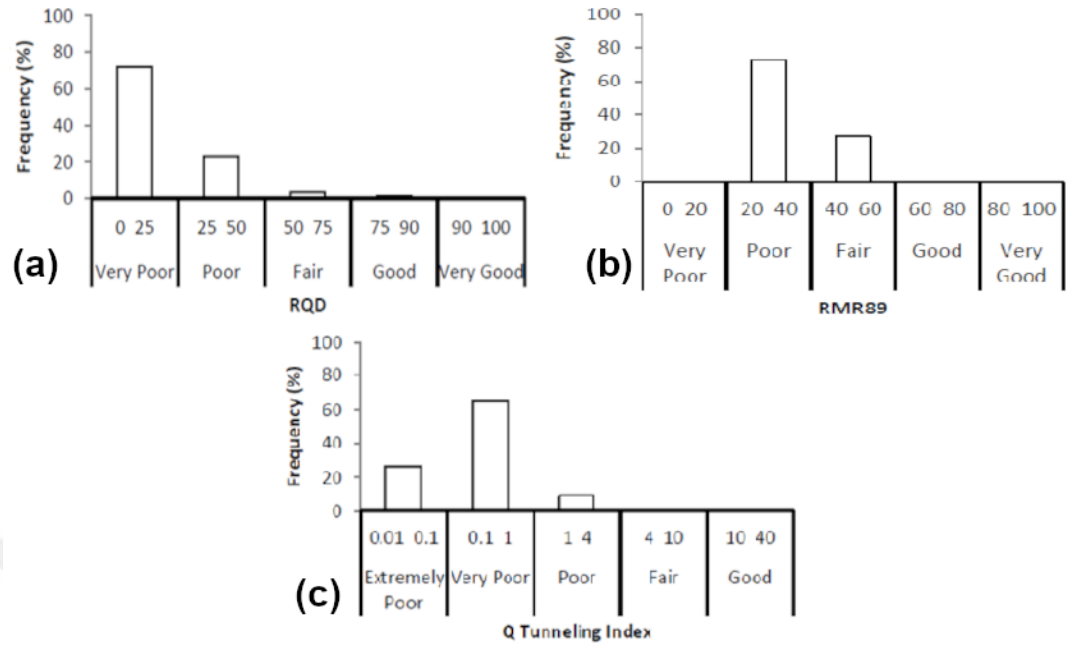

Figure 3.2 (a) RQD (b) RMR_{89} (c) Q-index distribution of the samples

3.2 Laboratory Testing

The intact core samples obtained from the field studies were transported to the METU Rock Mechanics Laboratory. The specimen were prepared according to the suggested testing methods by ISRM. As explained in Chapter 2.3, the uniaxial compressive strength tests, the static deformability tests, the triaxial compression test (confinements adjusted regarding the strata depth), the point load index tests, the indirect tensile strength test (Brazilian), and the direct shear tests were performed. According to the test results, the rock material properties are given in Table 3.1.

Table 3.1 Rock material properties for a representative trona field

Strata	*Density (gr/cm^3)*	*Unit Weight (kN/m^3)*	*Uniaxial Compressive Strength (MPa)*	*Modulus of Elasticity (MPa)*	*Poisson 's Ratio*	*Tensile Strength (MPa)*	*Cohesion (MPa)*	*Internal Friction Angle (°)*
T1	2.21	21.73	13.90	10996	0.23	1.1	1.63	27
T2	2.15	21.12	22.07	3520	0.34	0.52	3.65	38
T3	2.34	23.08	46.55	34409	0.15	2.59	5.10	53
T4	2.26	22.18	44.63	21670	0.16	1.45	8.27	28
T5	2.16	21.21	20.82	9926	0.23	2.50	7.79	28
T6	2.13	20.88	18.22	14240	0.24	3.08	5.27	39
T7	2.14	21.03	24.80	8816	0.22	2.54	5.76	34
T8	2.17	21.28	26.86	6882	0.25	3.92	-	-

The bulk modulus (K) and shear modulus (G) were calculated using the equations 9 and 10 and the results were tabulated in Table 3.2.

$$K = \frac{E}{3(1-2\upsilon)} \tag{9}$$

$$G = \frac{E}{2(1+\upsilon)} \tag{10}$$

3.3 Determination of the Rock Mass Parameters

The field studies and laboratory tests were used to calculate the rock mass parameters. The calculations were performed using Hoek-Brown (Hoek et al., 2002) failure criteria in Rocscience RocData software. Internal friction angle, cohesion, and tensile strength parameters were adjusted by decreasing 35% to conform to the post-yield of material behavior. The significant difference of T3 and T4 mechanical properties compared to the other strata points out that they are the stiff layers and stress accumulation potential is high. Compared to T4, with greater mechanical properties and thickness, T3 poses a greater risk in terms of sudden failure. Therefore, not only the method but also the exact layer(s) to apply destressing must be determined for operational efficiency. The results were presented in Table 3.2.

Also, GSI value distribution graph is given in Figure A.1 in Appendix A. It must be noted that the SI unit system was used where the length is in meters (m), density is in kg/m^3, force is in Newton (N), stress is in Pascal (Pa), and gravity is in m/sec^2.

Table 3.2 Rock mass geomechanical parameters

		T1	***T2***	***T3***	***T4***	***T5***	***T6***	***T7***	***T8***
GSI		24	26	31	30	26	27	26	21
Unit Weight (kN/m^3)		21.7	21.1	23.1	22.2	21.2	20.9	21.0	21.3
Modulus of Elasticity (GPa)		11	4	34	21	10	14	9	7
Poisson's Ratio		0.23	0.34	0.15	0.16	0.23	0.24	0.22	0.23
Bulk Modulus (GPa)		376	135	765	468	223	344	192	204
Shear Modulus (GPa)		254	48	689	411	149	222	133	134
Uniaxial Compressive Strength (MPa)		0.15	0.12	0.39	0.34	0.11	0.11	0.13	0.23
Tensile Strength (kPa)		1.04	0.14	0.25	1.94	1.56	0.29	0.47	0.72
Cohesion (MPa)	*Peak*	0.10	0.19	0.57	0.31	0.15	0.32	0.37	0.50
	Resi-dual	0.06	0.12	3.70	2.00	0.10	0.21	0.24	0.33
Internal Friction Angle (°)	*Peak*	29	39	47	26	13	22	20	26
	Resi-dual	19	26	31	17	8	14	13	16

The contact mechanical properties used in modeling were given in Table 3.3.

Table 3.3 Joint properties of discontinuities and DFN

Joint Properties	*Normal Stiffness (GN/m)*	*Shear Stiffness (GN/m)*	*Cohesion (kPa)*	*Angle of friction (^{o})*
Bedding planes & discontinuities	100	10	300	28
Destressed zone	0.1	0.01	-	-

CHAPTER 4

NUMERICAL ANALYSIS OF SOLUTION MINING IN A THICK DEPOSIT

The large underground spaces produced by solution mining induce significant deformations on the overlaying strata and around the opening. Despite the unsupported roof yields to fill in the openings, the induced stresses tend to flow around the produced region where geological units are stiff. The risk of sudden and unexpected instability due to overstressing of strata and pillars is a critical factor that cannot be traded off with the economic advantages of solution mining. Therefore, stress management is vital in solution mining. Commonly, the induced stresses can be analyzed by physical models, trial production, and geomechanical simulations. Although the laboratory scale physical models provide an overall understanding of stress flow, it is challenging to determine a rock-like material to represent the strata. Also, simplification of the structural and topological characteristics may dramatically affect the mechanical response of the model. On the other hand, test production is a costly alternative as it requires field-scale operation and in-situ monitoring of the mechanical parameters. Under these circumstances, numerical modeling is the best method to investigate various production sequences with parametric analyses. Once the rock mass behavior under various loading conditions is specified using laboratory or in-situ rock mechanics tests, computational simulations can be used to examine the response of the rock mass in any of the production stages. However, advanced mechanical knowledge is required for implementing and interpreting the geomechanical models. Considering these facts, this research was designed to rely on numerical modeling to investigate the solution mining in thick ore deposits. The geomechanical parameters were obtained from a real case to investigate a hypothetical solution mine with a thick deposit. This section presents the numerical models that involve a single production cavern and stiff layers above the trona deposit. The model geometry and boundary conditions were

explained. The ultimate goal was to simulate the stress concentration on the stiff layers due to solution mining. The strata destressing technique was simulated and the numerical modeling technique was validated to check its suitability for simulation of the stress relaxation. Later, alternative destressing schemes were numerically investigated by using ITASCA 3DEC software, and the most viable option was recommended.

4.1 The Model Geometry

The trona deposit and the surrounding strata are presented with rectangular prisms in the model body. The dimensions are 370 m in the x-direction and 800 m in the y-direction where the origin was assumed to be at the bottom-left corner of the body. The model height is 400 m. Regarding the geological and structural properties, the rock mass was divided into eight dominant layers with various thicknesses and horizontal strata contacts. A layer name was assigned from top to bottom starting with a prefix "T" and a number from 1 to 8. The thickness of each layer is also given in Figure 4.1. For T1, T2, and T8 layers mesh size of 25 m was assigned. Also, for better resolution in the layers that mechanical activity is important (T3, T4, T5, T6, and T7) the mesh size of 10 m was used. With the given mesh sizes, a total of 4368 blocks were created in the model. The velocity boundary conditions were set on each face to completely fix the motion except the top surface, which indicates the topographical surface. The gravity loading was implemented with a hydrostatical stress condition, that stands for around 8 MPa in-situ stress within the trona deposit.

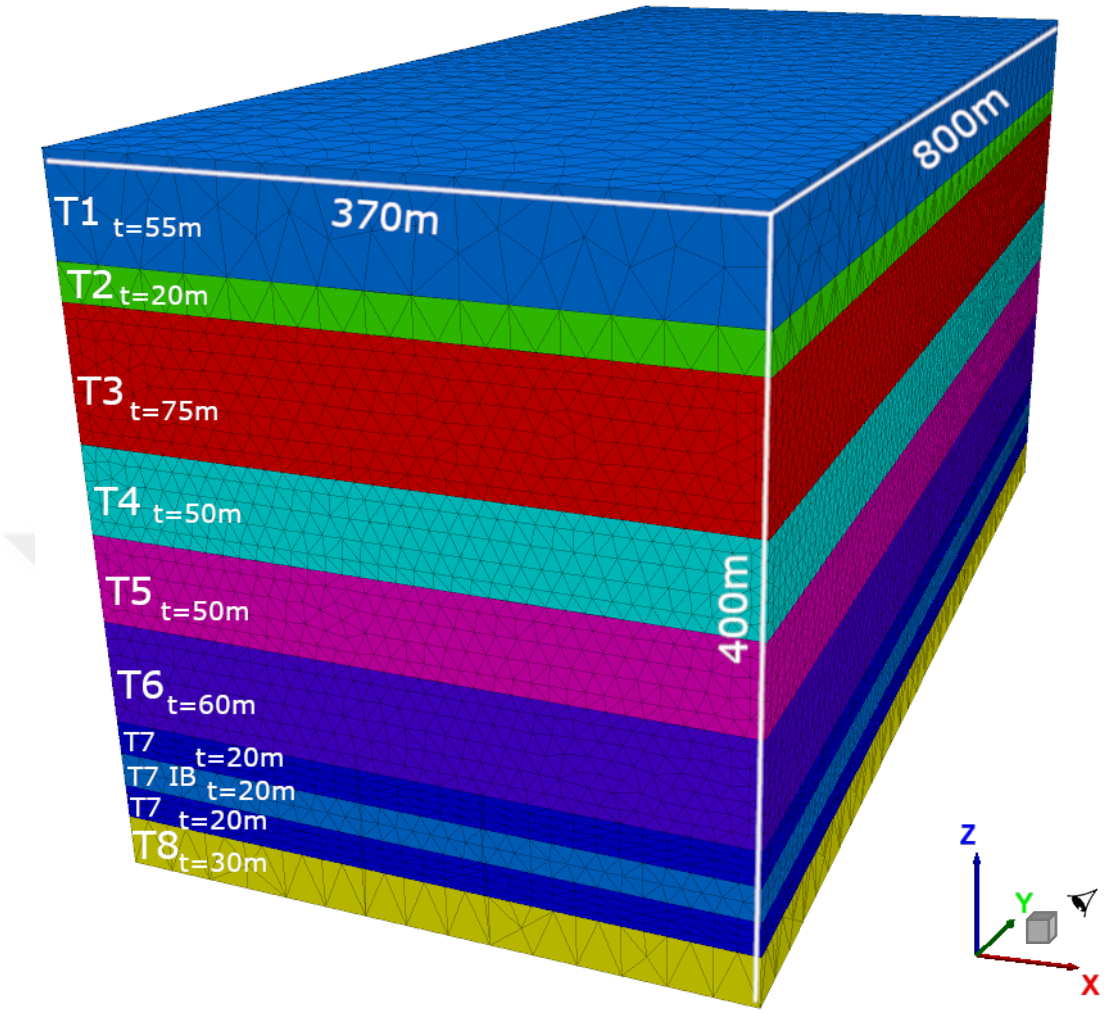

Figure 4.1 The isometric view of the model body and the strata dimensions

The geomechanical properties obtained from the interpretation of field studies and laboratory works (Chapter 3) were assigned to each layer. Also, the contact mechanical properties were set regarding the laboratory direct shear tests. The elastoplastic material behavior was implemented in terms of the 'linear-elastic model' and the 'Mohr-Coulomb Strain-Softening' model. A softening model was used on purpose as the plastic properties of geomaterials degrade when loading goes on after the material yields. On the other hand, the perfectly plastic Mohr-Coulomb model assumes no damage on the material properties by fixing the plastic properties. The strain-softening model reduces the shear resistance with the propagation of shear strains and this would allow to realistically simulate the post yield deformations.

As mentioned before, there are various operational practices for solution mining. In multi-seam bedded trona deposits, there may be intercalations within the deposit. Thus, the production sequence is a matter of concern. The common approach is to start solving the deposit from the floor and going on to the roof. As the interburden collapses the solution rises to the uppermost layer. This study covers two thick trona deposits separated by a thick interburden but the upper and lower deposits do not involve any intercalations. In the model, T7 layer presents the trona layer with a thickness of 60 m. The trona deposit was modeled to involve an upper and lower seam divided by an interburden. The seams and the interburden have equal thickness, which is 20 m. The elevation of the lower trona seam is between 30 m to 50 m and the upper trona seam is between 70 m to 90 m. Regarding the commonly observed structural features on trona seams, the upper and lower trona seams were discretized with vertical planes. In this manner, the whole trona deposit was divided into 30 pieces in y-dimension and 15 in x-dimension. A total of 450 blocks with approximately 26 m in y-dimension and 24 m in x-dimension are then joined together to act as a single layer. The interburden between the trona seams is kept as a single block and assigned with the material properties of the trona. A rectangular cavern geometry was modeled 70 m in width and 200 m in length. The cavern was located at the center of the horizontal plane (Figure 4.2). A complete production from a single cavern was simulated in phases. Each seam was divided into four sub-layers of 5 m thickness and they were removed individually from bottom to top. The lower and upper trona seams were completely exploited in a total of eight stages.

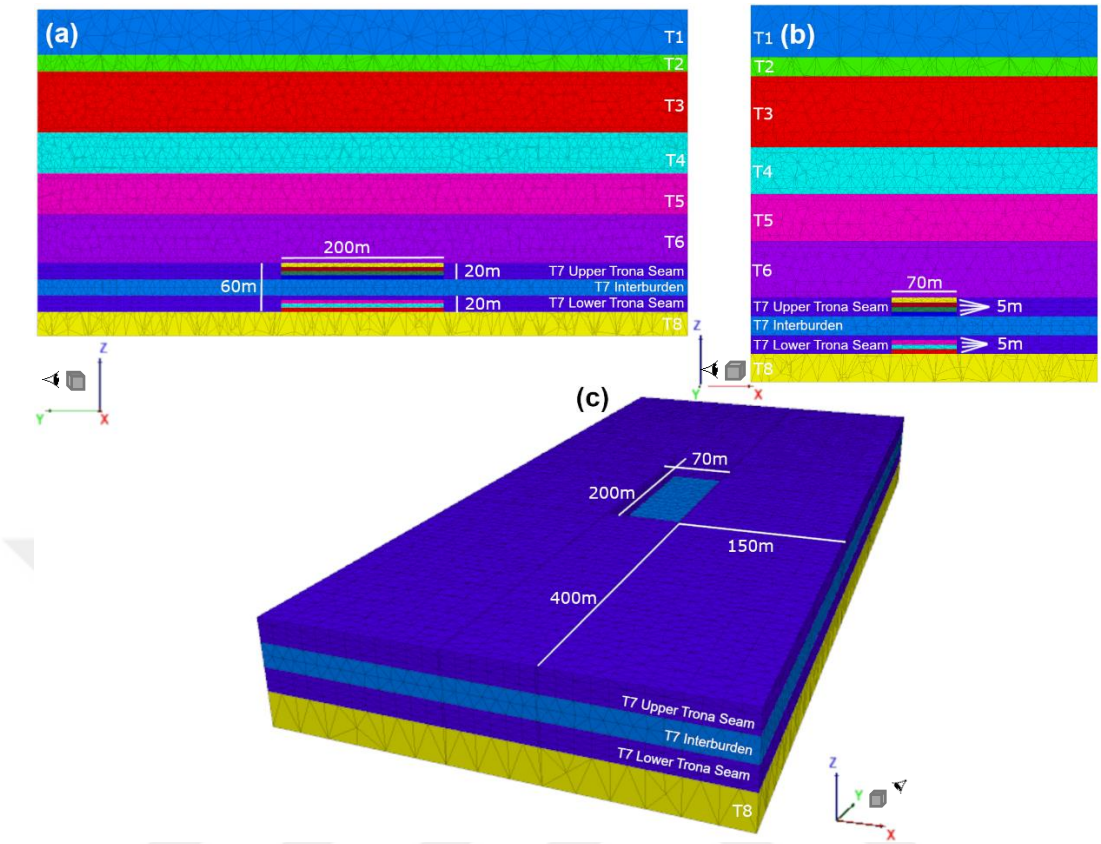

Figure 4.2 (a) The side view, (b) the front view and (c) the isometric view of the model

The major principal stress (σ_1) the minor principal stress (σ_3), and the vertical displacement on the determined history points within the overlying strata were traced for investigating the effect of destressing in a solution mine with stiff strata above the deposit. In each solution step of the iterative simulation, the mentioned parameters were stored for detailed model interpretations. The points were located right above the cavern, in each layer and along the centerline with 20 m spacing in between. The history points were assigned on the nearest grid element. For each layer, from T1 to T6, nine history points for σ_1, σ_3, and the vertical displacement were set. In total 27 history points were present in each of the six layers, which allows to check the stress and displacement in detail by plotting history graphs. In addition, three history points were placed on the interburden along the centerline with a spacing of 50 m to trace the stress. Finally, to observe the propagation of the

abutment pressure in each simulation step, a set of three history points were placed on both sides of the cavern with 50 m spacing on the cavern wall and 20 m away from the cavern walls (Figure 4.3).

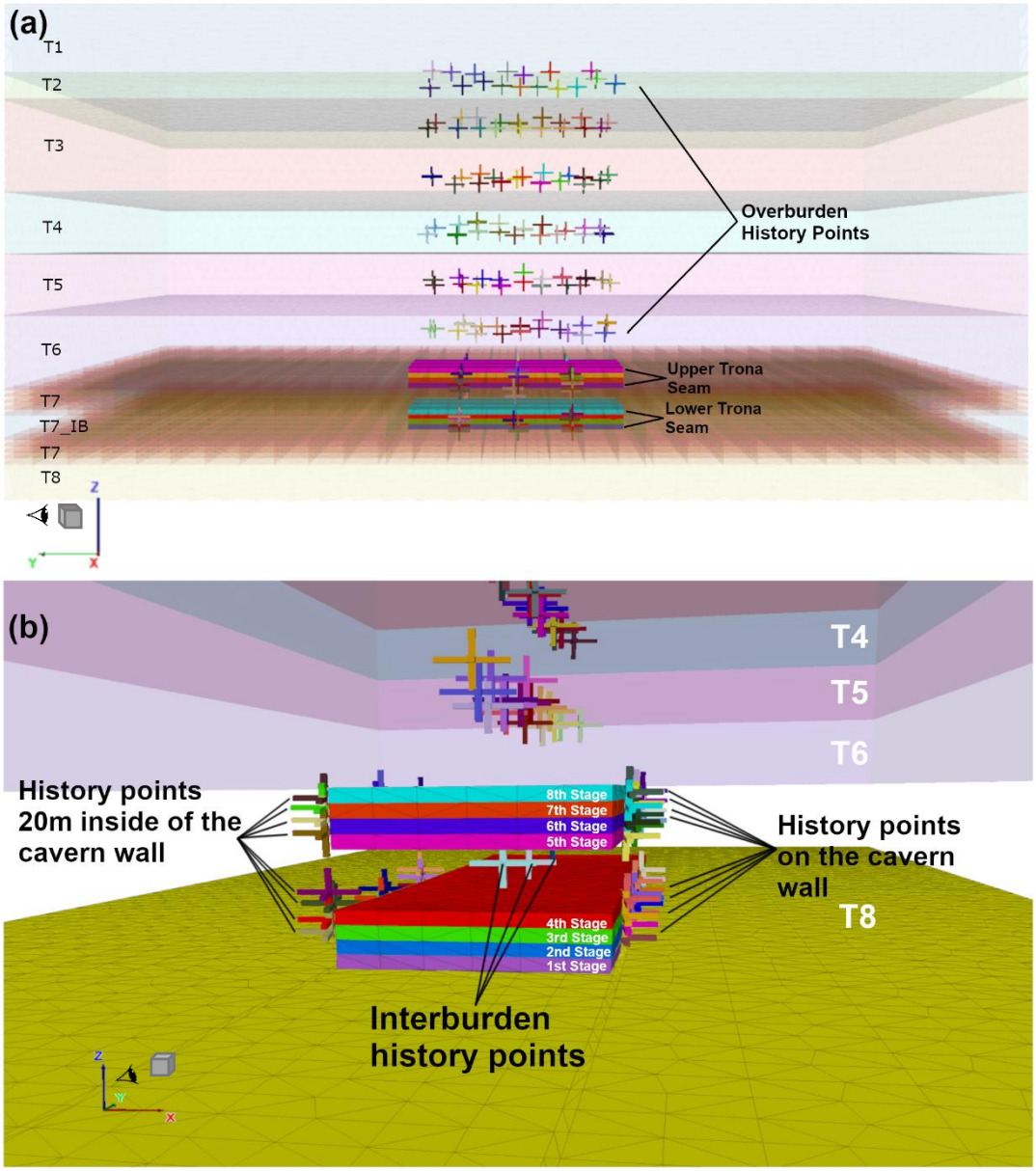

Figure 4.3 History points within the (a) overburden and (b) the cavern wall, interburden, and 20 m inside of the cavern wall

4.2 Stress Distribution within the Strata due to Production in a Single Cavern

The first stage of the simulation was to vanish the unbalanced forces before starting to simulate the production steps. To achieve that, the model was run with elastic and plastic material properties without removing any of the layers. Figure 4.4 shows the unbalanced force history.

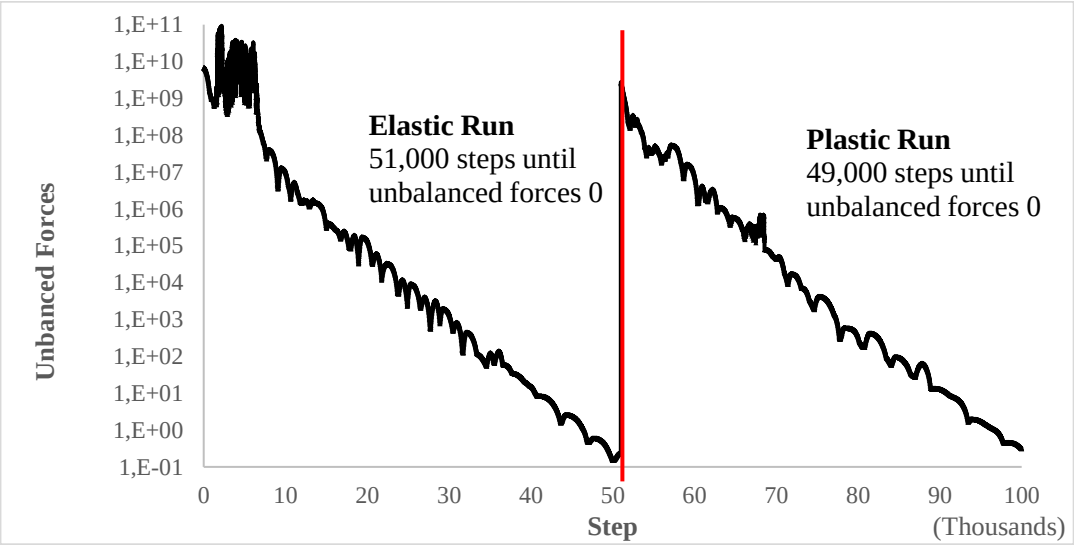

Figure 4.4 The unbalanced force history in elastic and plastic stages

After the force balance was achieved, the trona layers were started to be removed from bottom to top (total computational time was 540 min). The field observations in real trona solution mines point out that the thin interburden composed of clay rubbles into the cavern and creates new contact surfaces with the upper layer as the production goes on layer by layer. To mimic this behavior the solution steps were continued until the roof yields down to the floor due to sagging. The following stage removes another trona layer at the top and this procedure was repeated for each of the sub-layers. During each of the eight production stages, the stress development and z-displacement were traced on the history points. The central history points in each layer above the cavern were selected along the cavern to compare the stresses. In Figure 4.5.a the history locations were shown along with stress distribution

contours after the first production stage. In Figure 4.5.b, following the completion of the lower seam after the fourth production stage, an increase in the minor principal stresses can be observed around the cavern. In Figure 4.5.c, after completing the production in the upper trona seam, the stresses are accumulating on the stiff layers, which are namely T3 and T4. Also, isometric view of the model was given with σ_1 stress contours for each independent layer in Figure A.2 in Appendix where the concentration of the stresses can be seen more clearly.

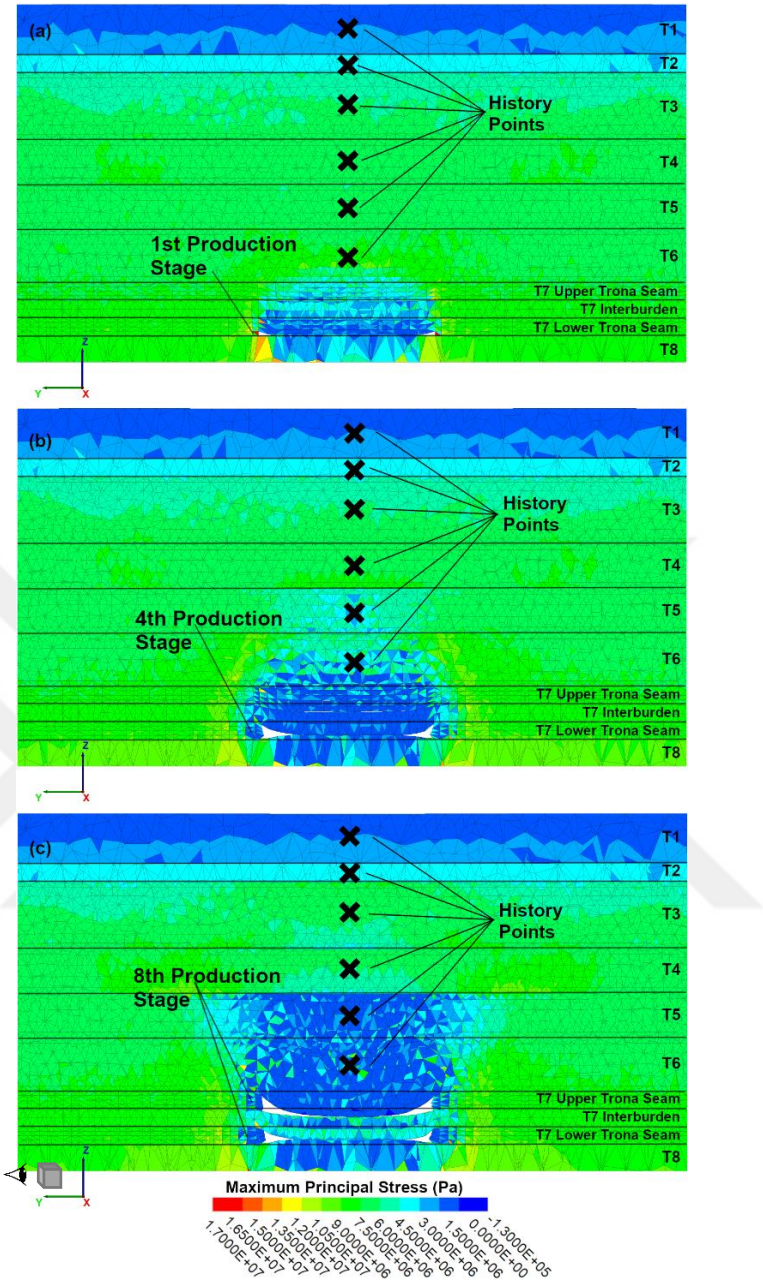

Figure 4.5 The maximum principal stresses (a) after removing the first trona layer at the bottom (b) after completing the lower trona seam (c) after completing production both in the upper and lower seams

History data of σ_1, σ_3 and the vertical displacement prove that during the production stress accumulates on the stiff layers. Figure 4.6 presents the σ_1 data from the overlaying strata history points during the whole production. The plot shows that the failure of the T6 layer occurs immediately after the first production stage. After the

third stage, the T5 layer fails. During the third production phase, while T5 was failing, the stress accumulates on T4 until it fails in the fourth production stage. The strength of the stiff layers after yielding can be observed from the low slope of decline in the stress graph after the failure of T4 just under 8 MPa. Thanks to the stiff T3 and T4 layers, in T1 and T2 layers no significant stress change was observed similar to the σ_3 values in Figure 4.7. Also, the deviatoric stress graph of the model is given in Figure A.3 in Appendix A.

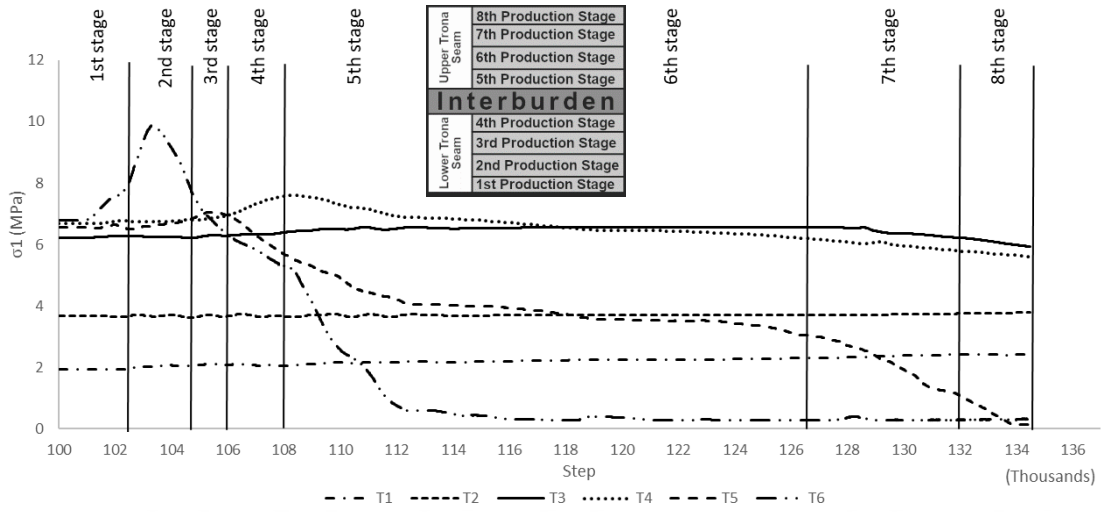

Figure 4.6 The major principal stress history during the production stages

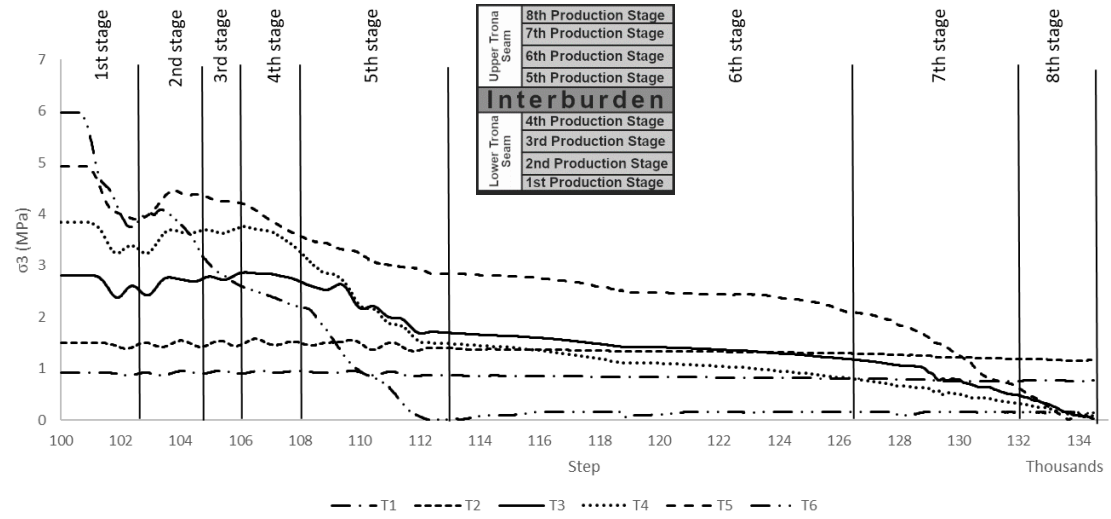

Figure 4.7 The minor principal stress history during the production stages

Finally, the vertical displacements of the strata can be seen in Figure 4.8, where failed T5 and T6 layers settle drastically but no significant sign of subsidence can be observed above T4. The maximum displacement in thin and relatively less stiff T4 layer is by 1.31 m. The displacements in the upper strata are 1.15 m in T3, 1.09 m in T2 and 0.98 m in T1. These results prove that the stiff layers above the trona seam do not move synchronously even in production of a single cavern. Unsynchronous and slow subsidence in trona solution mining operations with a series of neighboring caverns may result in serious consequences. Also, the stress graphs prove that high stress concentration may result in a violent failure. So, destressing in the stiff layers is necessary to sustain the ground control.

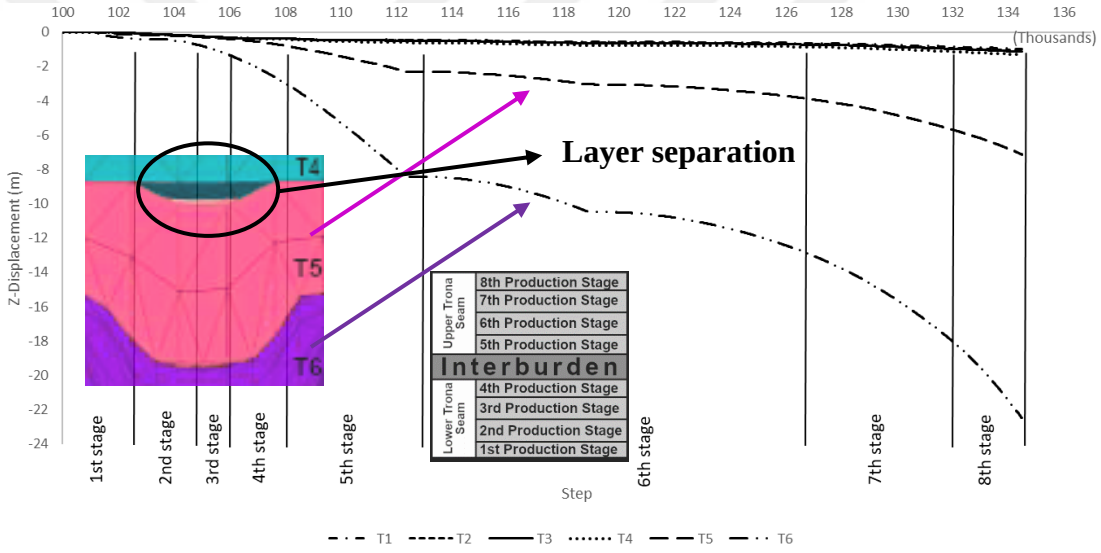

Figure 4.8 The vertical displacements of the strata

While production continues, abutment stresses develop on sides of the opening as a result of the large underground opening. In the presented study, a single cavern was modeled and subjected to the destressing operation. However, series of caverns are developed alongside where most of them operate simultaneously in real operations. In this situation, the abutment stresses become more vital in terms of the stability of the following caverns in the production sequence. This type of failures results in operational uncertainties, loss of solution and brine flow control, and even in the case of rigorous failures the caverns may be lost completely. To monitor the abutment

stresses around the cavern, as mentioned in the previous chapter, the history points were located with 50 m spacing in y-dimension on both sides. The history points on one side were directly placed on the cavern wall where on the other side the history points were placed 20 m inside of the cavern wall (Figure 4.9).

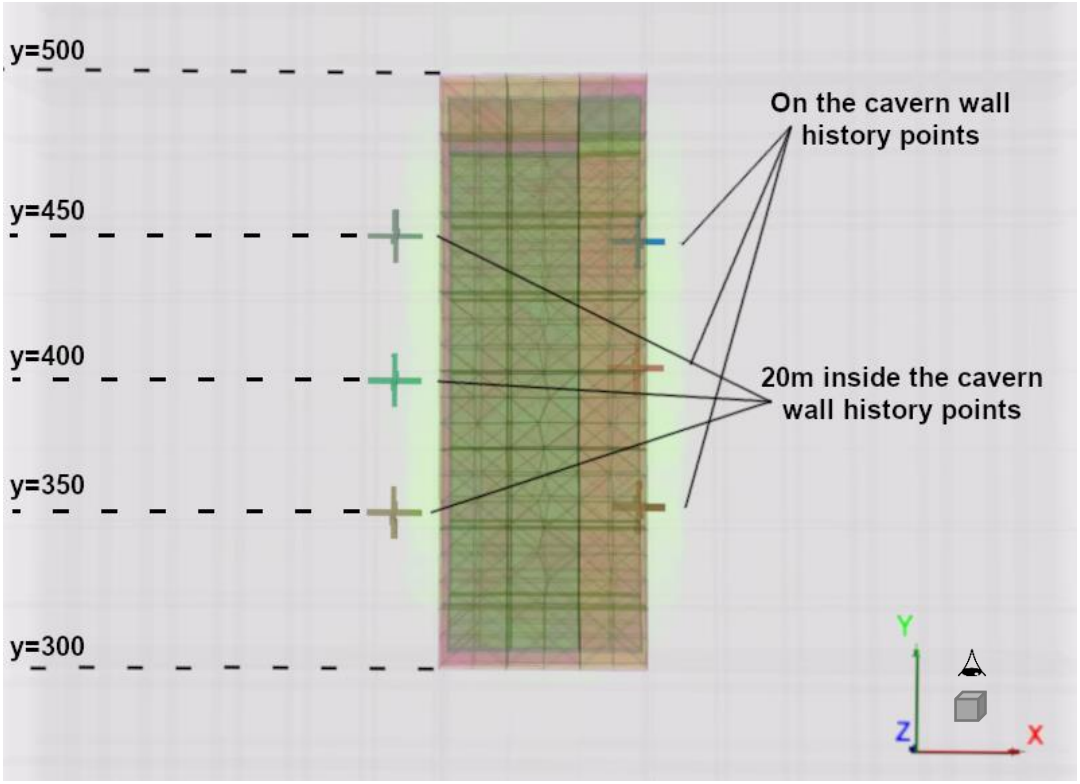

Figure 4.9 The history points along the cavern wall from the top view

In Figure 4.10 and Figure 4.11, during the first stage of production for the history point that is located at the same level in the middle (y= 400 m point), σ_1 value decreases drastically and trend can be observed with minor fluctuations on the cavern wall. In contrast to the cavern wall point, the point located 20 m inside the cavern wall decreases from 9-10 MPa to 1-2 MPa values after complete lower trona seam removal in fourth stage. Similar values are seen for the remaining stages. At the history point located on cavern wall at second stage production level, slight first stage σ_1 increase due to production can be observed. Again, similar to the first production stage level point, settles down with minor fluctuations during lower trona seam removal. The point located 20 m inside shows horizontal trend after complete lower

trona seam removal. But this time has a higher σ_1 value (3-4 MPa) than the first production stage level point. In similar fashion, history points on the cavern wall at third and fourth production stage levels show σ_1 stress increases in their correspondent stages. In both, there is a slight increase. Points located 20 m inside the cavern wall have the same trends as predecessors.

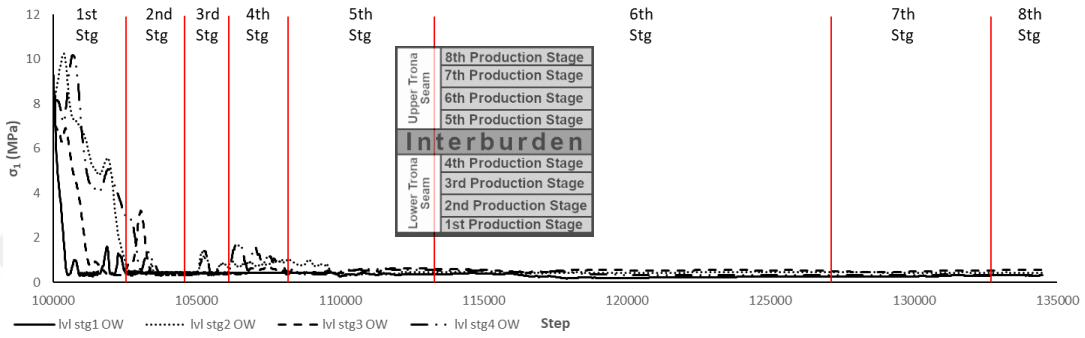

Figure 4.10 σ_1 history of the lower trona seam on the cavern wall

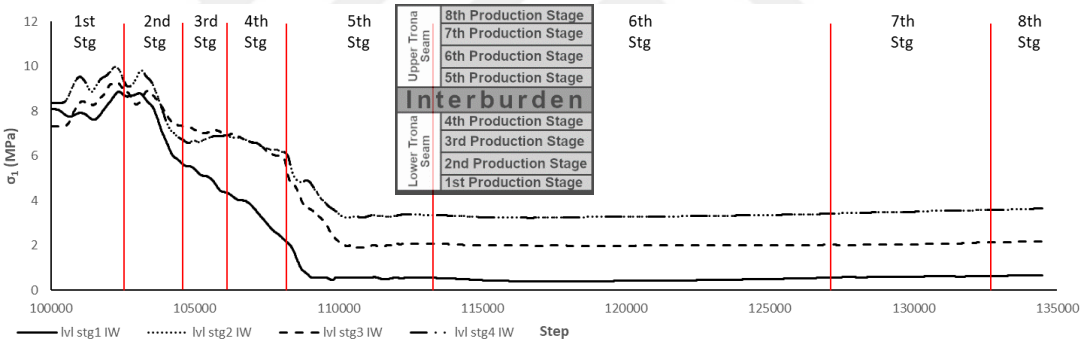

Figure 4.11 σ_1 history of the lower trona seam 20 m inside the cavern wall

After complete lower trona seam removal, with the start of the fifth stage, major disturbance of the σ_1 values at cavern wall point could be observed Figure 4.12. Stress at this point has a considerable increase to 25 MPa. On contrast to lower trona seam points, near to the end of the production, stress increase trend could be observed on the point which may be problematic for post-production period. Also, the same fifth stage disturbance could be observed at the 20 m inside point in Figure 4.13. After the fifth stage of production, a horizontal trend similar to the lower layer point is obtained. The point at sixth stage of production level doesn't show similar fifth

stage major stress disturbances for both on the cavern wall and 20 m inside. At the seventh production stage, the point at the same level show disturbance with maximum σ_1 value of 2-3 MPa. A major increase starting from the fifth stage could be seen on the same level 20 m inside point. For the final stage at the uppermost layer point, a slight increase in the stress could be observed for the point on the cavern wall. Again, a major increase starting from fifth stage could be seen on the eight production stage level 20 m inside point similar to seventh stage level point. Also, the abutment stress readings from other history points are given in the Appendix A.

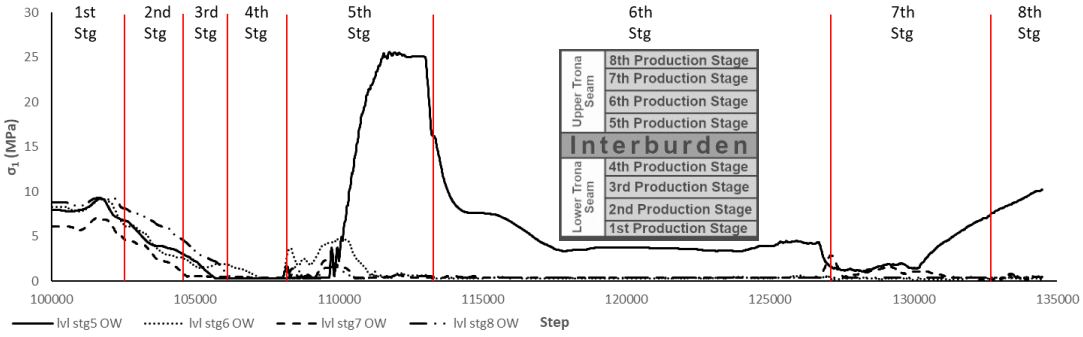

Figure 4.12 σ_1 history of the upper trona seam on the cavern wall

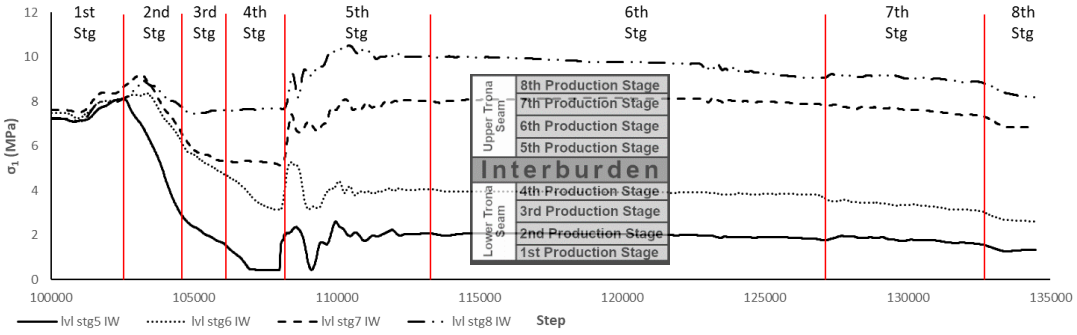

Figure 4.13 σ_1 history of the upper trona seam 20 m inside the cavern wall

In Figure 4.14, abutment stress development is given. At the virgin state (Figure 4.14.a) in-situ stress state is observed. After the first stage of production (Figure 4.14.b) abutment stress levels reach to 10 MPa concordant to the graphs given. Around the cavern, expanded stress contours can be seen until the end of complete

lower layer production (Figure 4.14.c, Figure 4.14.d, Figure 4.14.e). With the start of the first upper layer production stage (Figure 4.14.f) stress contour expansion at the lower layer levels is stopped where upper layer stress contours started to enlarge until the end of last stage (Figure 4.14.g, Figure 4.14.h, Figure 4.14.i).

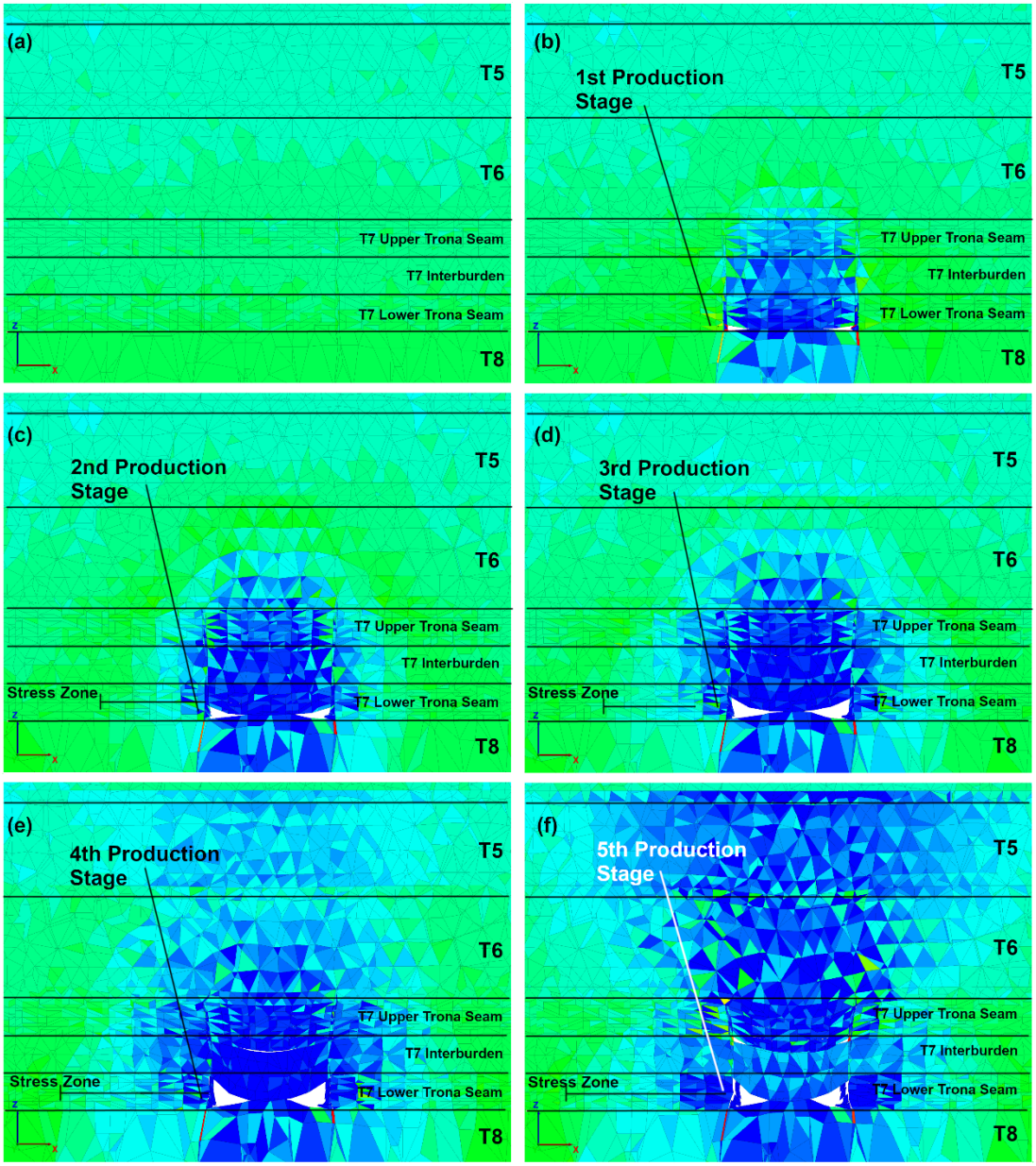

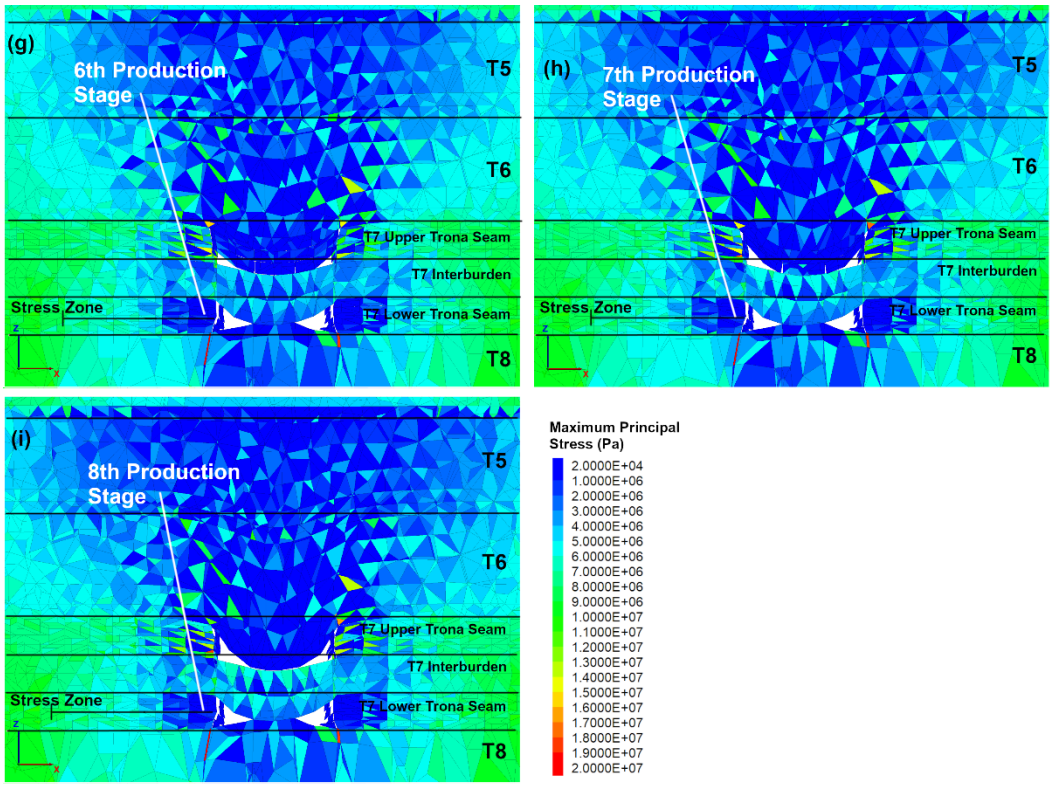

Figure 4.14 The maximum principal stresses at (a) the virgin state, (b) after the first stage of production, (c) after the second stage, (d) after the third stage, (e) after the complete lower trona seam production, (f) after the fifth stage of production, (g) after the sixth and (h) seventh stage of production, and (i) complete upper and lower production

It can be deduced that major σ_1 stress increase occurrences on the cavern walls are after the first sub-layer removal of the respective layer i.e., first lower layer or first upper layer removal. Failure of the pillars is imminent due to this stress increase. In this condition succeeding stage abutment stresses have no significant importance. As it mentioned this situation could cause serious outcomes especially for brittle material like trona. In addition to that, uneven stress distribution could be observed in real life due to the inhomogeneous nature of rock mass, discontinuities etc.

4.3 Validation and Verification of DFN as a Destress Modeling Technique

This study embraces the discrete fracture networks (DFN) for the modeling of destressed strata. However, first of all, DFN must be proven to be a valid method for the simulation of stress relaxation. Using the ITASCA 3DEC code, the fracture network was induced into the stiff strata. A set of discrete, planar, and finite sized fractures were formed in the rock mass. For the fracture size distribution, as it is widely acknowledged to exist in nature, the power law was used. The fracture size limits were set between 50 m to 100 m. The position distribution of the fractures was defined to be uniform in 3D. For the orientation distribution of the fractures again uniform distribution was selected so that the dip angle and dip directions of the fractures can distribute uniformly. Finally, the fracture density was selected as 0.25. However, the field data may always provide a better presentation.

To validate DFN as a destress modeling technique, a sample model was constructed (Figure 4.15). A DFN pattern was implemented in upper stiff layer (T3) conforming to the mentioned input parameters. The destressed region is placed just above the cavern with same horizontal dimensions. Similar to the first model, the history points on the same locations were defined to track σ_1, σ_3, and z-displacements. To validate the DFN, the original model without DFN (shown by 'woDESS') was compared with the model that involves the sample 'DESS'. Data observed on the same history points were compared in the stiff layers (T3 and T4).

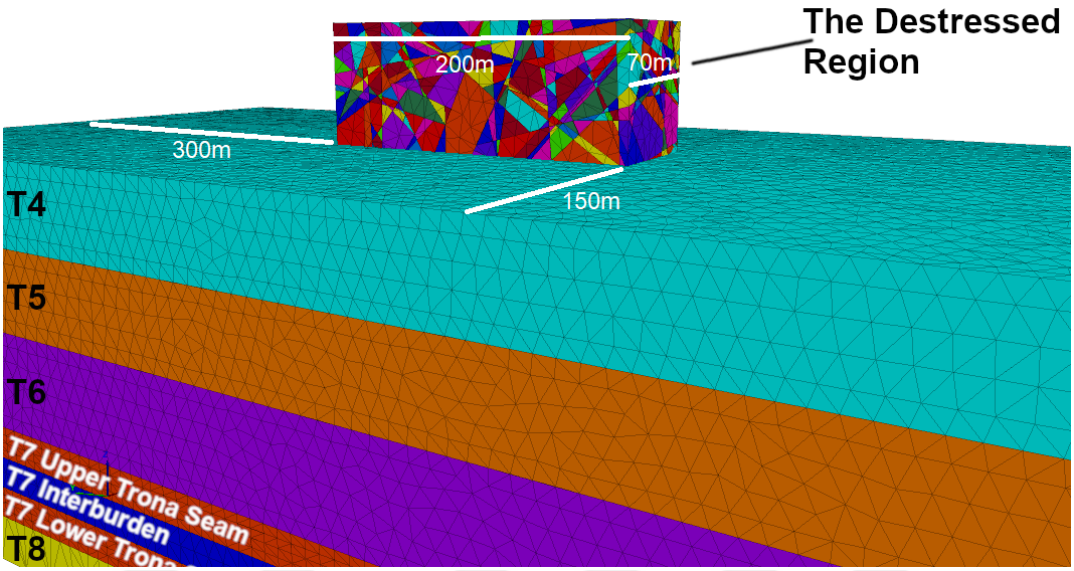

Figure 4.15 Validation of DFN with relaxation of T3 layer

By implementing DFN on the upper stiff layer (T3), a decrease in the stress concentration was expected. As shown in the history data in Figure 4.16 the stress concentrations drop from 6.6 MPa in woDESS model to 5 MPa in the sample DESS model. Considering the stress reduction by 24%, DFN can be considered to be successful in simulating the stress relaxation and is a viable method for the imitation of destressing.

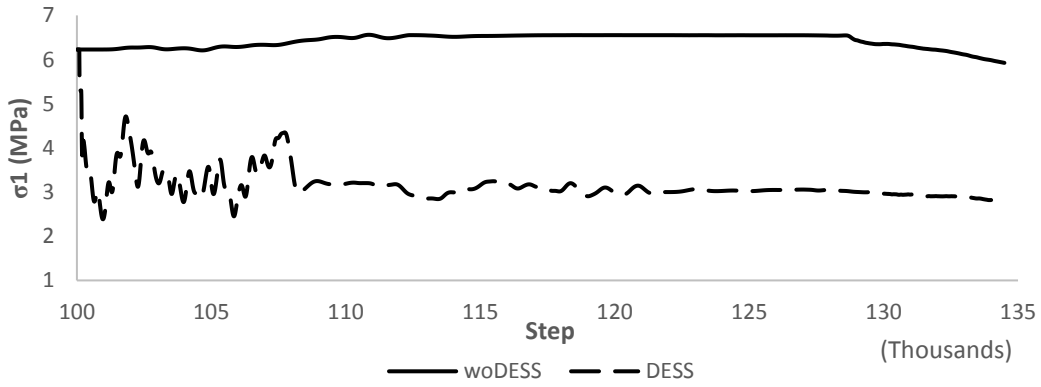

Figure 4.16 Comparison of the maximum principal stress in T3 layer with and without destressing

When the stress distributions of both cases are compared, for the first production stage, it can be noted that in the overburden strata tensile stress started to develop contrary to woDESS case (Figure 4.17). As the production goes on, the variation of stress distribution can be observed both in the overburden and around the cavern after the fourth production stage and the final production stage.

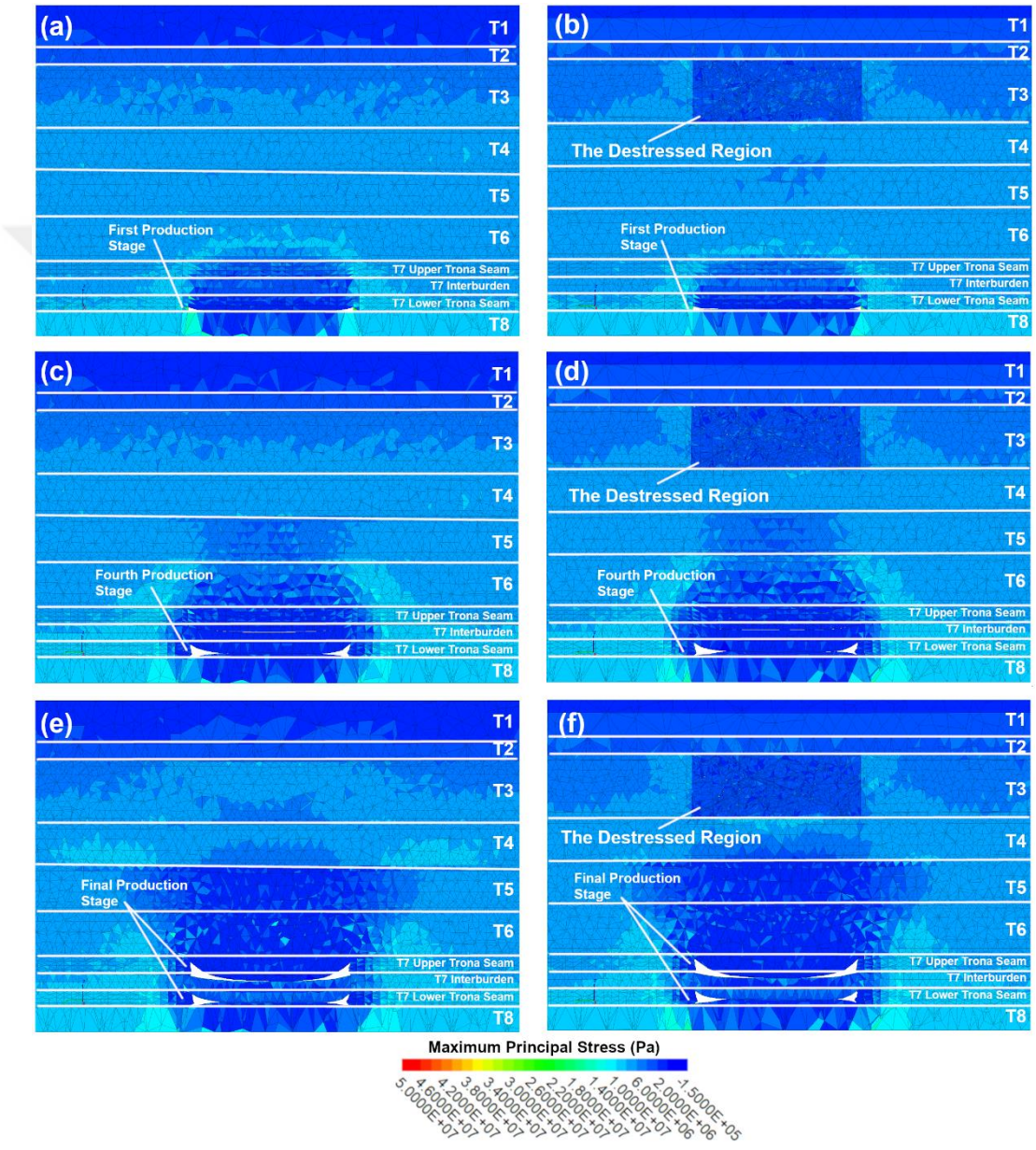

Figure 4.17 Comparison of the major principal stress distributions after the first stage of production (a) without destressing (b) with destressing, after the completion of the

lower trona seam (c) without destressing (d) with destressing, and completing the production both in the upper and lower seams (e) without destressing and (f) with destressing

Also, the yielding of the rock mass can be observed in Figure 4.18.a and Figure 4.18.b after the first production stage. This is a result of the tensile type yield due to caving. In Figure 4.18.c and Figure 4.18.d after the upper layer production is completed, and Figure 4.18.e and Figure 4.18.f after both of the seams were produced caving induces more plasticity above the cavern. This tensile type yielding continues with production and ends with failure of the overburden.

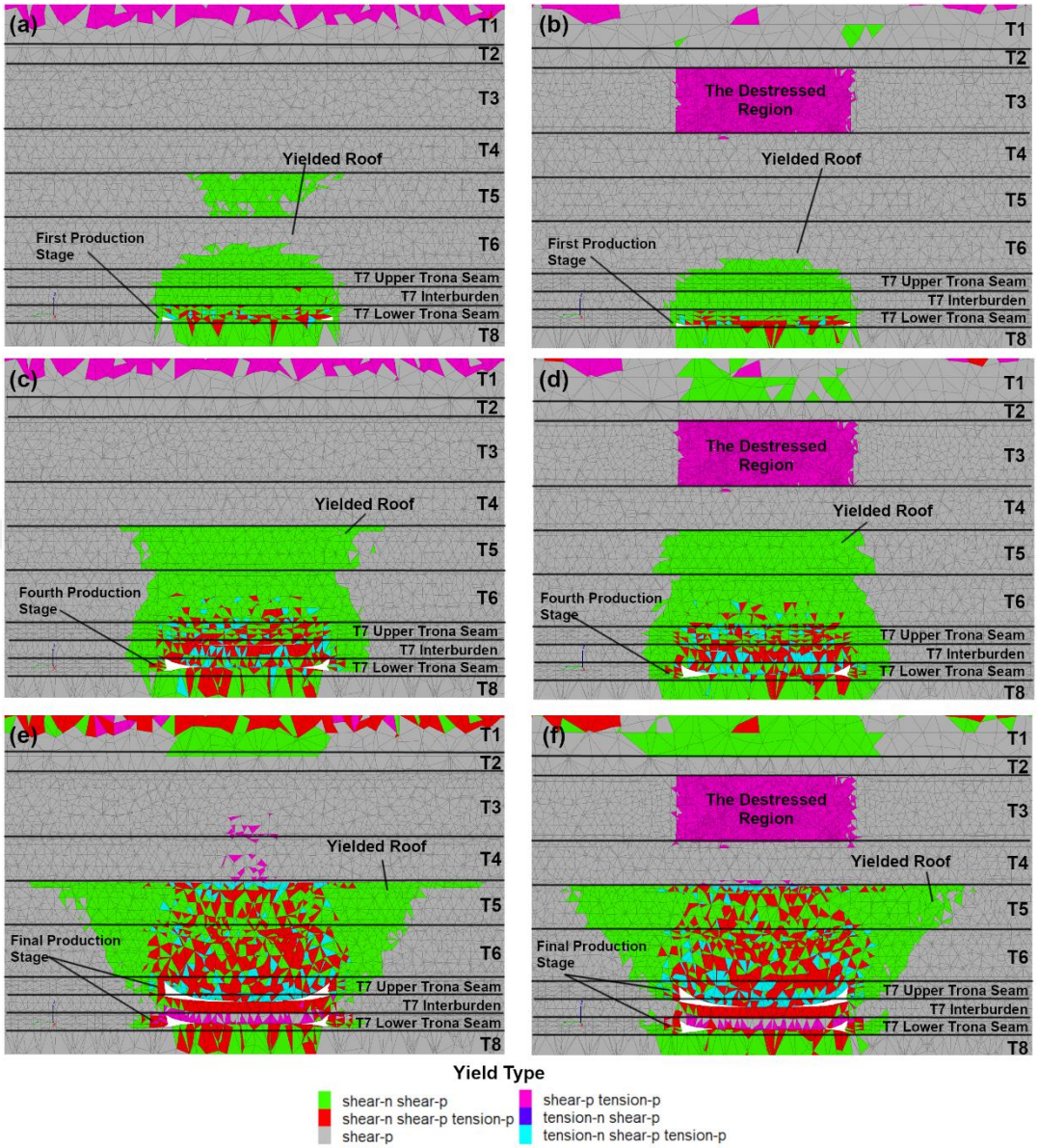

Figure 4.18 Yielded elements after first lower layer removal (a) without destressing (b) destressing, complete lower layer removal stage (c) without destressing (d) destressing, and both complete upper and lower layer removal (e) without destressing (f) destressing

To conclude, DFN was proven to be a valid method to use at destressing simulation. The results presented above clearly show that significant stress relaxation occurs due to implementation of DFN in the upper stiff layer (T3). Also, the history plot shows that more than 20% stress change could be obtained. In addition, the differences in

the stress distribution and yielded elements imply that the failure of the stiff overburden strata could be controlled by destressing.

4.4 Determination of the Suitable Destressing Pattern

Although DFN was proven as a valid method for the simulation of destressing, the validation model implemented the fracture network on the whole strata above the cavern. In field-practise, inducing a fracture network on such a large space is challenging due to economical and practical reasons. As discussed in Chapter 2.6, the fractures initiated on small regions are expected to propagate the inherent network to affect a larger area. For this reason, different destressing patterns were studied to determine the economically and technically viable solution. This study investigated two alternative destressing patterns, which are the 'ribbon type' and the 'borehole type'. Both of the patterns, can be implemented by hydraulic fracturing , destress blasting or destress conditioning. The study flowsheet is given in Figure 4.19. This study does not intend to simulate the fracture propagation but only investigates the effects of the induced fracture network on the rock mass.

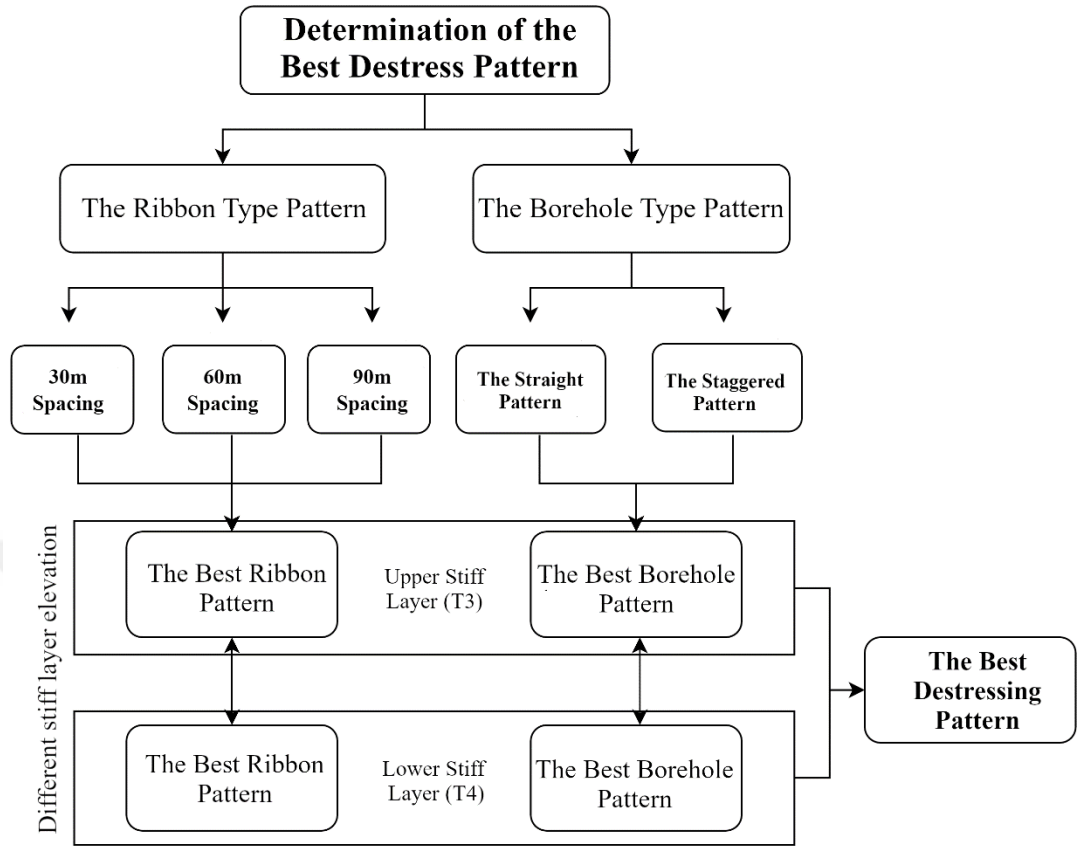

Figure 4.19 Determination of the best destressing pattern

4.4.1 The Ribbon Type Destressing Pattern

Destressing the whole stiff layer as in the validation part is not feasible in any real mining operation. When cost of the operation, labor requirements, and control of destressing on a large area is considered, it is not viable to target the whole strata. Due to this reason, the area above cavern on the stiff layer was divided into multiple slices, called “Ribbon”, with a smaller volume. Destressing with the ribbon type pattern covers the whole stiff layer from bottom to top on the vertical dimension. In x-dimension, the destressed regions have equal length with the cavern, which is 70 m and aligned with the cavern borders. In the y-dimension the ribbons were distributed evenly using three different spacings within the stiff layers T3 and T4. The spacings were designed to be 30 m, 60 m, and 90 m due to operational

challenges. In the ribbon pattern with 30 m spacing (coded as RN_30), four evenly spaced destressed zones were aligned with the mentioned properties (Figure 4.20.a, Figure 4.20.b). When the spacing is 60 m (coded as RN_60) only three ribbons may fit into the region (Figure 4.20.c, Figure 4.20.d). Finally, when the spacing is 90 m (coded as RN_90) two ribbons could be fitted within the cavern borders as shown in Figure 4.20.e and Figure 4.20.f.

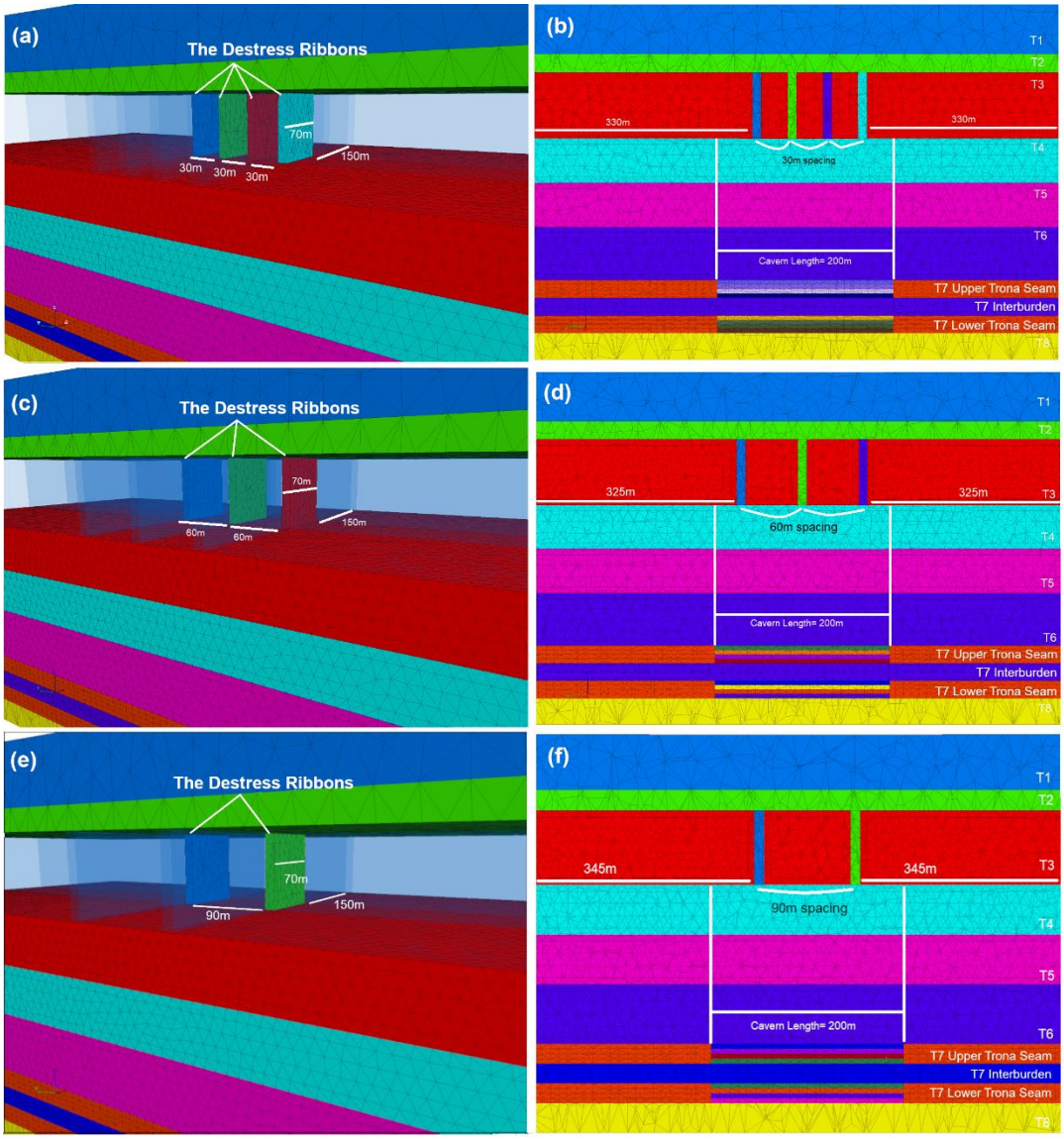

Figure 4.20 The model body, dimensions, and distances of RN_30 pattern in (a) isometric view and (b) side view, RN_60 (c) isometric view and (d) side view, RN_90 (e) isometric view and (f) side view

4.4.2 The Borehole Type Destressing Pattern

The main motivation of the borehole pattern is to offer a more practical approach compared to the ribbon pattern. DFN of borehole types similarly stretches out from the bottom to top of the respective layer in z-dimension. In x-dimension, the boreholes were distributed with an equal spacing within the cavern dimensions and placed just above the cavern. The boreholes were placed vertically in the respective layer covering up to 4 m of fractured region. Again, due to practical reasons two different patterns were applied, which are namely “The Straight Pattern” and “The Staggered Pattern”. As the name implies, in the staggered pattern (BH_STG), the row of boreholes were placed with 20 m spacing where the following row of the boreholes were placed in the middle of the former boreholes (Figure 4.21.a and Figure 4.21.b) or simply in the staggered formation. In the straight pattern (BH_STR), the boreholes were placed symmetrically and distributed equally just over the cavern with 20 m spacing in x- and y-dimensions (Figure 4.21.c, Figure 4.21.d).

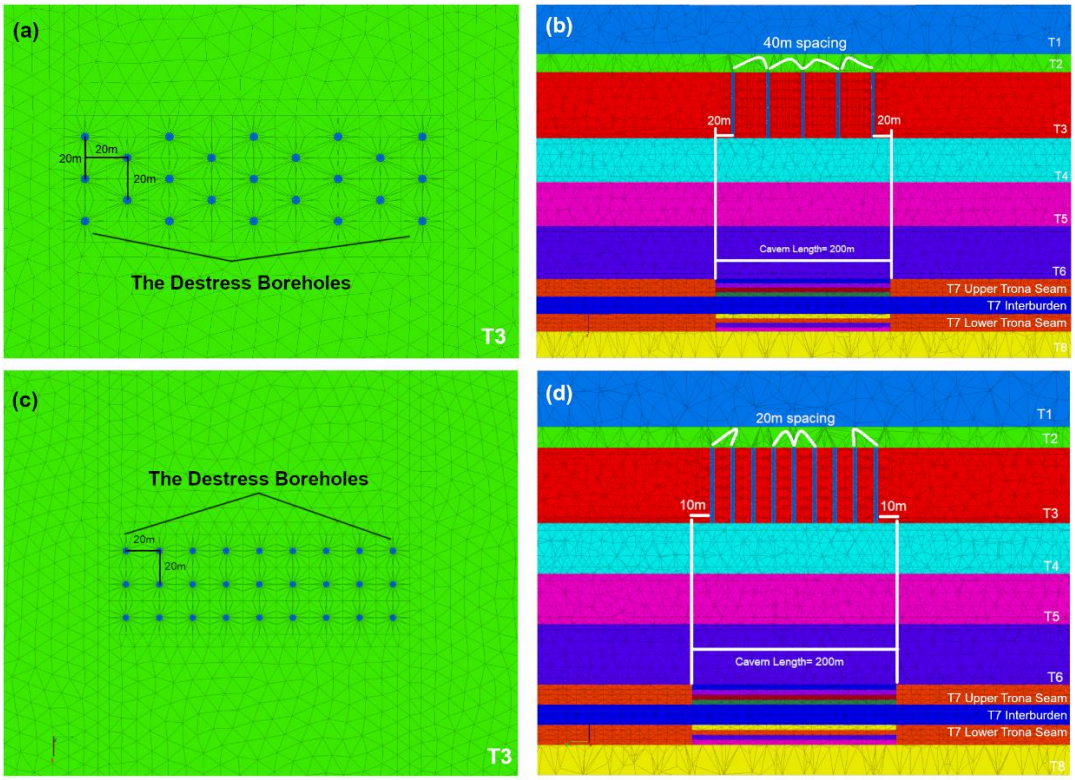

Figure 4.21 The borehole pattern dimensions, distance, and the model body of the BH_STG (a) top view and (b) side view, BH_STR (c) top view and (d) side view

Both the ribbon and the borehole patterns were also implemented in T4 to compare the effect of destressing depth, thickness of the relaxed layer along with the patterns (Figure 4.22.a, Figure 4.22.b). The same destressing scheme was applied only by changing the implemented layer.

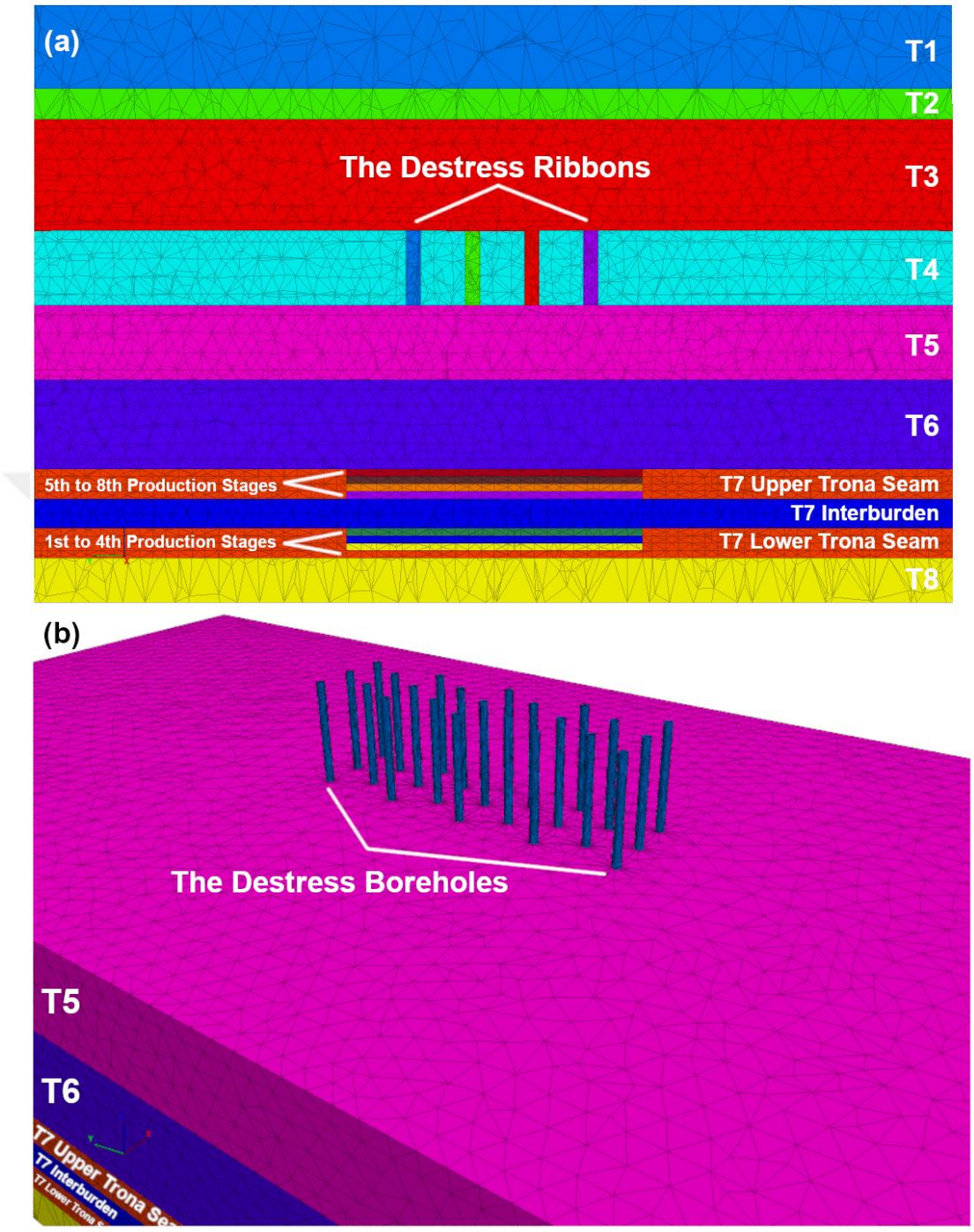

Figure 4.22 The destressing patterns in T4 (a) the ribbon pattern with 30 m spacing and (b) the staggered borehole patterns

CHAPTER 5

RESULTS AND DISCUSSION

This chapter presents the results of computational models to find out the best destressing practice in solution mining. Considering the stiff layers (T3 and T4) above the trona deposit were thick, the initial research attempt was to identify the suitable location for implementation of the destressing operation. In the previous chapter, DFN was proven to be a viable method for simulation of the induced fracture network. Based on this fact, various destressing patterns were modeled and compared under this chapter. The objective was to find the pattern providing the required stress relaxation within the strata. The problem constraints were the operational viability and the economy. Structure of the chapter is given as follows:

- to decide on the best spacing for the ribbon pattern in the upper stiff layer (T3) by comparing 30 m (RN_30), 60 m (RN_60) and 90 m (RN_90) distance between the destressed regions,
- to decide on the best borehole pattern in the upper stiff layer (T3) layer by comparing a staggered (BH_STG) and straight (BH_STR) drillhole pattern
- to decide on the best destressing pattern in the upper stiff layer (T3) comparing the model results,
- to compare the effect of destressing in the upper (T3) and lower (T4) stiff layers by comparing the best practice of the ribbon (RN) and the borehole (BH) patterns,
- to decide on the best destressing pattern in an overall sense.

5.1 Destressing with the Ribbon Pattern

Firstly, the best practice was intended to be determined by comparing the different spacings of the ribbon patterns in the upper stiff layer (T3). The spacing between the

destressed layers were set to 30 m (RN_30), 60 m (RN_60), and 90 m (RN_90). The models were coded with 'RN' for the ribbon and the spacing separated by an underscore. Comparing the induced stress distribution by relaxing the stratum, the best spacing was found. As described before, the ribbons were implemented to cover the whole stratum on the z-dimension. However, the relaxation spans only within the cavern's projected area on the horizontal plane. The spacing was adjusted on the y-dimension as shown in Figure 5.1.

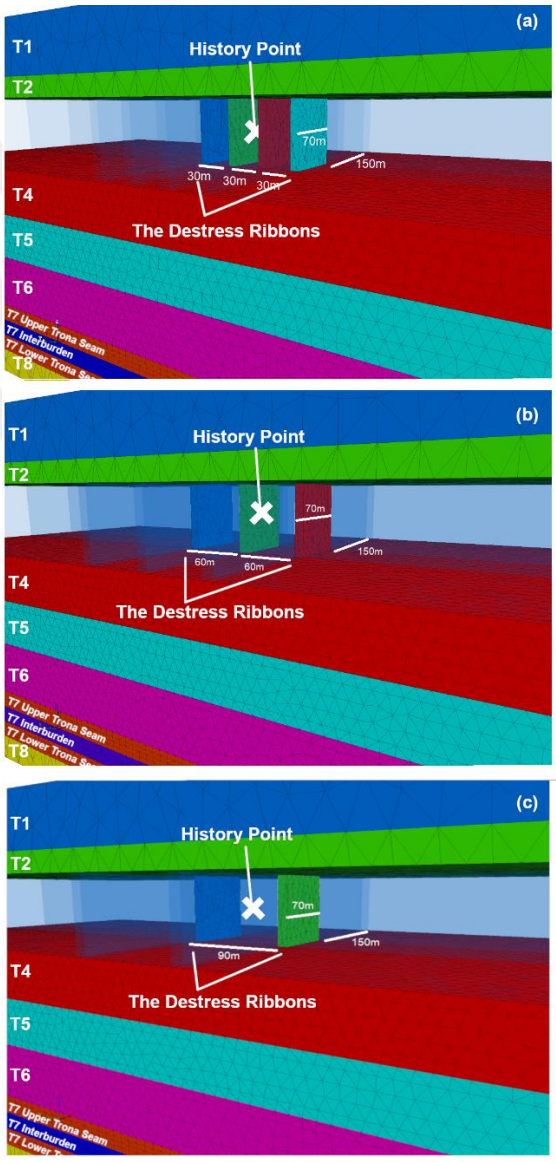

Figure 5.1 Spacing between destressed ribbons (a) 30 m (RN_30) (b) 60 m (RN_60) and (c) 90 m (RN_90)

The major principal stress (σ_1) history in all of the models showed that both RN_30 and RN_60 patterns caused stress levels to increase in the upper stiff layer (T3), in between the ribbons where there no fracture is intended by destressing (Figure 5.2). This increment was observed to be 8% and 10% for RN_30 and RN_60 models. That is due to the nature of stress flow, which drives stresses to accumulate on the stiff layers. Stress increment between the ribbons increase the likelihood of these regions to fail due to two reasons. The first one is the disturbance of the in-situ stress field. Because the ribbons are fractured, the confinement in between the ribbons will also diminish. As confinement decreases, the rock strength would be expected to degrade. The other reason is the increasing stress concentration. The σ_1 history records prove the idea. With no destressing, the maximum principal stress was around 6.5 MPa. However, the RN_30 pattern increases the concentration up to 7.1 MPa while it is 7.2 MPa for RN_60 pattern for the initial stages of production. As opening dimensions propagate the stress level drops gradually, which indicates the failure of the stratum without posing a sudden collapse risk. On the other hand, the stress level was observed to be around 6.2 MPa for the ribbon spacing of 90 m (RN_90). It shows that 90 m spacing is not sufficient to attain the mass scale relaxation goal. When the destressing operation is performed within the upper stiff layer (T3), the stress relaxation was also observed in the lower stiff layer (T4) (Figure 5.3). It was by 17% for RN_30 case, 21% for RN_60 case, and 23% for RN_90 case.

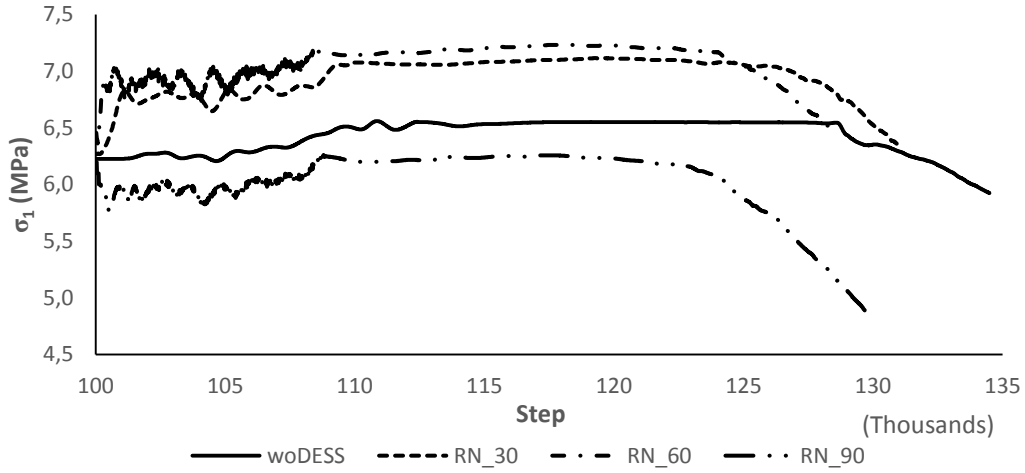

Figure 5.2 σ_1 history in the upper stiff layer (T3) when the same layer is destressed with various ribbon spacings

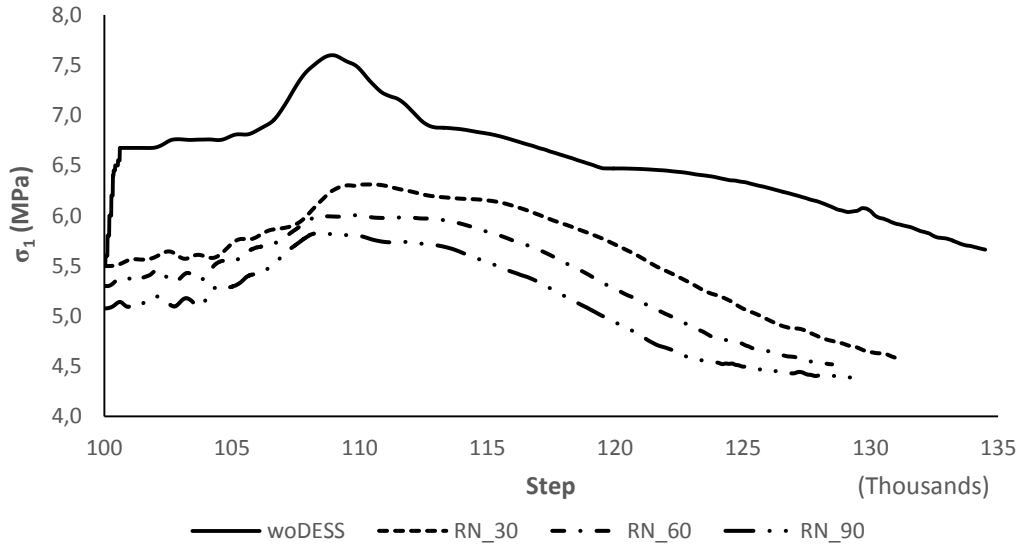

Figure 5.3 σ_1 history in the lower stiff layer (T4) for destressing the upper stiff layer (T3) with various ribbon spacings

The simulations show that the stress increase in the upper stiff layer (T3) within the unweakened zones contributes to the failure of the stratum. Since the objective of the study was to reduce the sudden collapse risk by failing the stiff layers under control,

the ribbon pattern was proven to be useful. In addition to the stress plots, stress contours of all cases were given after the first production stage (Figure 5.4), after completing the lower seam at the fourth production stage (Figure 5.5), and after exploiting the whole deposit in the eighth production stage (Figure 5.6). With no destressing and right after the first production stage it can be seen that there is no obvious stress concentration on the stiff layers. However, after the lower trona seam was produced, the stress accumulations both on the overburden and around the cavern can be seen.

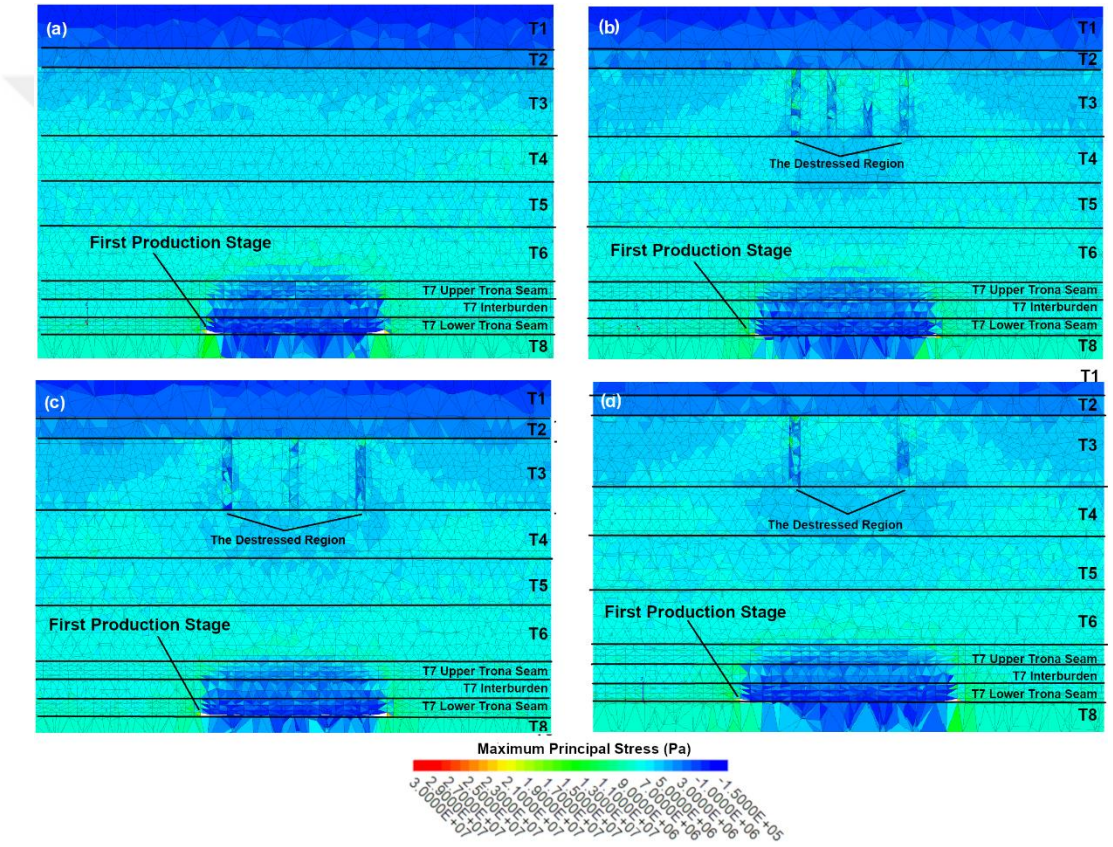

Figure 5.4 The major principal stresses after the first production stage in a) woDESS b) RN_30 c) RN_60 d) RN_90

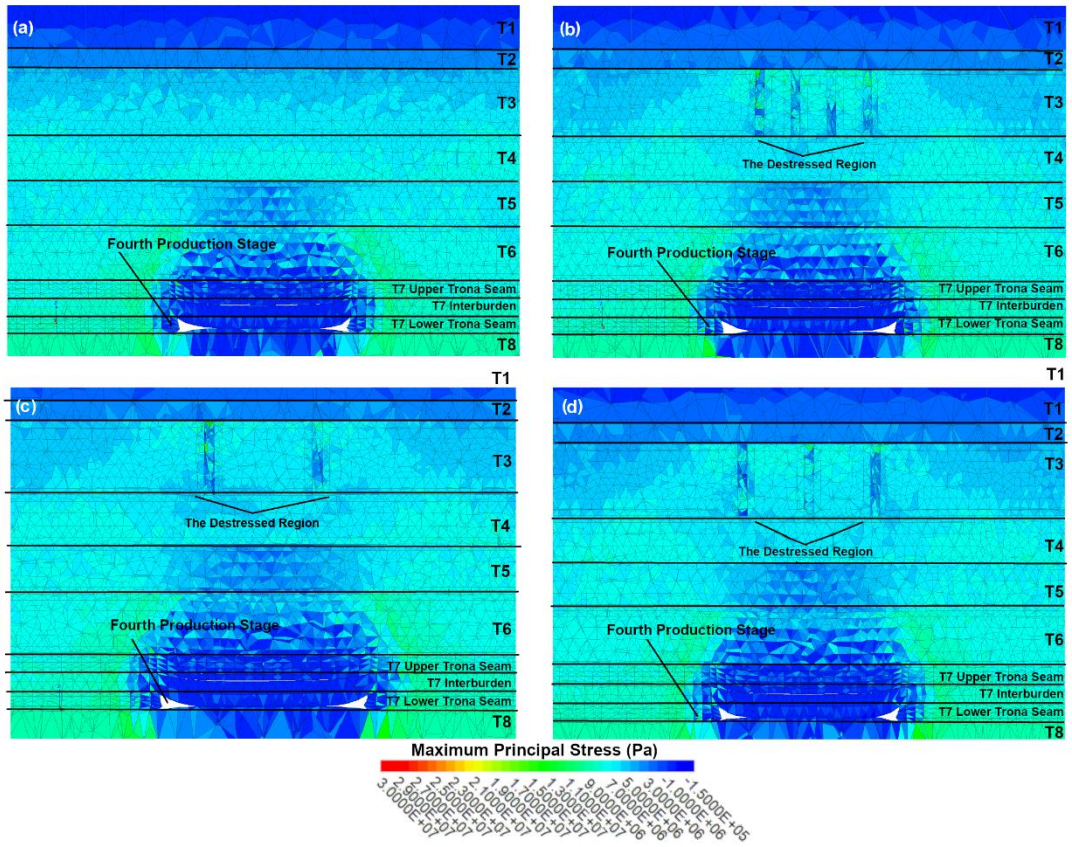

Figure 5.5 Stress distributions after fourth production stage in a) woDESS b) RN_30 c) RN_60 d) RN_90

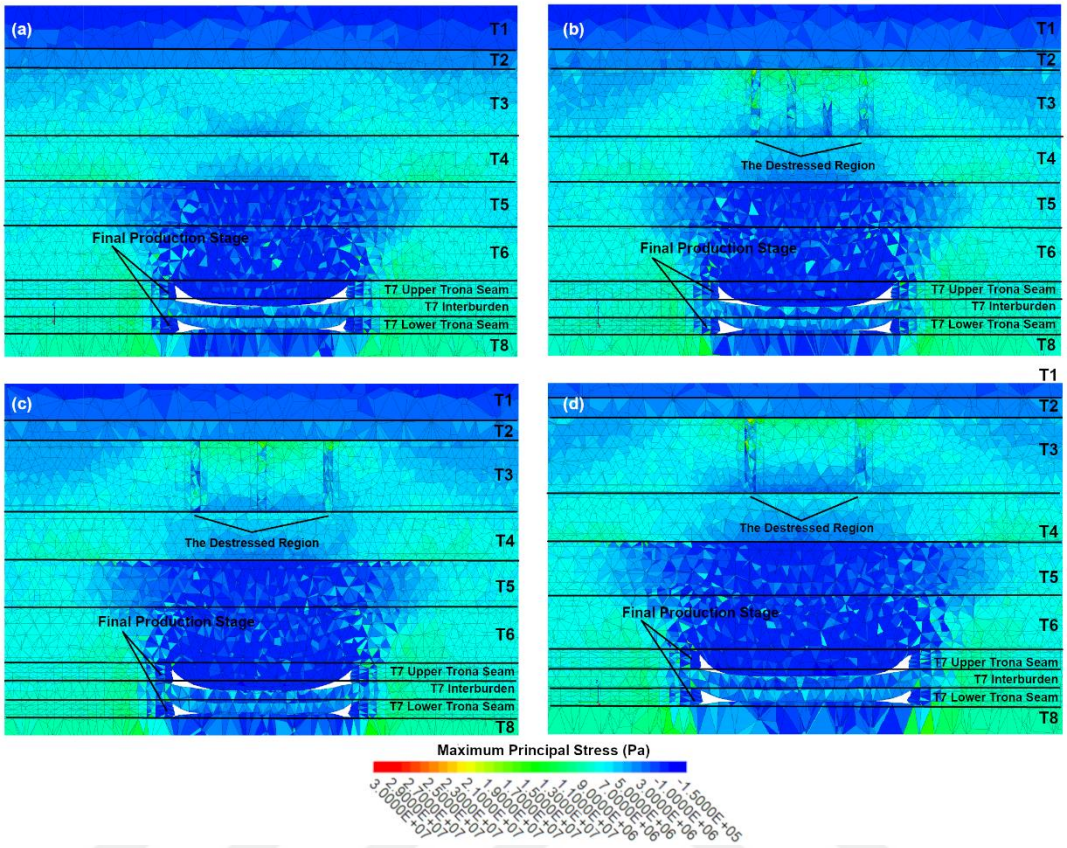

Figure 5.6 Stress distributions after the eighth production stage in a) woDESS b) RN_30 c) RN_60 d) RN_90

The yielded elements and respective states are given after the first (Figure 5.7), fourth (Figure 5.8), and final production stage (Figure 5.9). It can be seen that the yielded elements progress towards the topographical surface as the trona seams were produced. In addition, the effect of destressing in the stiff layers can also be observed. The models prove that the density of the fracture network correlates to the ribbon spacing. As the spacing decreases, the rock mass is deformed and relaxed more intensely.

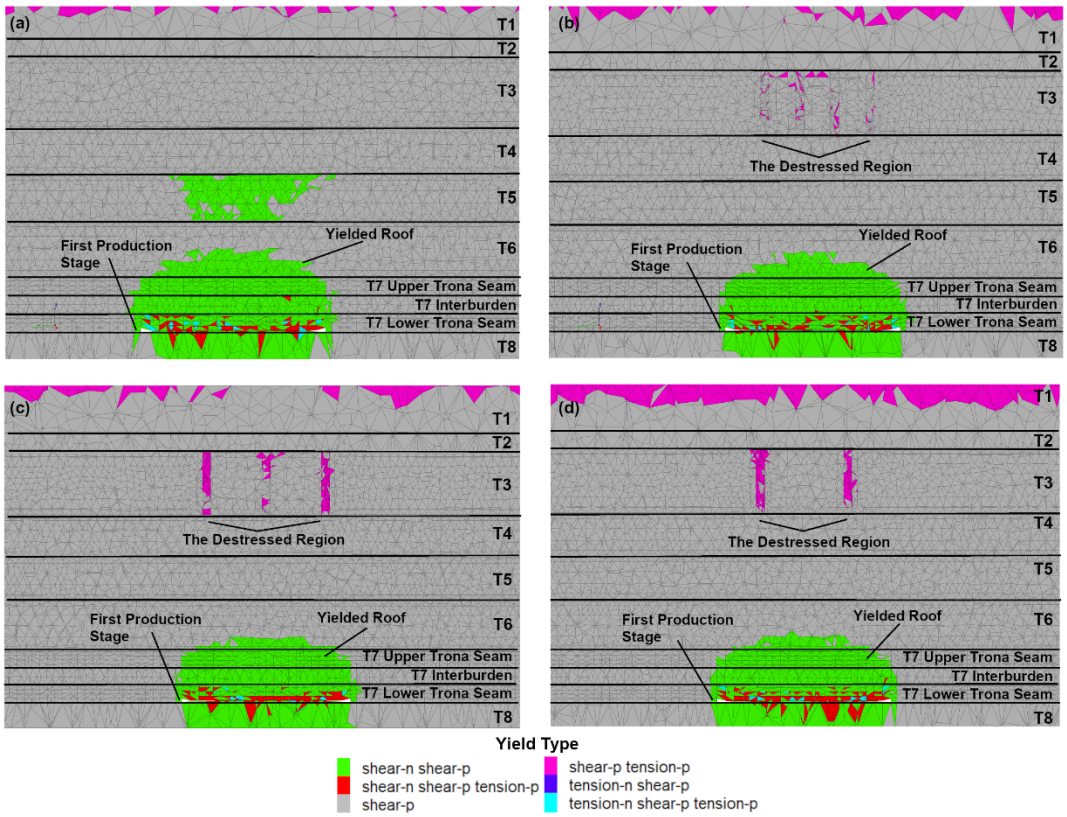

Figure 5.7 The yielded elements after removal of the first layer in the lower seam (a) woDESS, (b) RN_30, (c) RN_60, and (d) RN_90

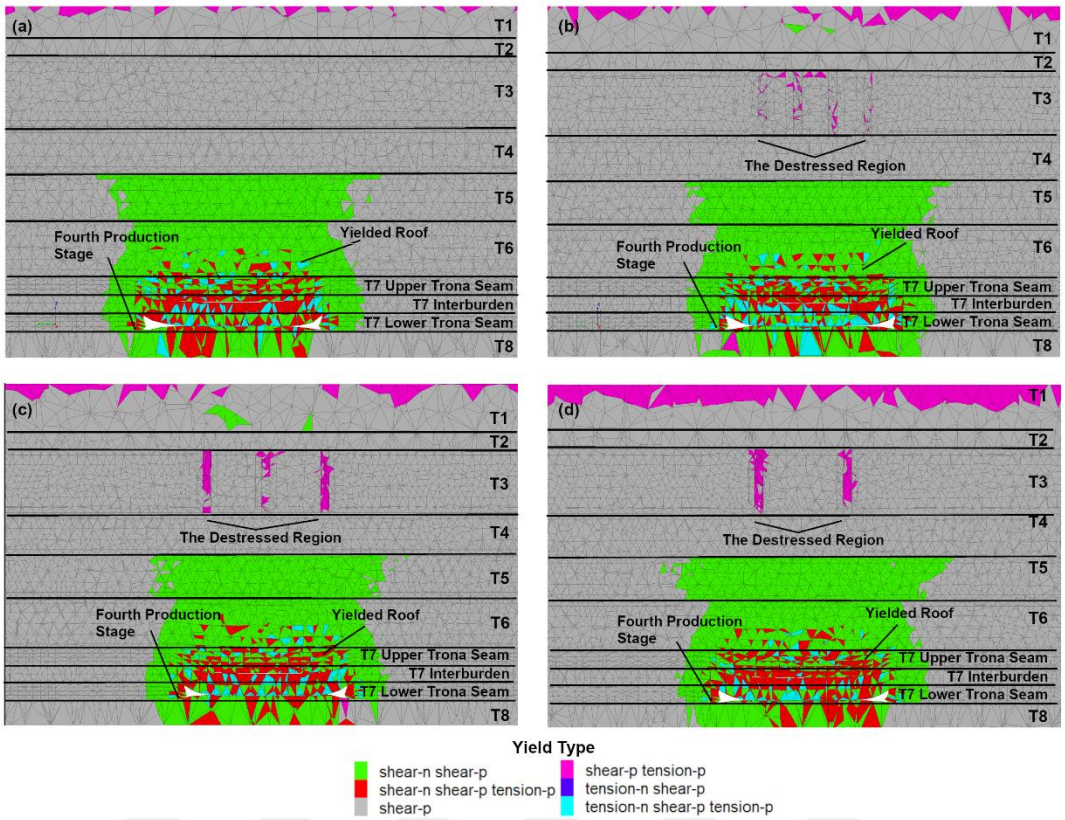

Figure 5.8 The yielded elements after completing the lower trona layer (a) woDESS, (b) RN_30, (c) RN_60, and (d) RN_90

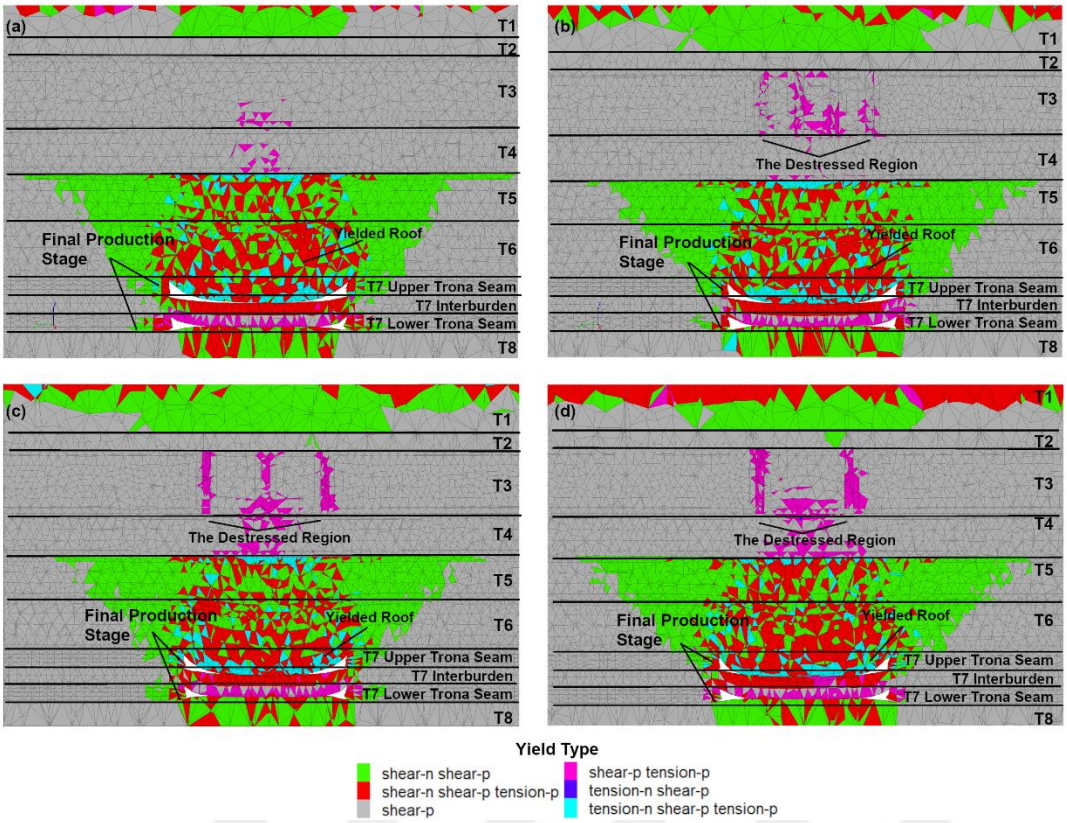

Figure 5.9 The yielded elements after completing both the lower and upper trona seams (a) woDESS, (b) RN_30, (c) RN_60, and (d) RN_90

Regarding the stress plots, contour maps and the yielded element visuals RN_30 and RN_60 are the most effective spacings for the ribbon pattern. There is no significant variation (around 2%) between the stress reduction effects of RN_60 and RN_30. RN_90 cannot provide the expected stress relaxation. Also, considering the dimensions of the intended area (70 m in width and 75 m in height), the destressing is not easy to implement. RN_30 has four ribbons whereas RN_60 has only three. By considering both the mechanical and practical advantages, RN_60 was concluded to be the most suitable pattern.

5.2 Destressing with the Borehole Pattern

Although the ribbon pattern was proven to be useful for destressing, inducing a fracture network on a large span is both costly and difficult. Alternatively, the

borehole pattern may pose a viable alternative to create a similar fracture network for destressing. To check the performance of the borehole pattern in terms of stress relaxation, the numerical models were prepared to compare the stresses in the rock mass before and after destressing. As mentioned before, two different layouts were studied: namely staggered (BH_STG) and straight (BH_STR) patterns (Figure 5.10).

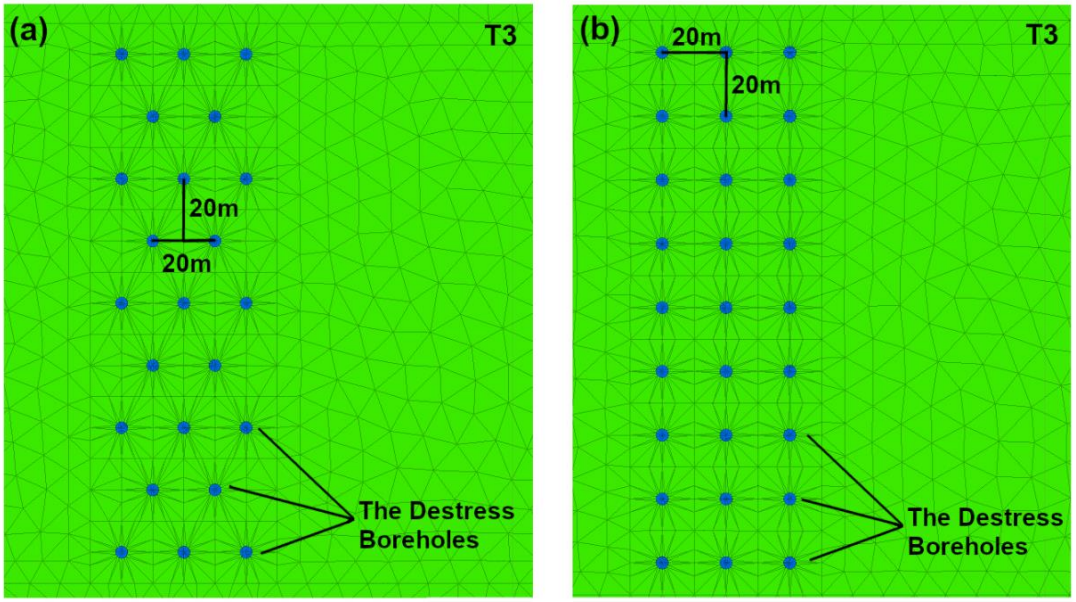

Figure 5.10 The top view of the (a) staggered (BH_STG) and (b) straight (BH_STR) patterns of the borehole destressing

In Figure 5.11, it can be seen that both BH_STR and BH_STG patterns in the upper stiff layer (T3) lead to a stress increase in the same layer (T3) similar to RN_30 and RN_60. Compared to the model with no destressing (6.6 MPa), 22% stress increase can be observed in BH_STG where 46% increase was observed in BH_STR with a maximum principal stress of 8.0 MPa and 9.6 MPa respectively. Unlike the ribbon pattern simulations, no stress relaxation was observed in the lower stiff layer (T4) (Figure 5.12). For BH_STR case, there is a 19% stress increase in lower stiff layer (T4) relative to the woDFN case and similar stress values were observed in BH_STG case. It is obvious that both cases achieve destressing goals by increasing the stress accumulation on the stiff stratum, which is followed by the failure.

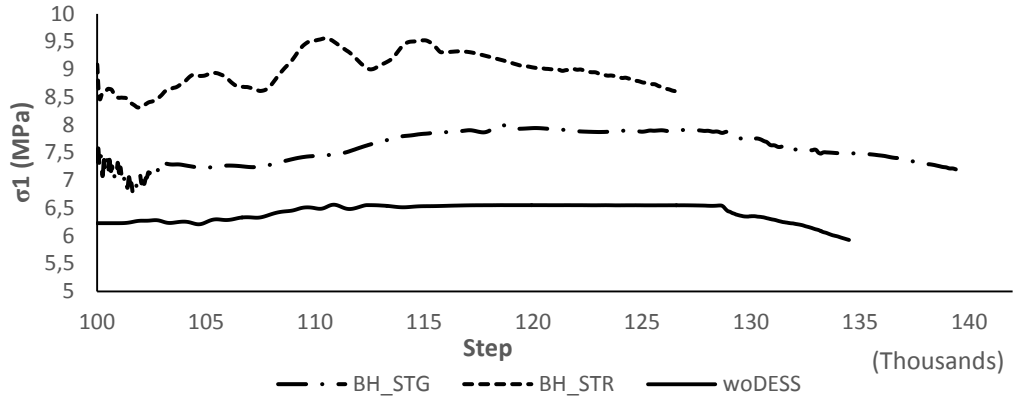

Figure 5.11 Comparison of σ_1 history in the upper stiff layer (T3) for no destressing and destressing in T3 layer with borehole patterns

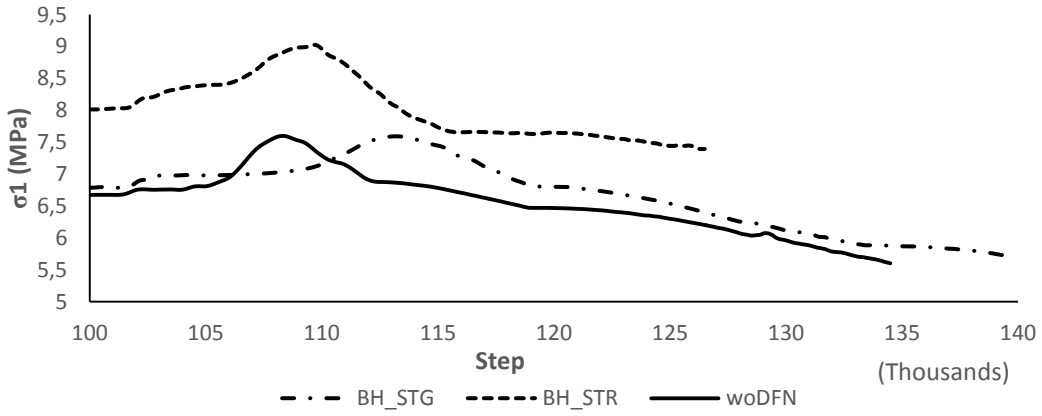

Figure 5.12 Comparison of σ_1 history in the lower stiff layer (T4) for no destressing and destressing in T3 layer with borehole patterns

The variation of the stress distribution after the first production stage was given in Figure 5.13. It can be seen that a higher stress concentration was observed right below the destressed zone with the BH_STR pattern.

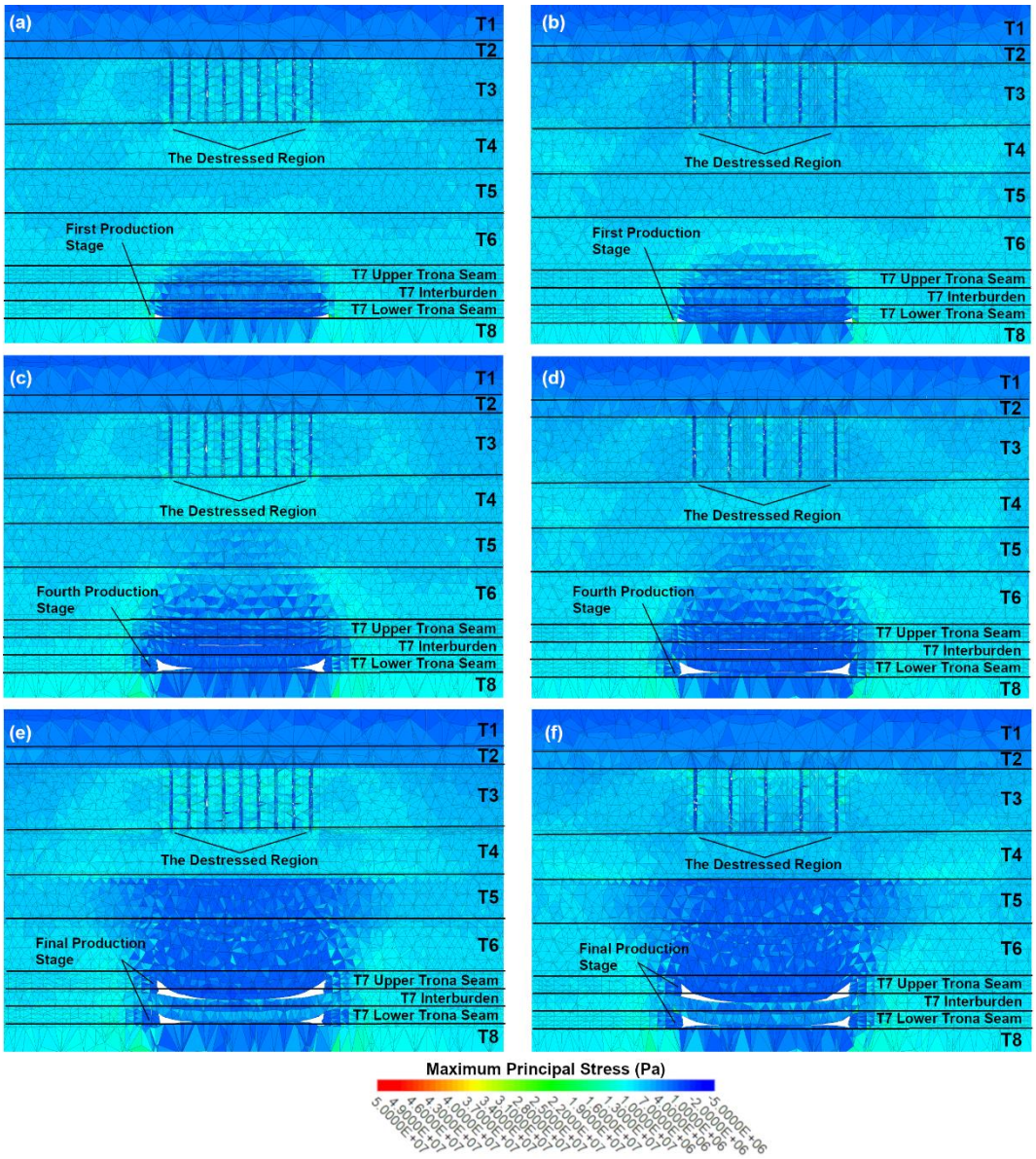

Figure 5.13 Stress distributions when BH_STR applied and after (a) the first production stage, (c) completing production in the lower seam, (e) producing both the upper and lower seams; when BH_STG applied and after (b) the first production stage, (d) completing production in the lower seam, (f) producing both the upper and lower seams

The yield in the rock mass can be observed from the Figure 5.14.a and Figure 5.14.b after the first production stage, from the Figure 5.14.c and Figure 5.14.d after the upper trona seam is produced, and from the Figure 5.14.e and Figure 5.14.f after the whole deposit is exploited. The caving due to production results in plastic

deformations above the cavern. The tensile yielding goes on during the production and terminates with the failure of the overburden.

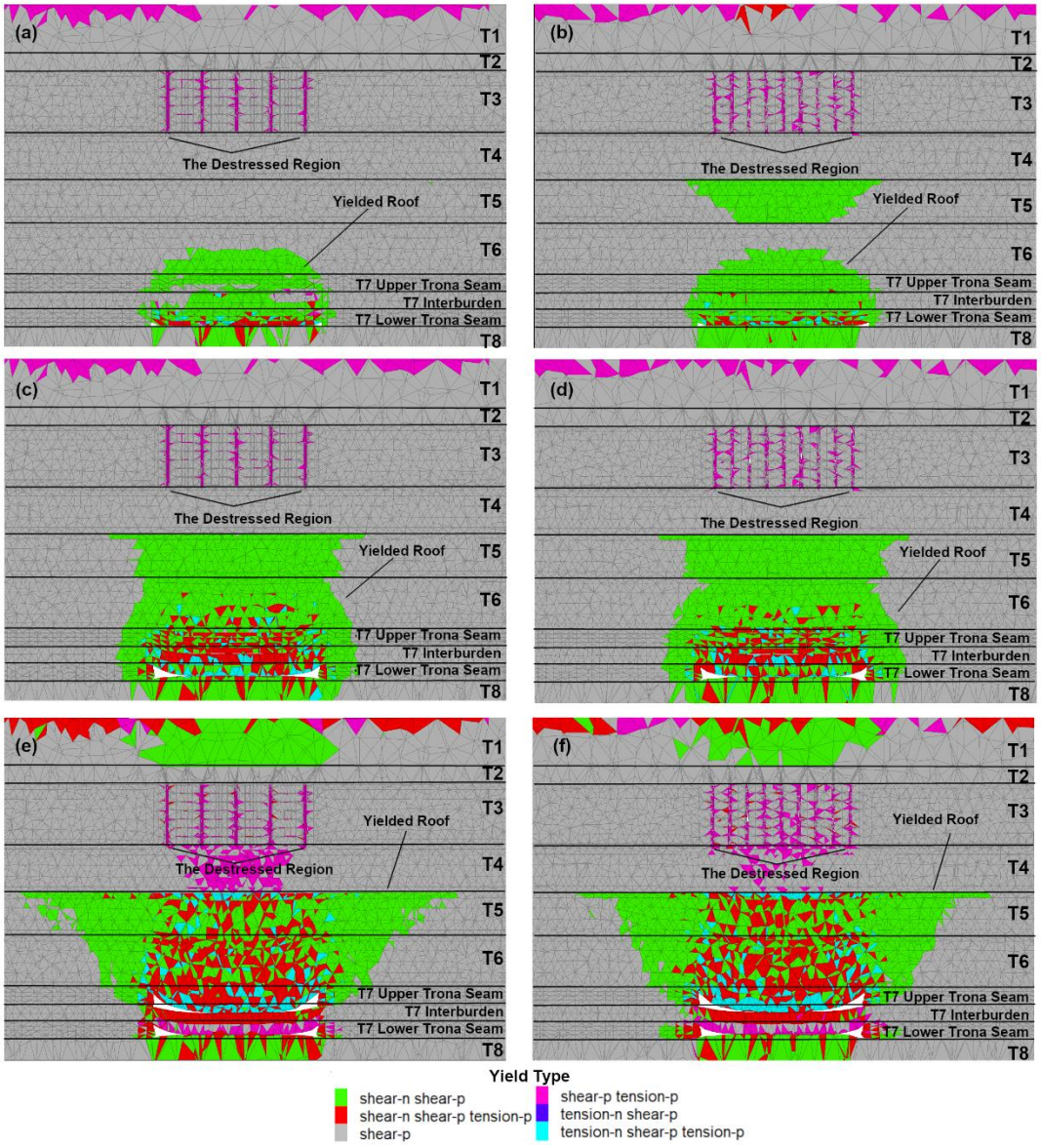

Figure 5.14 The yielded elements when BH_STG applied and after (a) the first production stage, (c) completing production in the lower seam, (e) producing both the upper and lower seams; when BH_STR applied and after (b) the first production stage , (d) completing production in the lower seam, (f) producing both the upper and lower seams

To conclude, both of the BH_STG and BH_STR patterns were proven to be useful for destressing. 22% and 46% increase in the stress between the destressed regions

is the proof of that the fractures created in a limited region propagate through the rest of the rock mass. Although BH_STR shows a higher stress accumulation, BH_STG pattern also works. By considering the operational efficiency the BH_STG pattern can be concluded to be more suitable for destressing.

5.3 Selection of the Best Pattern in the Upper Stiff Layer (T3)

Based on the simulations, the best decisions for destressing in the upper stiff layer (T3) are RN_60 for the ribbon pattern and BH_STG for the borehole pattern. Both economical and practical considerations were taken into account while making the decision. Further, RN_60 and BH_STG patterns were compared (Figure 5.15 and Figure 5.16) to see the best method for the elimination of sudden collapse risk. Data obtained from the same history points show that BH_STG has superiority over RN_60 case by 90% more stress increase in upper stiff layer (T3). The maximum principal stresses are 7.2 MPa for RN_60 and 8 MPa for BH_STG cases with respect to 6.6 MPa in woDESS case. Although both provide stress increase (10% RN_60, 22% BH_STG), considering the operational advantages, the amount of time, and the expenses BH_STG pattern is a better option.

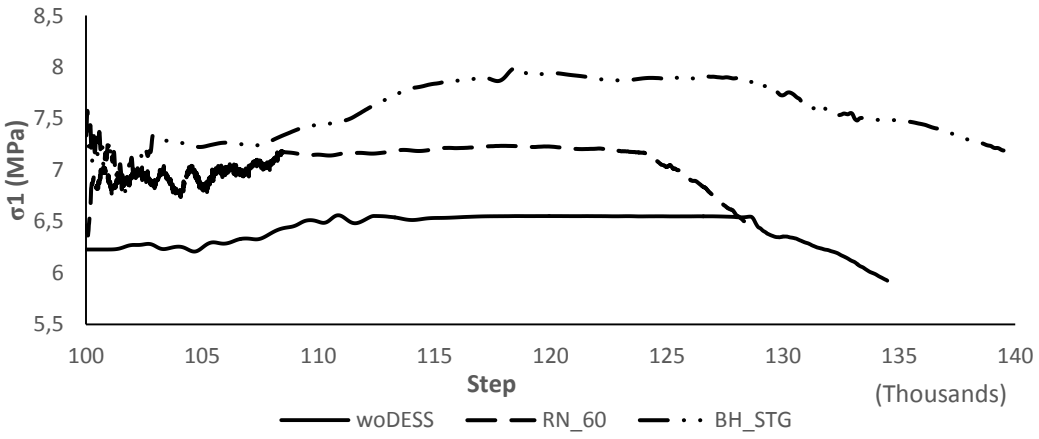

Figure 5.15 Comparison of σ_1 history in T3 layer when no destressing is induced and T3 layer is fractured using RN_60 and BH_STG patterns

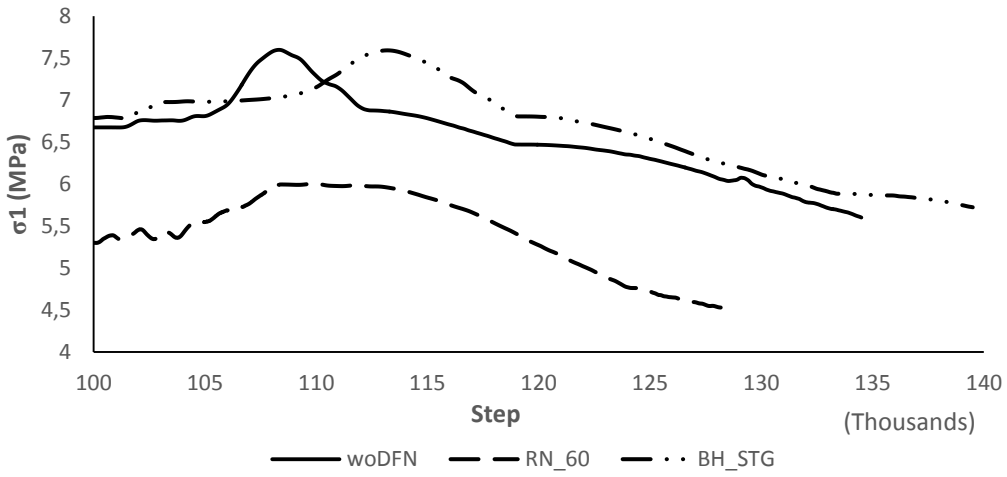

Figure 5.16 σ_1 histories in T4 layer for RN_60, BH_STG, and woDESS models

To sum up, in the stiffest and thickest T3 layer to perform destressing operation, drilling boreholes in a staggered pattern is the most viable option for destressing. Both mechanical and practical advantages lead to this choice. BH_STG is the best option when comparing the BH_STR and other RN patterns in T3.

5.4 Assessment of Destressing in the Upper (T3) and the Lower (T4) Stiff Strata

Besides the effects of shape, size, spacing, and patterns, the effect of destressed layer was also studied. Considering two distinct stratums with stiff mechanical characteristics share a thick span on the stratigraphy, it would be of concern to see the best layer to perform the destressing operation. For simulations, the best practice for both of the patterns were used. Similar to the destressing in upper stiff stratum (T3), BH_STG and RN_60 patterns were implemented to the lower stiff stratum (T4). The pattern dimensions were adjusted regarding the thickness of the T4 layer while the horizontal plane dimensions were identical. The similar DFN model and joint properties were used.

Investigating the σ_1 history in the upper stiff layer (T3) (Figure 5.17) for RN_60 pattern when the layer was destressed, σ_1 values increase by 10%. This was due to the stress transfer from the weakened zone to the unweakened zone as explained before. However, if the destressing operation was conducted on lower stiff layer (T4), it was seen that σ_1 values in the upper stiff layer (T3) decreases by 8%. In the lower stiff layer (T4), it can be observed that 21% relaxation occurs with the implementation of DFN into the upper stiff layer (T3) but fracturing the lower stiff layer (T4) shows a 3% stress increase. This tendency is similar to T3 σ_1 values when DFN implemented. However, in the former case the stress increase was 10% with respect to the 3%. The results show that both cases are acceptable since the strata fails in a controlled manner in either of the cases.

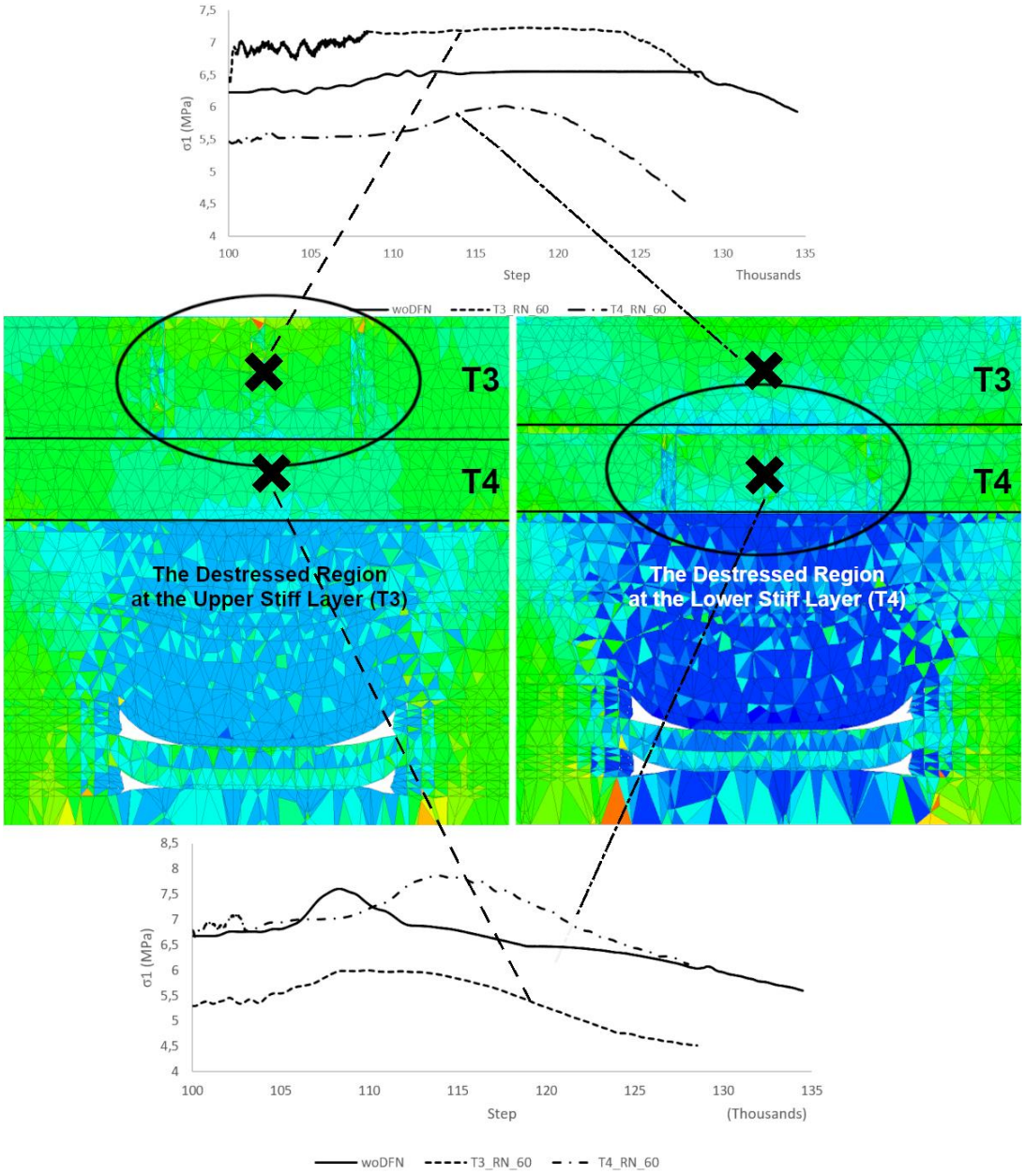

Figure 5.17 The major principal stresses in T3 and T4 layers for destressing with T3_RN_60 (left) and T4_RN_60 patterns (right)

For BH_STG pattern, destressing the upper stiff layer (T3) shows a 22% increase in the stress of T3; however, it is a 7% reduction when the lower stiff layer (T4) is destressed (Figure 5.18). These outcomes are compatible with the RN patterns as implementation of destressing into the layer results in higher stress levels in the

respective layer and lower stress levels in the other layer. However, σ_1 as a result of destressing the lower stiff layer (T4) shows 2% relaxation when BH_STG is conducted in T4 and no significant σ_1 change is observed in T3. In Figure 5.19, it can be seen that in both of the cases again the failure is observed, which refers to the success of the destressing operation. The difference between σ_1 decrease in RN and BH patterns can be explained by the geometry and size of the weakened volume. Naturally in RN patterns the stress decline is sharper than BH patterns but both patterns are successful in preventing the sudden collapse risk. According to the failure pattern, for deep deposits it would be logical to conduct destressing operation within the stiffer and thicker layers such as it is done in the upper stiff layer (T3) in this case. By increasing the stress accumulation in the unweakened zone, the failure of the strata is ensured.

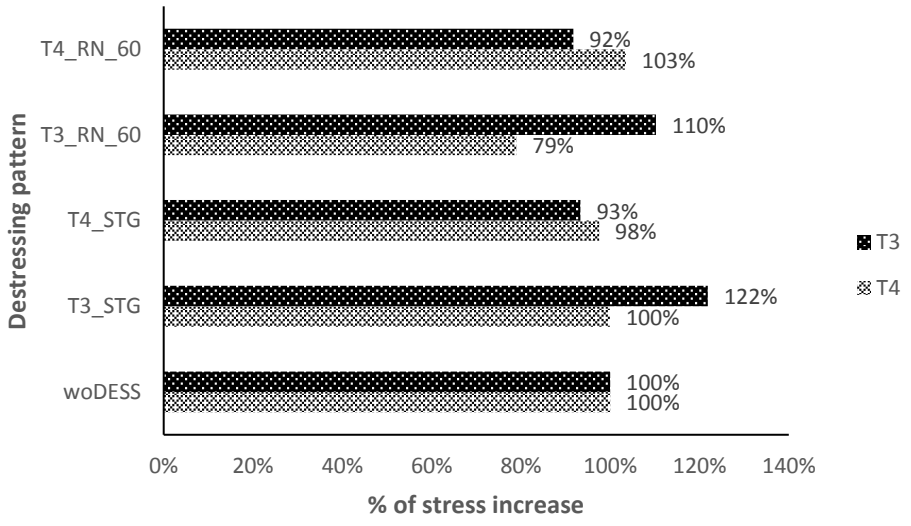

Figure 5.18 Percentage of major principal stress changes in the upper stiff layer (T3) and lower stiff layer (T4) regarding the destressing pattern and the strata

In the case of shallow deposits destressing less stiff and thinner strata would work as like in this study. Layers T6 and T5 cave almost immediately after removing trona layers where T3 and T4 start to accumulate stresses. Destressing in the relatively weak layer prevents this accumulation by providing failure of the strata.

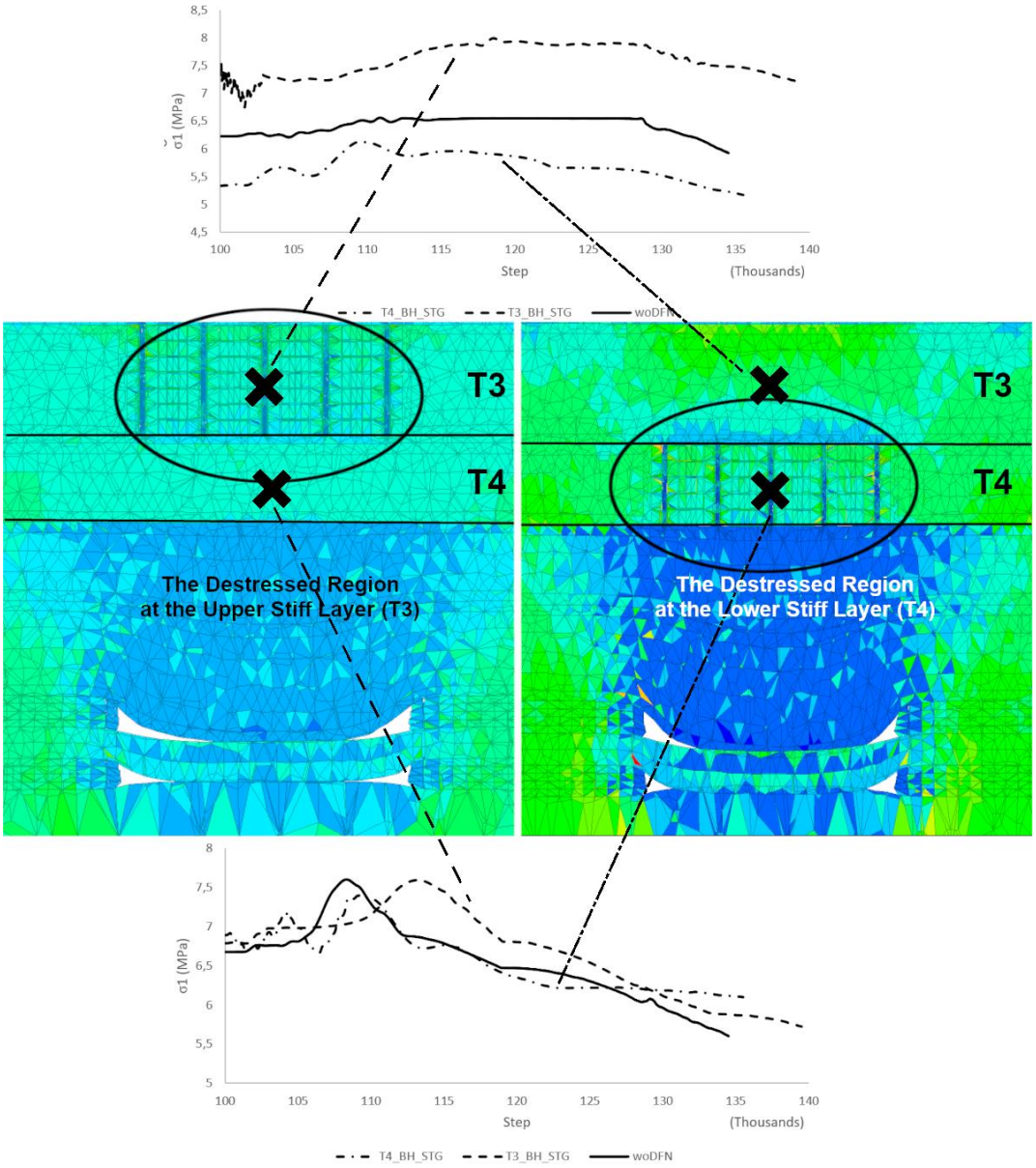

Figure 5.19 σ_1 values for T3 and T4 layer for T3_BH_STG (left) and T4_BH_STG (right)

CHAPTER 6

CONCLUSION

In conclusion, solution mining is an advantageous method for trona extraction due to its simplicity, safety, and low cost. However, challenges related to strata geomechanics, specifically the risk of sudden collapse in stiff layers, need to be addressed. This research focused on investigating mitigation methods through numerical simulations.

The study determined geomechanical parameters of trona rock mass and identified the stiff layers. Various destressing schemes were explored to manage stress in a hypothetical trona deposit with thick interburden. Elastoplastic material behavior was simulated using a strain-softening model. The propagation of stresses, vertical displacement, and abutment pressures around the cavern during production stages and after destressing were tracked.

Key findings include:

- Sequential removal of trona layers led to stress accumulation on stiff layers, particularly T3 and T4. Significant vertical displacements were observed on the roof of the cavern in T5 and T6 layers after complete extraction of trona seams.
- Asynchronous settling of stiff layers can result in roof collapse and premature loss of the cavern before the completion of the production.
- Abutment pressures increased significantly at the cavern wall, increasing the risk of pillar failure. Proper destressing and abutment stress management are crucial for operational sustainability.
- Implementing Discrete Fracture Networks (DFN) in the upper stiff layer (T3) reduced stress concentration by 24% and facilitated controlled failure of overburden strata.

- Two destressing patterns, ribbon and borehole, were compared for operational and economic concerns. The ribbon pattern with a spacing of 60 m demonstrated the most effective stress reduction, while the borehole pattern with staggered locations was deemed more practical.
- When considering multiple stiff layers, destressing T3 using RN_60 leads to a 10% increase in σ_1, while destressing T4 results in an 8% decrease in σ_1 in T3. Implementing DFN in T3 causes a 21% relaxation in T4, while fracturing T4 leads to a 3% stress increase.
- For the BH_STG pattern, destressing T3 results in a 22% stress increase in T3 and destressing T4 leads to a 7% stress reduction in T3, with a 2% relaxation in σ1 in T4.
- Both destressing patterns effectively prevent sudden collapse risks, with deep deposits benefiting from destressing stiffer and thicker layers (T3) and shallow deposits benefitting from destressing less stiff and thinner strata (T4)

Future research opportunities identified in the study include:

- Multi-cavern interactions: Investigating the interactions between multiple caverns to understand the destressing process more comprehensively.
- Advanced numerical methods: Exploring GPU-accelerated numerical methods to improve computational performance and utilizing advanced constitutive models for more realistic mechanical response. Coupled simulations of hydromechanical or thermomechanical models can investigate multi-physical effects.
- Field-scale investigations: Utilizing field monitoring data to validate numerical models and enhance their accuracy.

In conclusion, future studies should focus on complex scenarios, employ advanced numerical methods, and validate simulations through field-scale investigations. These efforts will contribute to enhancing operational safety, reducing geomechanical risks, and ensuring sustainable operation of solution mining.

REFERENCES

Abreu, J. F., Costa, A. M., Costa, P. V. M., Miranda, A. C. O., Zheng, Z., Wang, P., Goulart, M. B. R., Bergsten, A., Ebecken, N. F. F., Bittencourt, C. H., Assi, G., Meneghini, J. R., & Nishimoto, K. (2023). Large-scale storage of hydrogen in salt caverns for carbon footprint reduction. *International Journal of Hydrogen Energy*. https://doi.org/10.1016/j.ijhydene.2022.12.272

Adler, L., & Thompson, S. D. (2011). Mining Methods Classification System. In P. Darling (Ed.), *Mining Engineering Handbook* (3rd ed., pp. 349–355). Society for Mining, Metallurgy, and Exploration.

Aristotle. (350 B.C..). *Meteorology*.

Atluri, S. N., Kim, H.-G., & Cho, J. Y. (1999). A Critical Assessment of the Truly Meshless Local Petrov-Galerkin (MLPG), and Local Boundary Integral Equation (LBIE) Methods. *Computational Mechanics, 24*, 348–372.

Atluri, S. N., & Zhu, T. (1998). A new Meshless Local Petrov-Galerkin (MLPG) approach in computational mechanics. *Computational Mechanics, 22*, 117–127.

Aydan, Ö., & Ulusay, R. (2013). Geomechanical evaluation of derinkuyu antique underground city and its implications in geoengineering. *Rock Mechanics and Rock Engineering*, *46*(4), 731–754. https://doi.org/10.1007/s00603-012-0301-7

Aydan, Ö., Ulusay, R., & Tokashiki, N. (2014). A new rock mass quality rating system: Rock Mass Quality Rating (RMQR) and its application to the estimation of geomechanical characteristics of rock masses. *Rock Mechanics and Rock Engineering*, *47*(4), 1255–1276. https://doi.org/10.1007/s00603-013-0462-z

Aydın, Y., & Şenkal, S. S. (2001). Beypazarı Trona Yatağı'nı İşletmeye Alma Çalışmaları. In E. Ünal, B. Ünver, & B. Ünver (Eds.), *Türkiye 17.*

Uluslararası Madencilik Kongresi: Türkçe Bildiriler Kitabı (pp. 57–65). TMMOB.

Barton, N. (2002). Some new Q-value correlations to assist in site characterization and tunnel design. *Int. J. Rock Mech. & Min. Sci.*, *39*(2), 185–216.

Barton, N., & Bar, N. (2015). Introducing the Q-slope method and its intended use within civil and mining engineering projects. In Schubert & Kluckner (Ed.), *EUROCK 2015 & 64th Geomechanics Colloquium* (pp. 157–162).

Barton, N. R., Lien, R., & Lunde, J. (1974). Engineering Classification of Rock Masses for the Design of Tunnel Support. In *Rock Mechanics* (Vol. 6, pp. 189–236). Springer-Verlag. https://doi.org/https://doi.org/10.1007/BF01239496

Bawden, W. F. (2011). Ground Control Using Cable and Rock Bolting. In P. Darling (Ed.), *Mining Engineering Handbook* (pp. 611–625). Society for Mining, Metallurgy, and Exploration, Inc.

Begg, W. R., & Pohrivcak, N. A. (1998). Mining Methodology and Description: The Immel Mine. In W. A. Hustrulid & R. L. Bullock (Eds.), *Underground Mining Methods: Engineering Fundamentals and International Case Studies* (pp. 83–89). Society for Mining, Metallurgy, and Exploration, Inc.

Belytschko, T., Krongauz, Y., Organ, D., Fleming, M., & Krysl, I. (1996). Meshless Methods: An Overview and Recent Developments. *Comput. Methods Appl. Mech. Engrg*, *139*, 3–47.

Belytschko, T., Lu, Y. Y., & Gu, L. (1994). Element-Free Galerkin Methods. *INTERNATIONAL JOURNAL FOR NUMERICAL METHODS IN ENGINEERING*, *37*, 229–256.

Bessinger, S. L. (2011). Longwall Mining. In P. Darling (Ed.), *Mining Engineering Handbook* (3rd ed., pp. 1399–1415). Society for Mining, Metallurgy, and Exploration, Inc.

Bieniawski, Z. T. (1973). Engineering Classification of Jointed Rock Masses. In *Transaction of the South African Institution of Civil Engineers* (Vol. 14, pp. 335–344). South African Institution of Civil Engineers.

Bieniawski, Z. T. (1989). *Engineering Rock Mass Classifications A Complete Manual for Engineers and Geologists in Mining, Civil, and Petroleum Engineering*. John Wiley & Sons, Inc.

Bieniawski, Z. T. (1992). Ground Control. In H. L. Hartman (Ed.), *Mining Engineering Handbook* (2nd ed., Vol. 1, pp. 897–937). SME.

Boshkov, S. H., & Wright, F. D. (1973). Underground Mining Systems and Equipments. In A. B. Cummins & I. A. Given (Eds.), *Mining Engineering Handbook*. SME-AIME.

Buczkowski, R., & Kleiber, M. (1997). Elasto-Plastic Interface Model for 3D Frictional Orthotropic Contact Problems. *INTERNATIONAL JOURNAL FOR NUMERICAL METHODS IN ENGINEERING*, *40*, 599–619.

Bullock, R. L. (1998). Room-and-Pillar Method of Open-Stope Mining. In R. E. Gertsch & R. L. Bullock (Eds.), *Techniques in Underground Mining: Selections from Underground Mining Methods Handbook* (pp. 159–170). Society for Mining, Metallurgy, and Exploration, Inc.

Bullock, R. L. (2011). Room-and-Pillar Mining in Hard Rock. In P. Darling (Ed.), *Mining Engineering Handbook* (3rd ed., pp. 1327–1338). Society for Mining, Metallurgy, and Exploration.

Carmack, J., Dunn, B., Flach, M., & Sutton, G. (1998). The Viburnum Trend Underground - An Overview. In *Underground Mining Methods: Engineering Fundamentals and International Case Studies* (pp. 89–95). Society for Mining, Metallurgy, and Exploration, Inc.

Carter, P. R. (2001). Mining Practice for Intermediate-Depth, Narrow Tabular Ore Bodies with Particular Reference to the Free State and Klerksdorp Goldfields.

In W. A. Hustrulid & R. L. Bullock (Eds.), *Underground Mining Methods Engineering Fundamentals and International Case Studies* (pp. 165–178). Society for Mining, Metallurgy, and Exploration, Inc.

Çelik, A., & Özçelik, Y. (2021). Investigation of the efficiency of longwall top coal caving method applied by forming a face in horizontal thickness of the seam in steeply inclined thick coal seams by using a physical model. *International Journal of Rock Mechanics and Mining Sciences, 148*. https://doi.org/10.1016/j.ijrmms.2021.104917

Chamberlin, P. D. (2009). In Situ Leaching. In R. L. Lowrie (Ed.), *Mining Reference Handbook* (pp. 379–382). Society for Mining, Metallurgy, and Exploration, Inc.

Chen, D., Sun, C., & Wang, L. (2021). Collapse behavior and control of hard roofs in steeply inclined coal seams. *Bulletin of Engineering Geology and the Environment*, *80*(2), 1489–1505. https://doi.org/10.1007/s10064-020-02014-3

Chen, J.-S., Liu, W. K., Hillman, M. C., Chi, S.-W., Lian, Y., & Bessa, M. A. (2017). Reproducing Kernel Particle Method for Solving Partial Differential Equations. In *Encyclopedia of Computational Mechanics Second Edition* (pp. 1–44). John Wiley & Sons, Ltd. https://doi.org/10.1002/9781119176817.ecm2104

Cho, N., Martin, C. D., & Sego, D. C. (2007). A clumped particle model for rock. *International Journal of Rock Mechanics and Mining Sciences*, *44*(7), 997–1010. https://doi.org/10.1016/j.ijrmms.2007.02.002

Choi, D. S., & Dahl, H. D. (1981). Measurement and Prediction of Mine Subsidence Over Room-And-Pillar in Three Dimensions. In S. Peng (Ed.), *Workshop on Surface Subsidence Due to Underground Mining* (pp. 34–47). West Virginia University.

Chou, Q., Altosaar, A., & Gillen, K. (2016). Predicting Clearwater Formation Natural Fracture Intensity, Athabasca Oil Sans Area. In *Phys. Research: Solid Earth* (Vol. 50). American Geophysical Union.

Coates, D. F. (1981). *Rock Mechanics Principles*. Canada Centre for Mineral and Energy Technology.

Contrucci, I., Klein, E., Cao, N. T., Daupley, X., & Bigarré, P. (2011). Multi-parameter monitoring of a solution mining cavern collapse: First insight of precursors. *Comptes Rendus - Geoscience*, *343*(1), 1–10. https://doi.org/10.1016/j.crte.2010.10.007

Corkum, A. G., & Board, M. P. (2016). Numerical analysis of longwall mining layout for a Wyoming Trona mine. *International Journal of Rock Mechanics and Mining Sciences*, *89*, 94–108. https://doi.org/10.1016/j.ijrmms.2016.09.001

Cosar, S. (2004). *Application Of Rock Mass Classification Systems for Future Support Design of The Dim Tunnel Near Alanya*.

Coulomb, C. A. (1776). Essai sur une application des regles de maximis et minimis a quelques problemes de statique, relatifs a l'architecture. In *Memoires de Mathematique & de Physique 7* (pp. 343–382).

Cundall, P. A. (1971). A Computer Model for Simulating Progressive Large Scale Movements in Blocky Rock Systems. *Symposium of the International Society of Rock Mechanics*, II–8.

Cundall, P. A., & Hart, R. D. (1992). Numerical modelling of discontinua. *Engineering Computations*, *9*(2), 101–113. https://doi.org/10.1108/eb023851

Cyran, K., Kowalski, M., & Wilkosz, P. (2019). *GEOMECHANICAL PERFORMANCE OF THE SALT CAVERNS IN A LONG TERM STABILITY ANALYSIS*. www.solutionmining.org

Daupley, X., Cuche, H., & Ghoreychi, M. (2005). *Typology of Strata Movement Related to Old Solution Mining of Salt at Sarralbe (Lorraine, France)*.

Deere, D. U., Hendron, A. J., Patton, F. D., & Cording, E. J. (1967). Design of Surface and Near Surface Construction in Rock. *8th U.S. Symposium on Rock Mechanics: Failure and Breakage of Rock*, 237–302.

Dershowitz, W. S., & Herda, H. H. (1992). Interpretation of Fracture Spacing and Intensity. In Tillerson & Wawersik (Eds.), *The 33rd U.S. Symposium on Rock Mechanics (USRMS)* (pp. 757–766). Balkema.

Dowding, C. H., & Andersson, C.-A. (1986). Potential for Rock Bursting and Slabbing in Deep Caverns. *Engineering Geology*, *22*, 265–279.

Duarte, A., & Tinsley Odent, J. (1996). H-p Clouds- an h-p Meshless Method. In *Numerical Methods for Partial Differential Equations* (Vol. 12, pp. 673–705). John Wiley & Sons, Inc.

Einaudi, M. T. (2000). Mineral Resources: Assets and Liabilities. In *Earth systems – Processes and Issues* (Ernst WG). Cambridge University Press.

Einstein, H. H., & Baccher, G. B. (1983). Probabilistic and Statistical Methods in Engineering Geology Specific Methods and Examples Part I: Exploration. *Rock Mechanics and Rock Engineering*, *16*, 39–72.

Eros, J. M., & Candelario-Quintana, L. (2006). *Mineral Facilities of Africa and the Middle East*. USGS. https://pubs.usgs.gov/of/2006/1135/

Eti Soda. (2020). *What is Soda Ash*. https://www.etisoda.com/en/what-is-soda-ash/

Evans, A. M. (1993). *Ore Geology and Industrial Minerals: An Introduction* (3rd ed.). Blackwell Publishing.

Farahmand, K., Vazaios, I., Diederichs, M. S., & Vlachopoulos, N. (2015). *Generation of a Synthetic Rock Mass (SRM) Model for Simulation of Strength of Crystalline Rock using a Hybrid DFN- DEM Approach*. OnePetro.

http://onepetro.org/ISRMEUROCK/proceedings-pdf/EUROCK15/All-EUROCK15/ISRM-EUROCK-2015-135/1469434/isrm-eurock-2015-135.pdf

Farmer, I. (1992). Room and Pillar Mining. In H. L. Hartman (Ed.), *Mining Engineering Handbook* (pp. 1681–1686). SME.

Fortney, S. J. (1998). Advanced Mine-Wide Automation in Potash. In R. L. Bullock & W. A. Hustrulid (Eds.), *Underground Mining Methods: Engineering Fundamentals and International Case Studies* (pp. 143–148). Society for Mining, Metallurgy, and Exploration, Inc.

Fuenkajorn, K., & Archeeploha, S. (2011). Estimation of cavern configurations from subsidence data. *Bulletin of Engineering Geology and the Environment*, *70*(1), 53–61. https://doi.org/10.1007/s10064-010-0269-z

Gandhi, S. M., & Sarkar, B. C. (2016). Mineral Deposits: Types and Associations. In *Essentials of Mineral Exploration and Evaluation* (pp. 23–52). Elsevier. https://doi.org/10.1016/b978-0-12-805329-4.00009-0

Gens, A., Carol, I., & Alonso, E. E. (1995). Rock Joints: FEM Implementation and Applications. In M. J. Boulon & A. P. S. Selvadurai (Eds.), *Mechanics of Geomaterial Interfaces* (pp. 133–151). Elsevier.

Ghaboussi, J., Wilson, E. L., & Isenberg, J. (1973). Finite element for rock joints and interfaces. *Journal of the Soil Mechanics and Foundations Division: Proceedings of the American Society of Civil Engineers*, *99*, 833–848.

Ghabraie, B., Ren, G., Smith, J., & Holden, L. (2015). Application of 3D laser scanner, optical transducers and digital image processing techniques in physical modelling of mining-related strata movement. *International Journal of Rock Mechanics and Mining Sciences*, *80*, 219–230. https://doi.org/10.1016/j.ijrmms.2015.09.025

Ghabraie, B., Ren, G., & Smith, J. V. (2017). Characterising the multi-seam subsidence due to varying mining configuration, insights from physical

modelling. *International Journal of Rock Mechanics and Mining Sciences*, *93*, 269–279. https://doi.org/10.1016/j.ijrmms.2017.02.001

Gingold, R. A., & Monaghan, J. J. (1977). Smoothed Particle Hydrodynamics: Theory and Application to Non-spherical Stars. *Mon. Not. R. Astr. Soc.*, *181*, 375–389.

Goodman, R. E., Taylor, R. L., & Brekke, T. L. (1968). A Model for the Mechanics of Jointed Rock. *Journal of the Soil Mechanics and Foundations Division*, *94*(3), 637–659.

Griffith, W. A., Sanz, P. F., & Pollard, D. D. (2009). Influence of outcrop scale fractures on the effective stiffness of fault damage zone rocks. *Pure and Applied Geophysics*, *166*(10–11), 1595–1627. https://doi.org/10.1007/s00024-009-0519-9

Grimstad, E., & Barton, N. (1993). Updating the Q-system for NMT. *International Symposium on Sprayed Concrete*, 46–66. https://www.researchgate.net/publication/312619292

Guo, Q., Ren, F., Guo, H., Zhao, L., & Yan, Z. (2013). Strain Sensors with Temperature Compensation Employed for Insitu Stress Monitor. In *TELKOMNIKA* (Vol. 11, Issue 11).

Habibi, R., Moomivand, H., Ahmadi, M., & Asgari, A. (2021). Stability analysis of complex behavior of salt cavern subjected to cyclic loading by laboratory measurement and numerical modeling using LOCAS (case study: Nasrabad gas storage salt cavern). *Environmental Earth Sciences*, *80*(8), 1–21. https://doi.org/10.1007/S12665-021-09620-8/FIGURES/20

Hadjigeorgiou, J., & Potvin, Y. (2011). Hard-Rock Ground Control with Steel Mesh and Shotcrete. In P. Darling (Ed.), *Mining Engineering Handbook* (pp. 573–594). Society for Mining, Metallurgy, and Exploration, Inc.

Hammah, R. E., Yacoub, T., Corkum, B., Wibowo, F., & Curran, J. H. (2007). Analysis of Blocky Rock Slopes with Finite Element Shear Strength Reduction Analysis. In E. Eberhardt, D. Stead, & T. Morrison (Eds.), *1st Canada-US Rock Mechanics Symposium* (pp. 329–334).

Hamrin, H. (1982). Choosing an Underground Mining Method. In W. A. Hustrulid (Ed.), *Underground Handbook.* AIME.

Hamrin, H. (1998). Choosing an Underground Mining Method. In R. E. Gertsch & R. L. Bullock (Eds.), *Techniques in Underground Mining: Selections from Underground Mining Methods Handbook* (pp. 45–85). Society for Mining, Metallurgy, and Exploration, Inc.

Hamrin, H. (2001). Underground Mining Methods and Application. In W. A. Hustrulid & R. L. Bullock (Eds.), *Underground Mining Methods: Engineering Fundamentals and International Case Studies* (pp. 3–14). Society for Mining, Metallurgy, and Exploration, Inc.

Hardy, M. P., & Agapito, J. F. T. (1977). Pillar Design in Underground Oil Shale Mines. *16th U.S. Symposium on Rock Mechanics*, 257–266. http://onepetro.org/ARMAUSRMS/proceedings-pdf/ARMA75/All-ARMA75/ARMA-75-257/2061740/arma-75-257.pdf/1

Hardy, M., Ramey, M., Yates, C., & Nielsen, K. (2003, February 24). *Solution Mining of Nahcolite at the American Soda Project, Piceance Creek, Colorado*.

Harrison, J. P. (2011). Mine Subsidence. In P. Darling (Ed.), *Mining Engineering Handbook* (pp. 627–644). Society for Mining, Metallurgy, and Exploration, Inc.

Harrison, J. P., & Hudson, J. A. (2000). *Engineering Rock Mechanics Part 2: Illustrative Worked Examples* (Vol. 2). Pergamon.

Hart, R. D. (1993). An Introduction to Distinct Element Modeling for Rock Engineering. In *Analysis and Design Methods Principles, Practice and Projects* (Vol. 2, pp. 245–261). Pergamon.

Hartman, H. L. (1987). *Introductory Mining Engineering*. Wiley.

Haynes, S. J. (1993). Vein-type Ore Deposits. In *Ore Geology Reviews* (Vol. 8).

He, M., Zhang, X., & Zhao, S. (2017). Directional Destress with Tension Blasting in Coal Mines. *Procedia Engineering*, *191*, 89–97. https://doi.org/10.1016/j.proeng.2017.05.158

Herne, V., & McGuire, T. (1998). Mississippi Potash, Inc.'s, Underground Operations. In W. A. Hustrulid & R. L. Bullock (Eds.), *Underground Mining Methods: Engineering Fundamentals and International Case Studies* (pp. 137–142). Society for Mining, Metallurgy, and Exploration, Inc.

Hoek, E. (1994). Strength of Rock and Rock Masses. *International Society of Rock Mechanics News Journal*, *2*(2), 4–16.

Hoek, E. (2007). *Practical Rock Engineering*.

Hoek, E., Carranza-Torres, C., & Corkum, B. (2002). Hoek-Brown Failure Criterion 2002 Edition. *NARMS-TAC Conference*, 267–273.

Hoek, E., Marinos, P., & Benissi, M. (1998). Applicability of the geological strength index (GSI) classification for very weak and sheared rock masses. The case of the Athens Schist Formation. In *Bull Eng Geol Env* (Vol. 57).

Hore-Lacy, I. (2004). Uranium Mining, Processing, and Enrichment. *Encyclopedia of Energy*, *6*, 317–328.

Hudson, J. A. (2001). Rock engineering case histories: key factors, mechanisms and problems. *Rock Mechanics a Challenge for Society ISRM Regional Symposium EUROC2001*, 13–20.

ISRM. (2007). *The Complete ISRM Suggested Methods for Rock Characterization, Testing and Monitoring: 1974-2006* (R. Ulusay & J. Hudson, Eds.). ISRM Turkish National Group & ISRM.

ISRM. (2014). *The ISRM Suggested Methods for Rock Characterization, Testing and Monitoring: 2007-2014* (R. Ulusay, Ed.). Springer.

ITASCA Consulting Group Inc. (1992). *UDEC Manual*.

ITASCA Consulting Group Inc. (1994). *3DEC Manual*.

ITASCA Consulting Group Inc. (1995). *PFC Manual*.

Itasca Consulting Group Inc. (2016). *3DEC User's Guide*.

Jacquemyn, C., Swennen, R., & Ronchi, P. (2012). Mechanical stratigraphy and (palaeo-) karstification of the Murge area (Apulia, Southern Italy). *Geological Society Special Publication, 370*(1), 169–186. https://doi.org/10.1144/SP370.4

Jameson, A. W., & Ackerman, G. R. (2001). Underground Mining at Impala Platinum, Ltd., in the Northwest Province of South Africa. In W. A. Hustrulid & R. L. Bullock (Eds.), *Underground Mining Methods Engineering Fundamentals and International Case Studies* (pp. 156–163). Society for Mining, Metallurgy, and Exploration, Inc.

Jing, L. (2003). A review of techniques, advances and outstanding issues in numerical modelling for rock mechanics and rock engineering. In *International Journal of Rock Mechanics and Mining Sciences* (Vol. 40, Issue 3, pp. 283–353). Elsevier BV. https://doi.org/10.1016/S1365-1609(03)00013-3

Jing, L., & Hudson, J. A. (2002). Numerical methods in rock mechanics. In *International Journal of Rock Mechanics & Mining Sciences* (Vol. 39).

Jing, L., & Stephansson, O. (2007). *Fundamentals of Discrete Element Methods for Rock Engineering* (1st ed.). Elsevier.

Katona, M. G. (1983). A Simple Contact-Friction Interface Element with Applications to Buried Culverts. *INTERNATIONAL JOURNAL FOR NUMERICAL AND ANALYTICAL METHODS IN GEOMECHANICS*, *7*, 371–384. https://doi.org/https://doi.org/10.1002/nag.1610070308

Kattenhorn, S. A., & Pollard, D. D. (2001). Integrating 3-D seismic data, field analogs, and mechanical models in the analysis of segmented normal faults in the Wytch Farm oil field, southern England, United Kingdom A U T H O R S. In *AAPG Bulletin*, *v* (Vol. 85, Issue 7).

Kazerani, T., & Zhao, J. (2010). Micromechanical parameters in bonded particle method for modelling of brittle material failure. *International Journal for Numerical and Analytical Methods in Geomechanics*, *34*(18), 1877–1895. https://doi.org/10.1002/nag.884

Konicek, P., Konecny, P., & Ptacek, J. (2011). Destress rock blasting as a rockburst control technique. In *Harmonising Rock Engineering and the Environment* (pp. 1221–1226). CRC Press. https://doi.org/10.1201/b11646-229

Konicek, P., & Schreiber. (2018). Rockburst prevention via destress blasting of competent roof rocks in hard coal longwall mining. *Journal of the Southern African Institute of Mining and Metallurgy*, *118*(3), 235–242. https://doi.org/10.17159/2411-9717/2018/v118n3a6

Korzeniowski, W., & Stankiewicz, A. (1998). Modifications of the Room-and-Pillar Mining Methods for Polish Copper Ore Deposits. In W. A. Hustrulid & R. L. Bullock (Eds.), *Underground Mining Methods: Engineering Fundamentals and International Case Studies* (pp. 103–111). Society for Mining, Metallurgy, and Exploration, Inc.

Kroon, I. C., Orlic, B., & Scheffers, B. C. (2003). *Abandonment of Solution Mined Salt Caverns in the Netherlands*. www.tno.nl

Kyle, J. I., Maxwell, D. K., & Alexander, B. L. (2011). In-Situ Techniques of Solution Mining. In P. Darling (Ed.), *Mining Engineering Handbook* (3rd ed., pp. 1103–1119). Society for Mining, Metallurgy, and Exploration, Inc.

Lane, W. L., Yanske, T. R., Clark, L. M., & Roberts, D. P. (1998). Pillar Extraction and Rock Mechanics at the Doe Run Company in Missouri 1991 to 2000. In W. A. Hustrulid & R. L. Bullock (Eds.), *Underground Mining Methods: Engineering Fundamentals and International Case Studies* (pp. 95–103). Society for Mining, Metallurgy, and Exploration, Inc.

Lei, Q., Latham, J. P., & Tsang, C. F. (2017). The use of discrete fracture networks for modelling coupled geomechanical and hydrological behaviour of fractured rocks. In *Computers and Geotechnics* (Vol. 85, pp. 151–176). Elsevier Ltd. https://doi.org/10.1016/j.compgeo.2016.12.024

Lemos, J. V. (1987). *A Hybrid Distinct Element Computational Model for the Half-Plane* [MSc]. University of Minnesota.

Li, H., Wanyan, Q., Ding, G., Li, K., Kou, Y., Bai, S., Ran, L., Wu, J., & Deng, J. (2022). Geomechanical Feasibility Analysis of Salt Cavern Gas Storage Construction in Sanshui Basin, Guangdong Province. *Eng*, *3*(4), 709–731. https://doi.org/10.3390/eng3040048

Liang, X., Ma, H., Li, P., Cai, R., Zhao, K., Li, H., Yu, H., & Yang, C. (2022). A prediction method of the effective volume in sediment-filled salt cavern. *Journal of Energy Storage*, *56*. https://doi.org/10.1016/j.est.2022.106026

Lishchuk, V., Lund, C., Lamberg, P., & Miroshnikova, E. (2018). Simulation of a mining value chain with a synthetic ore body model: Iron ore example. *Minerals*, *8*(11). https://doi.org/10.3390/min8110536

Lisjak, A., & Grasselli, G. (2014). A review of discrete modeling techniques for fracturing processes in discontinuous rock masses. In *Journal of Rock Mechanics and Geotechnical Engineering* (Vol. 6, Issue 4, pp. 301–314). Chinese Academy of Sciences. https://doi.org/10.1016/j.jrmge.2013.12.007

Liu, A., & Liu, S. (2021). A fully-coupled water-vapor flow and rock deformation/damage model for shale and coal: Its application for mine stability evaluation. *International Journal of Rock Mechanics and Mining Sciences*, *146*. https://doi.org/10.1016/j.ijrmms.2021.104880

Liu, W. K., Li, S., Belytschko, T., & Liu, W.-K. (1995). *Moving Least Square Reproducing Kernel Methods I Methodology and Convergence*.

Liu, W., Zhang, Z., Fan, J., Jiang, D., Li, Z., & Chen, J. (2020). Research on gas leakage and collapse in the cavern roof of underground natural gas storage in thinly bedded salt rocks. *Journal of Energy Storage*, *31*. https://doi.org/10.1016/j.est.2020.101669

Livingstone, P., Purcell, J., Morehouse, D., & Waugh, D. (1998). Mining at IMC Potash Carlsbad. In W. A. Hustrulid & R. L. Bullock (Eds.), *Underground Mining Methods: Engineering Fundamentals and International Case Studies* (pp. 131–136). Society for Mining, Metallurgy, and Exploration, Inc.

Long, J. C., Gilmour, P., & Witherspoon, P. A. (1985). A Model for Steady Fluid Flow in Random Three-Dimensional Networks of Disc-Shaped Fractures. In *WATER RESOURCES RESEARCH* (Vol. 21, Issue 8).

Long, J. C. S., Remer, J. S., Wilson, C. R., & Witherspoon, P. A. (1982). Porous Media Equivalents for Networks of Discontinuous Fractures. *WATER RESOURCES RESEARCH*, *18*(3), 645–658.

Lorig, L. J., & Brady, B. H. G. (1982). A Hybrid Discrete Element-Boundary Element Method of Stress Analysis. *The 23rd U.S Symposium on Rock Mechanics (USRMS)*, 628–636. http://onepetro.org/ARMAUSRMS/proceedings-pdf/ARMA82/All-ARMA82/ARMA-82-628/2048451/arma-82-628.pdf/1

Lutton, R. J., Banks, D. C., & Strohm Jr., W. E. (1978). Slides in Gaillard Cut, Panama Canal Zone. In Barry. Voight (Ed.), *Rockslides and Acalanches, 2* (pp. 151–224). Elsevier Scientific Pub. Co.

Ma, H., Wei, X., Shi, X., Liang, X., Bai, W., & Ge, L. (2022). Evaluation Methods of Salt Pillar Stability of Salt Cavern Energy Storage. In *Energies* (Vol. 15, Issue 20). MDPI. https://doi.org/10.3390/en15207570

MacDonald, A. J., & Singh, N. (2001). Extraction of a Wide Ore Body at Depth in the SV2/3 Area at Placer Dome Western Areas Joint Venture. In W. A. Hustrulid & R. L. Bullock (Eds.), *Underground Mining Methods Engineering Fundamentals and International Case Studies* (pp. 179–185). Society for Mining, Metallurgy, and Exploration, Inc.

Marco, A., Perez, G., & Abel Gonzalez, V. (1998). Underhand Room-and-Pillar Mining as Applied at the Aurora Mine Charcas Unit, Grupo Mexico. In W. A. Hustrulid & R. L. Bullock (Eds.), *Underground Mining Methods: Engineering Fundamentals and International Case Studies* (pp. 111–119). Society for Mining, Metallurgy, and Exploration, Inc.

Mark, C. (1999). Empirical Methods for Coal Pillar Design. *2nd International Workshop on Coal Pillar Mechanics and Design*, 145–154.

Martens, Chas. D. & Assoc. (1972). *Underground Mining*. Joy Manufacturing Co.

Melenk, J. M., & Babuska, I. (1996). The partition of unity finite element method: Basic theory and applications. *Comput. Methods Appl. Mech. Engrg*, *139*, 289–314.

Miao, S., Konicek, P., Pan, P. Z., & Mitri, H. (2022). Numerical Modelling of Destress Blasting e A State-of-the-Art Review. *Journal of Sustainable Mining*, *21*(4), 278–297. https://doi.org/10.46873/2300-3960.1366

Mining Intelligence. (2014). *Mining Intelligence - Properties Overview Report*. https://data.miningintelligence.com:443/property/browsesearch.aspx?pg=2&st=LastUpdatedAsc&wttest=Mine%7cMine+Complex&ploc=Turkey

Minkley, W., & Lüdeling, C. (2015, June). Longwall Caving in Potash Mining-Geomechanical Assessment of Damage and Barrier Integrity. *ARMA 16-407* .

http://onepetro.org/ARMAUSRMS/proceedings-pdf/ARMA16/All-ARMA16/ARMA-2016-407/1328670/arma-2016-407.pdf/1

Momoh, O. A., Mitri, H. S., & Rizkalla, M. (1996). Numerical Modelling of Destress Blasting. In M. Aubertin, F. Hassani, & H. Mitri (Eds.), *2nd North American Rock Mechanics Symposium: NARMS '96* (pp. 1911–1918). A.A. Balkema.

Moradi, G., Bonab, H., & Abbasnejad, A. (2015). Experimental Modeling and Measuring Stresses and Strains during Arching Phenomenon. *Geosciences*, *2015*(2), 53–61. https://doi.org/10.5923/j.geo.20150502.01

Morgan, J. L., Snider-Lord, A. C., & Ambs, D. C. (2018, June 18). InSAR for Monitoring Cavern Integrity: 2D Surface Movement over Bryan Mound. *SMRI Spring 2018 Technical Conference*. www.solutionmining.org

Morrison, R. G. K. (1976). *A Philosophy of Ground Control: A Bridge Between Theory and Practice*. McGill University, Department of Mineralogy, Metallurgy, and Engineering.

Müller, C., Frühwirt, T., Haase, D., Schlegel, R., & Konietzky, H. (2018). Modeling deformation and damage of rock salt using the discrete element method. *International Journal of Rock Mechanics and Mining Sciences*, *103*, 230–241. https://doi.org/10.1016/j.ijrmms.2018.01.022

Munjiza, A. (2004). *The Combined Finite-Discrete Element Method*. John Wiley & Sons Ltd.

Nayroles, B., Touzot, G., & Villon, P. (1992). Computational Mechanics Generalizing the finite element method: Diffuse approximation and diffuse elements. *Computational Mechanics*, *10*, 307–318.

Nelson, M. G. (1998). Underground Mining of Frozen Placers. In W. A. Hustrulid & R. L. Bullock (Eds.), *Underground Mining Methods: Engineering*

Fundamentals and International Case Studies (pp. 119–128). Society for Mining, Metallurgy, and Exploration, Inc.

Nelson, M. G. (2011). Evaluation of Mining Methods and Systems. In P. Darling (Ed.), *Mining Engineering Handbook* (3rd ed., pp. 341–348). Society for Mining, Metallurgy, and Exploration .

Nielsen, K. R., Cirotski, L. G., & Turner, A. L. (2004). *Sodium Bicarbonate Production from Nahcolite* (Patent No. 2004/0231109A1).

Nieto, A. (2011). Selection Process for Underground Soft-Rock Mining. In P. Darling (Ed.), *Mining Engineering Handbook* (3rd ed., pp. 377–384). Society for Mining, Metallurgy, and Exploration, Inc. (SME).

Osborne, S. E. (2020). *2015 Minerals Yearbook Mining and Quarrying Trends (Advance Release)*. https://doi.org/10.3133/pp1802a

Özfırat, M. K., Şimşir, F., & Gönen, A. (2005). A Brief Comparison of Longwall Methods Used at Mining of Thick Coal Seams. *The 19th International Mining Congress and Fair of Turkey, İMCET2005*.

Pan, X. D., & Reed, M. B. (1991). A Coupled Distinct Element-Finite Element Method for Large Deformation Analysis of Rock Masses. *Int J Rock Mech Min Sci Geomech*, *28*(1), 93–99.

Paulick, P. R. (1963). *Atlas of Mining Methods* (Vol. 1). Verlagsdruckerre.

Pechmann, J. C., Walter, W. R., Nava, S. J., & Arabasz, W. J. (1995). Seismic Event in the Trona Mining District of Southwestern Wyoming. *Seismological Research Letters*, *66*(3), 25–34. http://pubs.geoscienceworld.org/ssa/srl/article-pdf/66/3/25/2753294/srl066003_0025.pdf

Peng, S. S. (1978). *Coal Mine Ground Control*. John Wiley & Sons, Inc.

Peng, S. S. (2006). *Longwall Mining* (2nd ed.). West Virginia University, College of Mineral and Energy Resources.

Peng, S. S., & Chiang, H. S. (1984). *Longwall Mining*. John Wiley & Sons, Inc.

Phillip, J. D., & Vandendoren, A. (2006). *Opløsningsbrydning af malm, som indeholder natriumcarbonat og -bicarbonate* (Patent No. DK2607313T3). SOLVAY.

Pike, R. D. (1943). *Solution Mining of Trona* (Patent No. 2,388,009).

Popov, G. (1971). *The Working of Mineral Deposits of Mineral Deposits*. Mir Publishers.

Qin, Y., Xu, N., Zhang, Z., & Zhang, B. (2021). Failure Process of Rock Strata Due to Multi-seam Coal Mining: Insights from Physical Modelling. *Rock Mechanics and Rock Engineering*, *54*(5), 2219–2232. https://doi.org/10.1007/s00603-021-02415-0

Ram Saharan, M. (2010). Numerical Modelling Investigations to Study Effect of Geotechnical and Explosive Properties in Limiting Rock Fracturing Due to Blasting in Deep Mining Roadways. *ISRM International Symposium 2010 & 6thAsian Rock Mechanics Symposium*, 23–27. http://onepetro.org/ISRMARMS/proceedings-pdf/ARMS610/All-ARMS610/ISRM-ARMS6-2010-136/1715867/isrm-arms6-2010-136.pdf/1

Riahi, A., Hammah, E. R., & Curran, J. H. (2010, June). Limits of Applicability of the Finite Element Explicit Joint Model in the Analysis of Jointed Rock Problems. *44th US Rock Mechanics Symposium*. http://onepetro.org/ARMAUSRMS/proceedings-pdf/ARMA10/All-ARMA10/ARMA-10-336/1718520/arma-10-336.pdf/1

Ritter, W. (1879). *Die statik der tunnelgewölbe*. J. Springer.

Robb, L. (2005). *Introduction To Ore-Forming Process*. Blackwell Publishing.

Roberts, D. R. (1998). Closed-Circuit Mechanized Cut-and-Fill Mining at PCS New Brunswick Division. In W. A. Hustrulid & R. L. Bullock (Eds.), *Underground Mining Methods: Engineering Fundamentals and International Case Studies 119-128* (pp. 149–154). Society for Mining, Metallurgy, and Exploration, Inc.

Roux, A. J. A., Leeman, E. R., & Denkhaus, H. G. (1957). De-Stressing: A Means of Ameliorating Rockburst Conditions. *Journal of the South African Institute of Mining and Metallurgy*.

Salamon, M. D. G., & Munro, A. H. (1967). A Study of the Strength of Coal Pillars. *Journal of the South African Institute of Mining and Metallurgy*, *68*, 55–67.

Schlitt, W. J. (2011). Surface Techniques of Solution Mining. In P. Darling (Ed.), *Mining Engineering Handbook* (3rd ed., pp. 1087–1101). Society for Mining, Metallurgy, and Exploration, Inc.

Sharma, V. M., Saxena, K. R., & Woods, R. D. (Eds.). (1999). *Distinct Element Modelling in Geomechanics*. Balkema.

Shi, G. (1988). *Discontinous Deformation Analysis - A New Numerical Model for the Statistics, Dynamics of Block Systems* [PhD]. University of California.

Shi, G., & Goodman, R. E. (1985). Two Dimensional Discontinous Deformation Analysis. *INTERNATIONAL JOURNAL FOR NUMERICAL AND ANALYTICAL METHODS IN GEOMECHANICS*, *9*, 541–556.

Shi, J. Q., & Durucan, S. (2005). CO2 Storage in Caverns and Mines. Oil & Gas Science and Technology-Revue d'IFP Energies nouvelles. *Oil & Gas Science and Technology-Rev. IFP*, *60*(3), 569–571. https://doi.org/10.2516/ogst:2005039ï

Singh, G. S. P., & Singh, U. K. (2010). Prediction of caving behavior of strata and optimum rating of hydraulic powered support for longwall workings.

International Journal of Rock Mechanics and Mining Sciences, *47*(1), 1–16. https://doi.org/10.1016/j.ijrmms.2009.09.001

Sipahi, M. T., & Develi, K. (2021). *Modelling of Hydraulic Fracturing Treatments in South East Part of Turkey With DFN Method and Comparison With Simulation Results*. OnePetro. http://onepetro.org/ARMAUSRMS/proceedings-pdf/ARMA21/All-ARMA21/ARMA-2021-1213/2482037/arma-2021-1213.pdf

Stace, R. (2011). Soft-Rock Ground Control. In P. Darling (Ed.), *Mining Engineering Handbook* (pp. 595–610). Society for Mining, Metallurgy, and Exploration, Inc.

Stefanko, R. (1983). *Coal Mining Technology: Theory and Practice*. SME of the AIME.

Sturzenegger, M., & Stead, D. (2009). Close-range terrestrial digital photogrammetry and terrestrial laser scanning for discontinuity characterization on rock cuts. *Engineering Geology*, *106*(3–4), 163–182. https://doi.org/10.1016/j.enggeo.2009.03.004

Sun, Y., Zuo, J., Karakus, M., Liu, L., Zhou, H., & Yu, M. (2021). A New Theoretical Method to Predict Strata Movement and Surface Subsidence due to Inclined Coal Seam Mining. *Rock Mechanics and Rock Engineering*, *54*(6), 2723–2740. https://doi.org/10.1007/s00603-021-02424-z

Tang, B., & Mitri, H. (2001). Numerical Modelling of Rock Preconditioning by Destress Blasting. *Ground Improvement*, *5*(2), 57–67.

Tavakkoli, M., Mohammadsadeghi, M., Shahrabadi, A., Khajoee, S., Malakooti, R., & Beidokhti, M. S. (2009). Deterministic versus Stochastic Discrete Fracture Network (DFN) Modeling, Application in a Heterogeneous Naturally Fractured Reservoir. *All Days*, 14–16. https://doi.org/10.2118/127086-MS

Terzaghi, K. (1936). Relation Between Soil Mechanics and Foundation Engineering - Presidential Adress. *INTERNATIONAL SOCIETY FOR SOIL MECHANICS AND GEOTECHNICAL ENGINEERING*, 13–18. https://www.issmge.org/publications/online-library

Tien, J. C. (2011). Room-and-Pillar Mining in Coal. In P. Darling (Ed.), *Mining Engineering Handbook* (3rd ed., pp. 1339–1346). Society for Mining, Metallurgy, and Exploration.

Timur, U. P., Orhan, M., & Aksüt, A. (2014). Çankırı Kaya Tuzu Mağarasının ve Yakın Çevresinin Turizm ve Rekreasyonel Amaçlı Kullanımının İrdelenmesi. *Ormancılık Dergisi*, *10*, 97–113.

Toper, A. Z., Grodner, M., Stewart, R. D., & Lightfoot, N. (1997). Preconditioning: A Rockburst Control Technique. In S. J. Gibowicz & S. Lasocki (Eds.), *Rockbursts and Sesmicity in Mines* (pp. 267–272). Balkema.

Turkmen, M. O., & Gozel, M. E. (2014). Fracture Characterization of a Carbonate Reservoir by DFN Modeling: A Case Study. *Proceedings - SPE Annual Technical Conference and Exhibition*, *3*, 1648–1669. https://doi.org/10.2118/170699-MS

Ünal, E. (1983). *Design Guidelines and Roof Control Standards for Coal Mine Roofs* [PhD]. Pennsylvania State University.

Ünal, E., & Özkan, İ. (1996). A Critical Review on Rock Mass Classification Systems. *Turkish National Rock Mechanics Symposium*, *3*, 181–193.

USGS. (2022). *Soda Ash*.

Van Besien, A. C. (1973). Analysis of Roof Fall Accident Statistics and their Application to Roof Control Research. *AIME Annual Meeting*, 71–73.

Vennes, I., Mitri, H., Chinnasane, D. R., & Yao, M. (2020). Large-scale destress blasting for seismicity control in hard rock mines: A case study. *International*

Journal of Mining Science and Technology, *30*(2), 141–149. https://doi.org/10.1016/j.ijmst.2020.01.005

Wang, G., & Yuan, J. (1997). A New Method for Solving the Contact-Friction problem. *Computer Methods and Advances in Geomechanics*, *2*, 1965–1967.

Wang, X., & Cai, M. (2020). A DFN–DEM Multi-scale Modeling Approach for Simulating Tunnel Excavation Response in Jointed Rock Masses. *Rock Mechanics and Rock Engineering*, *53*(3), 1053–1077. https://doi.org/10.1007/s00603-019-01957-8

Wei, L., Yinping, L., Chunhe, Y., Deyi, J., Daemen, J. J. K., Jie, C., & Junfeng, K. (2016). A new method of surface subsidence prediction for natural gas storage cavern in bedded rock salts. *Environmental Earth Sciences*, *75*(9), 1–17. https://doi.org/10.1007/S12665-016-5611-8/FIGURES/17

Weishen, Z., Yong, L., Shucai, L., Shugang, W., & Qianbing, Z. (2011). Quasi-three-dimensional physical model tests on a cavern complex under high in-situ stresses. *International Journal of Rock Mechanics and Mining Sciences*, *48*(2), 199–209. https://doi.org/10.1016/j.ijrmms.2010.11.008

Whittaker, B. N., & Reddish, D. J. (1989). Subsidence Occurrence, Prediction and Control. *Developments in Geotechnical Engineering*, *56*, 359–376. http://www.saveballona.org

Whyatt, J., & Varley, F. (2008). Catastrophic Failures of Underground Evaporite Mines. In S. S. Peng, C. Mark, G. L. Finfinger, S. C. Tadolini, A. W. Khair, K. A. Heasley, & Luo-Y (Eds.), *27th International Conference on Ground Control in Mining* (pp. 113–122). West Virginia University.

Wojtecki, Ł., Konicek, P., Mendecki, M. J., Gołda, I., & Zuberek, W. M. (2020). Geophysical Evaluation of Effectiveness of Blasting for Roof Caving During Longwall Mining of Coal Seam. *Pure and Applied Geophysics*, *177*(2), 905–917. https://doi.org/10.1007/s00024-019-02321-1

Xiao, Y. X., Feng, X. T., Feng, G. L., Liu, H. J., Jiang, Q., & Qiu, S. L. (2016). Mechanism of evolution of stress-structure controlled collapse of surrounding rock in caverns: A case study from the Baihetan hydropower station in China. *Tunnelling and Underground Space Technology*, *51*, 56–67. https://doi.org/10.1016/j.tust.2015.10.020

Yardimci, A. G. (2013). *Fuzzy Approach in Preliminary Design Of Weak Rock Slopes For Lignite Mines*.

Zangerl, C., Eberhardt, E., Evans, K. F., & Loew, S. (2008). Consolidation settlements above deep tunnels in fractured crystalline rock: Part 2-Numerical analysis of the Gotthard highway tunnel case study. *International Journal of Rock Mechanics and Mining Sciences*, *45*(8), 1211–1225. https://doi.org/10.1016/j.ijrmms.2008.02.005

Zhang, G., Wang, Z., Zhang, K., Li, Y., Wu, Y., Chen, Y., & Zhang, H. (2018). Collapse mechanism of the overlying strata above a salt cavern by solution mining with double-well convection. *Environmental Earth Sciences*, *77*(16). https://doi.org/10.1007/s12665-018-7739-1

Zhang, G., Zhang, H., Liu, Y., Wang, T., & Wang, Z. (2023). Surrounding rock stability of horizontal cavern reconstructed for gas storage. *Journal of Energy Storage*, *59*. https://doi.org/10.1016/j.est.2022.106534

Zhang, X., Yu, H., Dong, J., Liu, S., Huang, Z., Wang, J., & Wong, H. (2017). A physical and numerical model-based research on the subsidence features of overlying strata caused by coal mining in Henan, China. *Environmental Earth Sciences*, *76*(20). https://doi.org/10.1007/s12665-017-6979-9

Zhou, J., Huang, H., & Deo, M. (2016). *Simulation of Hydraulic and Natural Fracture Interaction Using a Coupled DFN-DEM Model*. OnePetro. http://onepetro.org/ARMAUSRMS/proceedings-pdf/ARMA16/All-ARMA16/ARMA-2016-739/1329110/arma-2016-739.pdf

Zienkiewicz, C., & Kelly, D. W. (1977). The Coupling of the Finite Element Method and Boundary Solution Procedures. *INTERNATIONAL JOURNAL FOR NUMERICAL METHODS IN ENGINEERING*, *11*, 355–375.

Zienkiewicz, O. C., Best, B., Dullage, C., & Stagg, K. (1970). Analysis of non-linear problems in rock mechanics with particular reference to jointed rock systems. *2nd International Congress on Rock Mechanics*, 501–509.

Zipf, K. R. Jr. (2001, June). Toward Pillar Design to Prevent Collapse of Room-and-Pillar Mines. *108th Annual Exhibit and Meeting*.

Zipf, K. R., & Swanson, P. (1999, June). Description of a large catastrophic failure in a southwestern Wyoming Trona Mine. *The 37th U.S. Symposium on Rock Mechanics*.

Zipf, R. K. Jr. (2001). Pillar Design to Prevent Collapse of Room-and-Pillar Mines. In W. A. Hustrulid & R. L. Bullock (Eds.), *Underground Mining Methods: Engineering Fundamentals and International Case Studies* (pp. 493–511). Society for Mining, Metallurgy, and Exploration, Inc

APPENDICES

A. Appendix 1

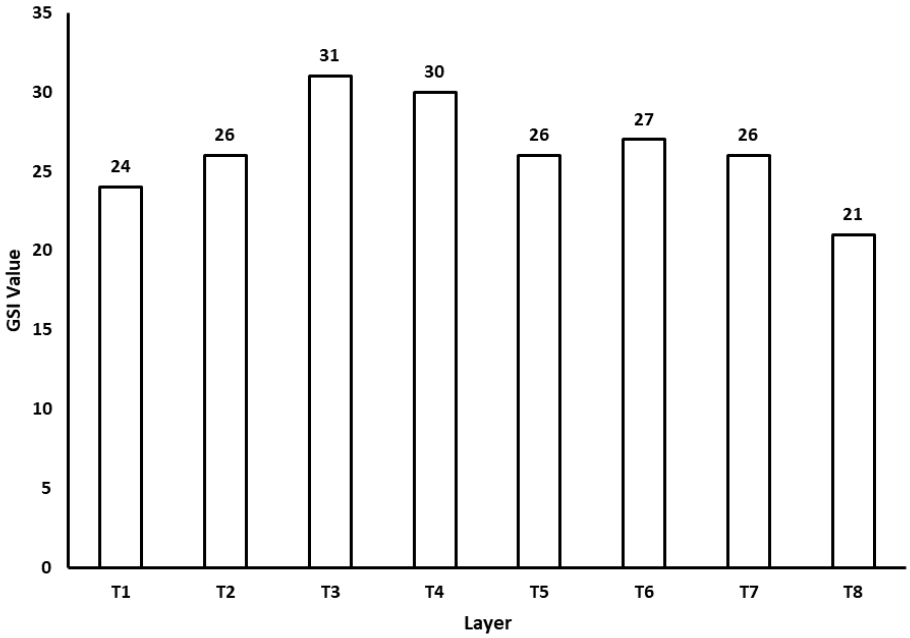

Figure A.1 GSI distribution of the strata

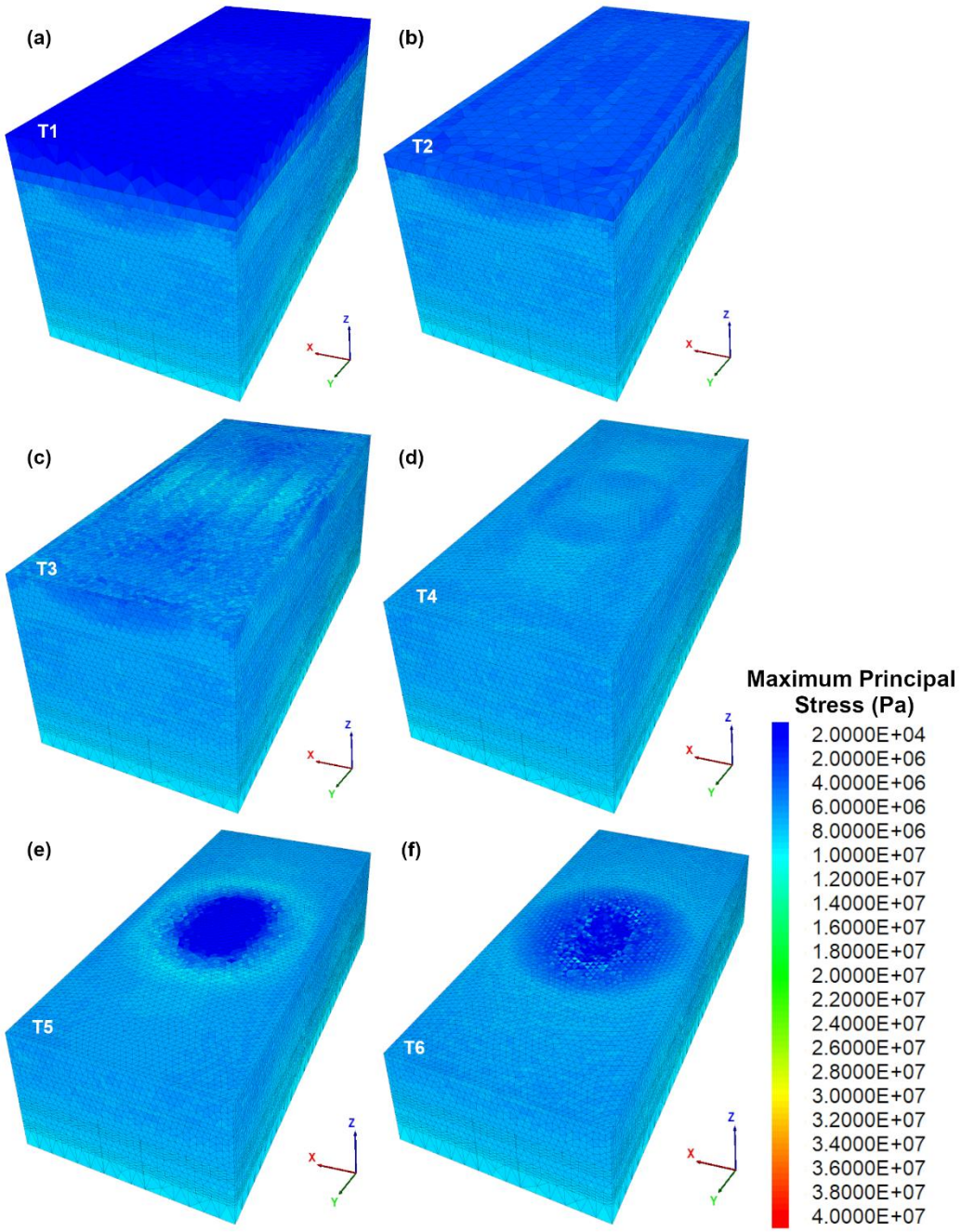

Figure A.2 After completing the trona removal the maximum principal stresses in (a) T1 layer (b) T2 layer (c) T3 layer (d) T4 layer (e)T5 layer (f) T6 layer

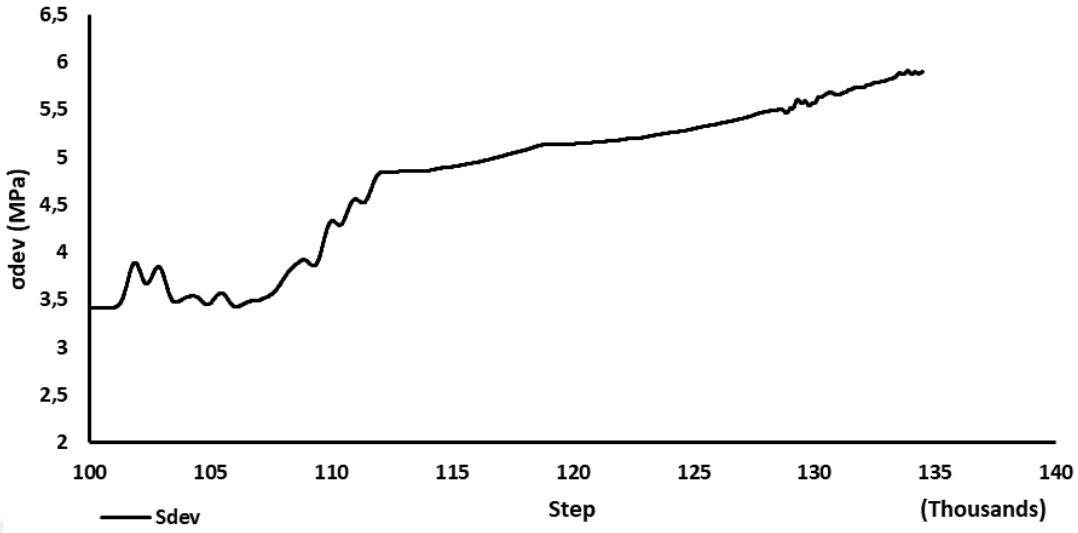

Figure A.3 σ_{dev} (in T3 layer) graph of woDESS model

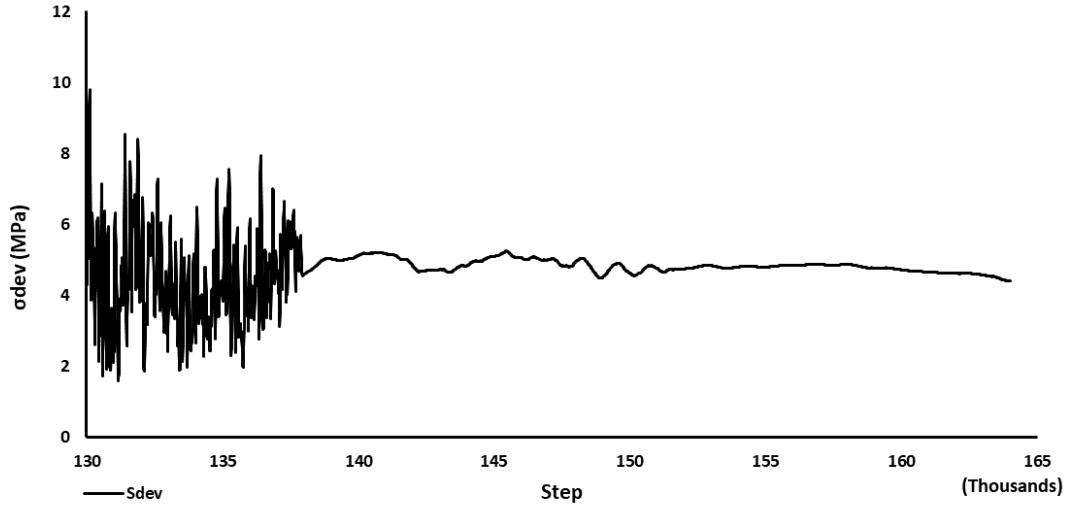

Figure A.4 σ_{dev} (in T3 layer) graph of DESS model

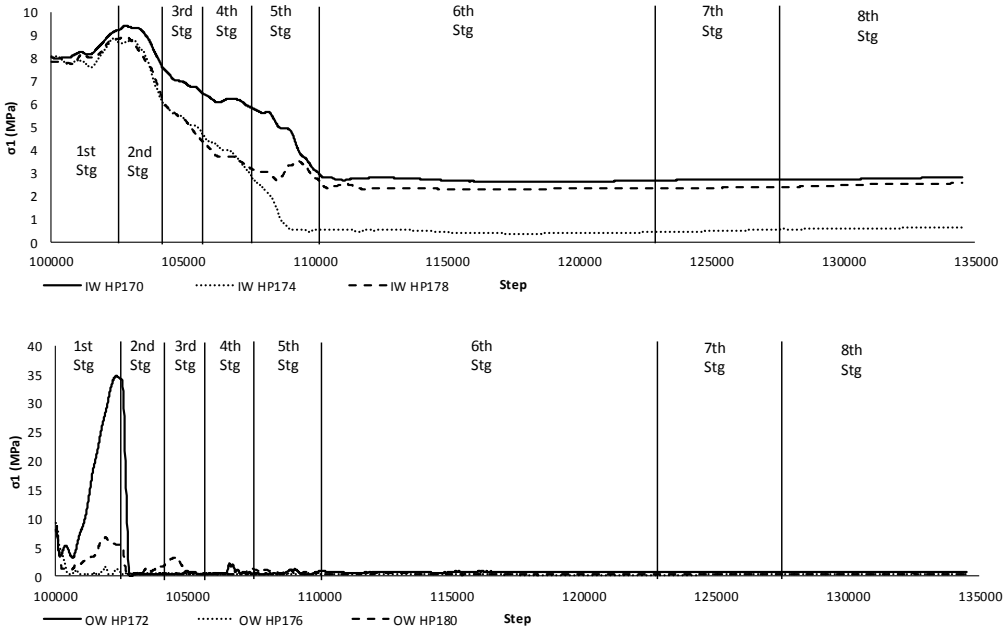

Figure A.5 σ_1 history of the 1st stage level history points on the cavern wall (upper) and 20 m inside the cavern wall (lower)

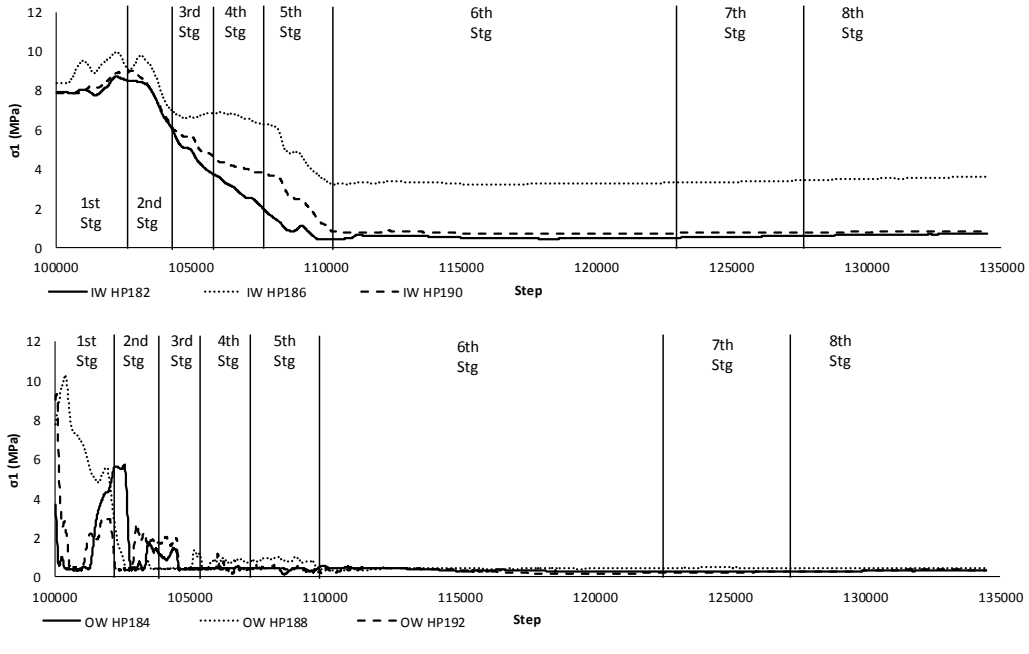

Figure A.6 σ_1 history of the 2nd stage level history points on the cavern wall (upper) and 20 m inside the cavern wall (lower)

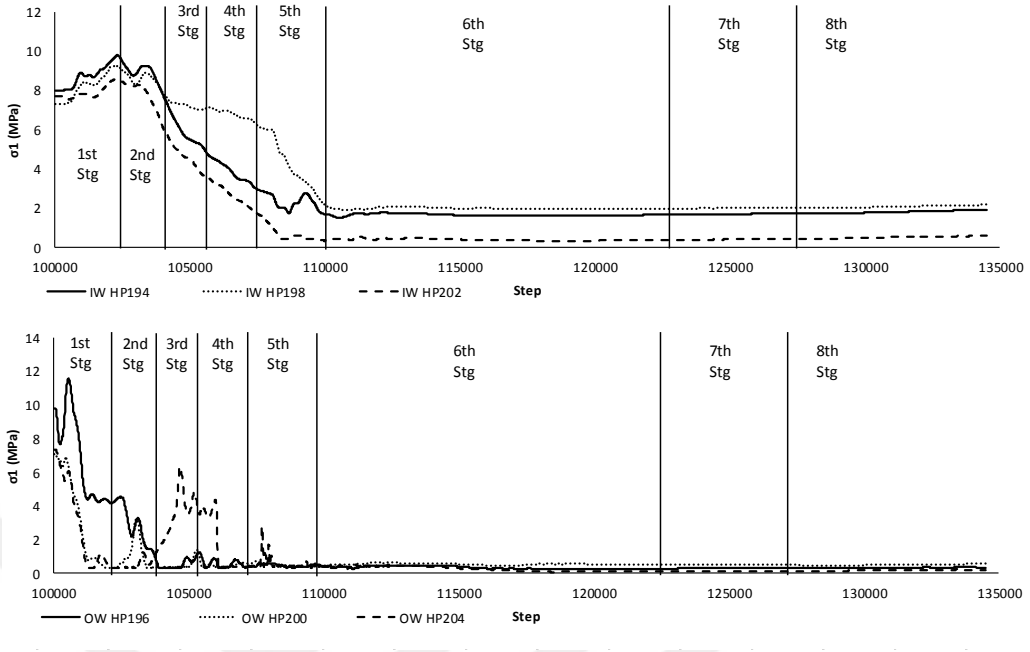

Figure A.7 σ_1 history of the 3rd stage level history points on the cavern wall (upper) and 20 m inside the cavern wall (lower)

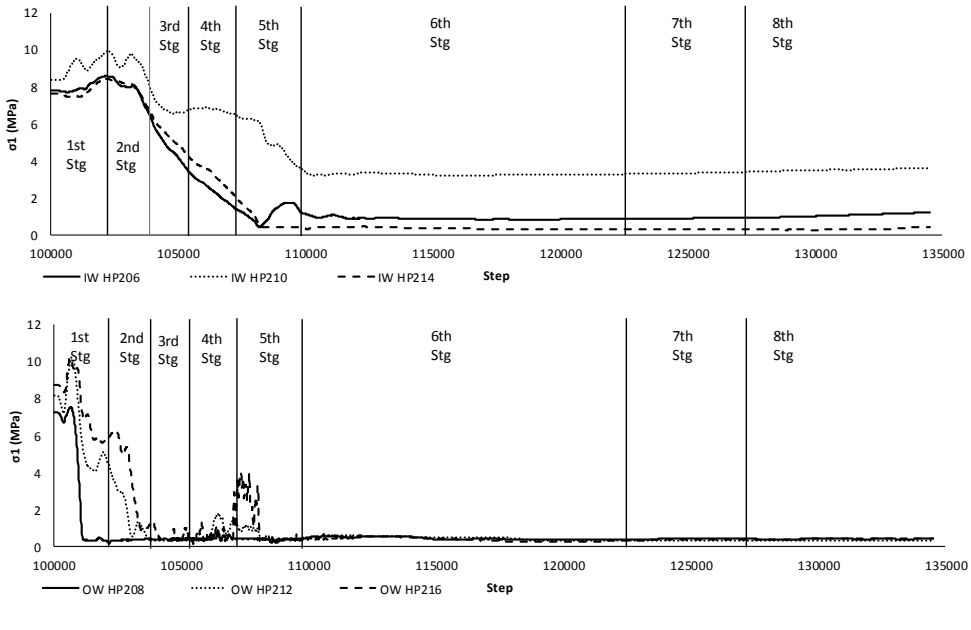

Figure A.8 σ_1 history of the 4th stage level history points on the cavern wall (upper) and 20 m inside the cavern wall (lower)

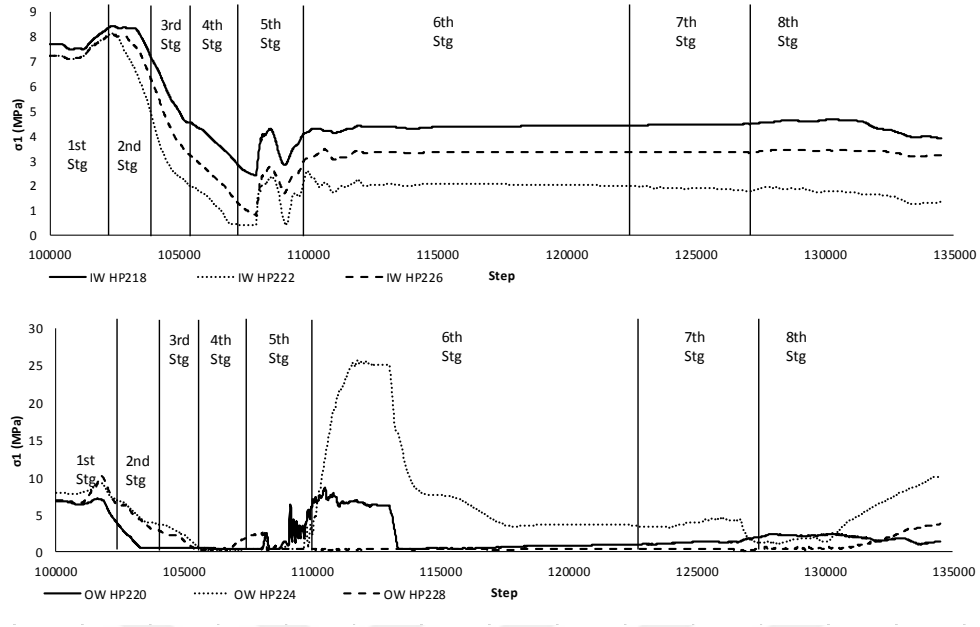

Figure A.9 σ_1 history of the 5th stage level history points on the cavern wall (upper) and 20 m inside the cavern wall (lower)

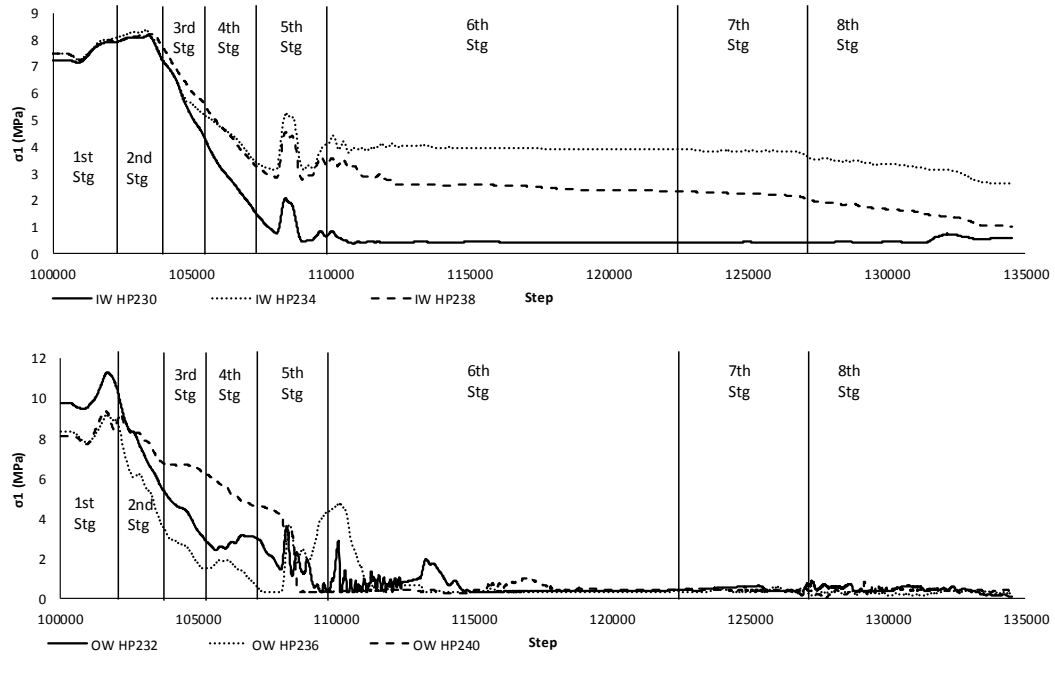

Figure A.10 σ_1 history of the 6th stage level history points on the cavern wall (upper) and 20 m inside the cavern wall (lower)

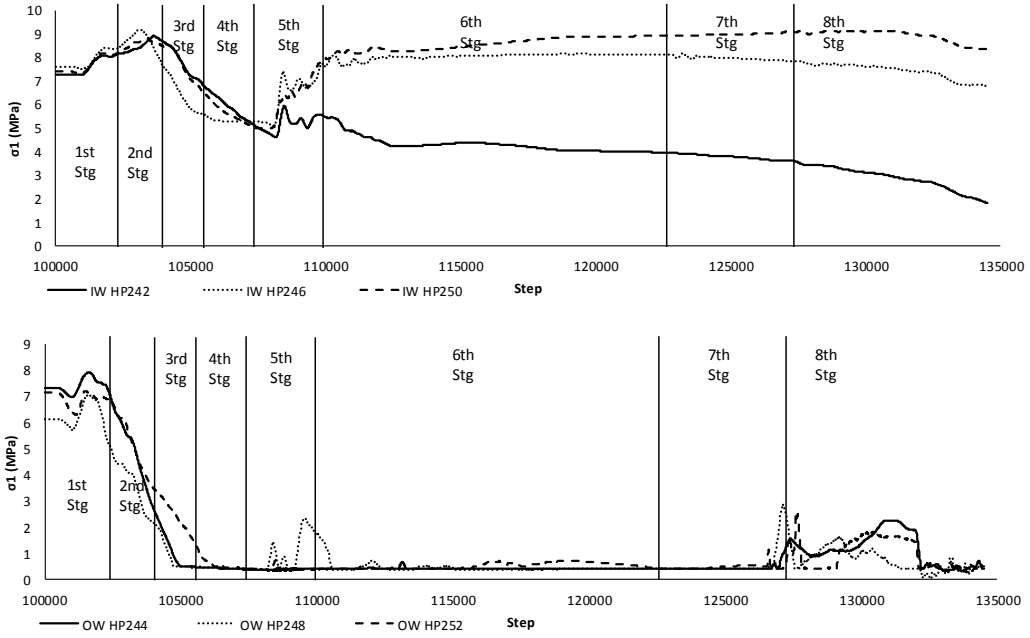

Figure A.11 σ_1 history of the 7th stage level history points on the cavern wall (upper) and 20 m inside the cavern wall (lower)

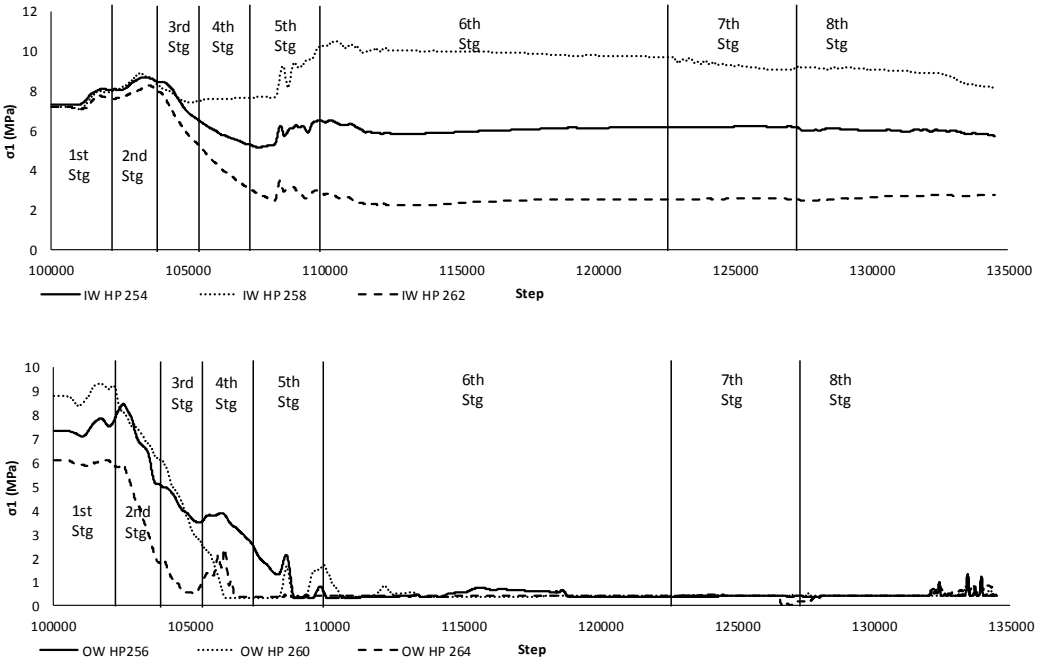

Figure A.12 σ_1 history of the 8th stage level history points on the cavern wall (upper) and 20 m inside the cavern wall (lower)